Positron accumulation and laser excitation of the positronium atom.

Deller, Adam

Positron Accumulation and Laser Excitation of the Positronium Atom

College of Science
Coleg Gwyddoniaeth

Swansea University
Prifysgol Abertawe

Adam Deller - October 2013

A thesis submitted to the Department of Physics, Swansea University for the degree of Doctor of Philosophy.

Abstract

We present techniques used in the accumulation and manipulation of positrons in an electrostatic trap, optimised with a view to producing the positronium atom (Ps) through positron bombardment of a porous silica film. Furthermore, a broadband UV laser has been developed for exciting the interval of the Lyman-α transition of Ps. Excitation of those atoms emitted to vacuum has been inferred from an observed reduction in their lifetime in coincidence with the laser pulse, as evidenced through measurement of the annihilation signal with a fast $PbWO_4$ gamma-ray detector. The excitation signal was recorded as the laser was tuned through the resonant wavelength of the transition (measured to be 243.020 ± 0.007 nm in vacuum) to determine the Doppler broadened linewidth, and thus make an estimate of the kinetic energy distribution associated with motion of the Ps atoms in the direction of the laser. The width of the distribution has been observed to negatively correlate with the positron implantation energy (i.e., implantation depth), indicating cooling of the Ps atoms as they diffuse through the pores to the surface. The lowest mean energy recorded in this way is estimated at 27 ± 2 meV for Ps formed by positrons embedded into the target at 2.9 keV.

Declaration

This work has not previously been accepted in substance for any degree and is not being concurrently submitted in candidature for any degree.

Signed ... (candidate)

Date .....21/10/2013.....

Statement 1

This thesis is the result of my own investigations, except where otherwise stated. Where correction services have been used, the extent and nature of the correction is clearly marked in a footnote(s).

Other sources are acknowledged by footnotes giving explicit references. A bibliography is appended.

Signed .. (candidate)

Date .....21/10/2013.....

Statement 2

I hereby give consent for my thesis, if accepted, to be available for photocopying and for inter-library loan, and for the title and summary to be made available to outside organisations.

Signed ... (candidate)

Date .....21/10/2013.....

Contents

Appendices

Acknowledgements

I am exceptionally lucky to have spent my time as a postgraduate student working alongside such brilliant and interesting people. I wish to thank my supervisor, Dr Dirk van der Werf, for much valued advice and many stimulating arguments, but in particular for affording me the freedom I've enjoyed throughout my studies. I must also thank my second supervisor, Prof. Michael Charlton - a verifiable authority on positrons and positronium (and Rory Gallagher) - these works have immeasurably benefited from Mike's insightful comments and considered suggestions. I am further grateful to Dr Aled Isaac and Dr Timothy Mortensen, who so expertly introduced me to the positron lab and made my experience working in it so enjoyable.

The UV laser described in chapter 3 of this thesis owes its - long awaited - existence to the advice and support that was kindly given by Prof. Helmut Telle, and I earnestly thank Helmut for the time he has devoted to this project. I further thank Dr Richard Lewis and Dr Serena Kerrigan, for much help in the early stages of the laser's development.

It would be impossible to have made any progress with this experiment without the assistance of our technical and administrative staff. I duly acknowledge my appreciation to these most excellent people - in particular: David Payne, Hugh Thomas, Jonathan Woodman-Ralph, Philip Hopkins, Ray Squire, Linda Andrews, Liz Davies and Gill Oliver. I would like especially to thank Julian Kivell, for the superb technical advice and support he's so consistently provided.

I am also fortunate to have met so many fascinating people during my degree - through collaboration, at conferences and in liaising with industry. I am grateful to those I've encountered for their encouraging enthusiasm, friendly critique and refreshing perspective, and am obliged to highlight the special contributions to the furthering of this work of Dr David Cassidy, Dr Rainer Novotny, Dr Joshua Machacek and Vitaly Matsiuk.

I am very glad to have been given the opportunity to contribute time from this study to the ALPHA antihydrogen experiment. The extraordinary achievements of the ALPHA collaboration are testament to the myriad of exceptional and genuinely inspirational scientists who make it. I am truly privileged to have worked with such people and wish them every success for the future. I need especially to thank Prof. Niels Madsen, Dr William Bertsche and Dr Paul Bowe, for each making a particular effort to help me through the steepest of learning curves. I am also grateful to Prof. Francis Robicheaux for providing the Poisson solver code used in chapter 4 of these works.

The completion of this thesis was made possible by the love, support and treasured distractions of my family and friends. I am eternally grateful and proffer my thanks to these awesome people. I am especially indebted to my parents, Jacqui and Neal Deller, who have ever supported my every pursuit; and to Rachel Sirrell, who has inexplicably stuck by me for the best part of a decade.

List of Tables

List of Figures

Nomenclature

Acronyms

AI/O	Analogue Input/Output
CERN	European Organization for Nuclear Research
CPT	Charge conjugation, Parity & Time reversal
DI/O	Digital Input/Output
FPGA	Field Programmable Gate Array
MCP	MicroChannel Plate
NI	National Instruments corporation
PID	Proportional, Integral & Derivative (feedback)
PMT	PhotoMultiplier Tube
QED	Quantum ElectroDynamics
RW	Rotating Wall
(SS)PALS	(Singe-Shot) Positron Annihilation Lifetime Spectroscopy

Physical Constants

c	speed of light in vacuum	$2.997\,924\,58 \times 10^{8}\ \mathrm{m\,s^{-1}}$
ϵ_0	permittivity of free space	$8.8542 \times 10^{-12}\ \mathrm{F\,m^{-1}}$
e	elementary charge	$1.602\,176\,565 \times 10^{-19}\ \mathrm{C}$
h	Planck constant	$6.626\,069\,57 \times 10^{-34}\ \mathrm{J\,s}$
$\hbar$	reduced Planck constant	$1.054\,571\,72 \times 10^{-34}\ \mathrm{J\,s}$
k_B	Boltzmann constant	$1.380\,648\,8 \times 10^{-23}\ \mathrm{J\,K^{-1}}$
m_e	electron mass	$9.109\,382\,15 \times 10^{-31}\ \mathrm{kg}$

Particles

e^-	electron
e^+	positron
ν_e	electron neutrino
n	neutron
γ	photon
p	proton
Ps	positronium atom
$W^\pm$	W ($\pm$) boson

Quantum Numbers

l	orbital angular momentum
m_l	magnetic
m_s	spin projection
n	principal
s	spin

Symbols

a	lattice spacing
$\vec{B}$	magnetic field
$\vec{E}$	electric field
E	energy
Γ	rate
I	electrical current
λ_D	Debye length
ϕ	electric potential
φ	work-function **or** phase
L	length
m	mass
ν	frequency

n	density **or** integer
$\varnothing$	diameter
ω	angular frequency
q	electric charge
ρ	radius
τ	lifetime
T	temperature
t	time
U	potential energy
$\vec{v}$	velocity
(x,y,z)	Cartesian coordinates
(r,θ,z)	cylindrical coordinates

Unless stated otherwise, all equations pertaining to measurable quantities are expressed in units of the Systém International (SI) standard.

Elements may be refereed to using the appropriate shorthand chemical symbol. Antiparticles are differentiated from particles by use of an overbar (e.g. $\overline{\nu_e}$), with the exception of the positron which is given as e^+. For clarity, symbols specific to positrons (electrons) are indicated by subscript +(-).

I think that the discovery of antimatter was perhaps the biggest jump of all the big jumps in physics in our century.

Werner Heisenberg, 1973

Chapter 1

Introduction

In the early twentieth century an extraordinary development in theoretical physics - Quantum Mechanics - revolutionised our view of the Universe and provided a foundation from which eventually developed the *Standard Model of Particle Physics* - a theory of twelve elementary particles and their interactions, as mediated by the electromagnetic, weak and strong forces.

The Standard Model has successfully met rigorous experimental tests, yet is nonetheless incomplete in ignorance of the most tangible force, gravity. Furthermore, the theory fails to explain certain cosmological phenomena, such as dark matter, dark energy, and the apparent imbalance between matter and antimatter in the Universe (baryon asymmetry).

In view of the known limitations of the Standard Model, it falls to the experimentalist to guide the vast spectrum of theories which vie to surpass it. A potential route identified for such is in stringent study of antimatter - the goal: to seek out any properties of this enigmatic substance which deviate from the Standard Model description and to explain its conspicuous scarcity in the Universe.

1.1 Antimatter

In the late 1920s, following the earliest developments in Quantum Mechanics, the British physicist Paul Dirac published his formulation of a relativistic wave equation for the electron [Dirac, 1928a,b]. Despite accurately predicting the electron spin and magnetic moment, and also the Sommerfeld fine structure of hydrogen, the Dirac equation allowed paradoxical negative kinetic energy states of the electron. In answer as to why electrons do not cascade down into the negative states, Dirac postulated that they are filled with an infinite sea of electrons and that the Pauli exclusion principle thus prevents transitions into them.

Dirac [1930] extended his reasoning to consider the transition of an electron from the sea into a positive energy state, thereby leaving behind a *hole*: an unoccupied negative state. He noted that such a hole would be observable as a real particle with equal but opposite spin and electric charge to the electron. At that time the only known sub-atomic particles were the electron and proton, it is perhaps logical then that Dirac initially identified the hole with the latter. However, closer inspection of the theory revealed that the electron and hole must have equal mass, invalidating such a hypothesis. Rather than dismissing the hole as a by-product of elegant mathematics ungrounded in reality, Dirac [1931] instead proposed that it could exist as an as-yet undiscovered particle, the anti-electron, and remarkably that the antiparticle equivalent for the proton might also exist. In the same article, Dirac was prudent to state,

> *We should not expect to find any [anti-electrons] in nature, on account of their rapid rate of recombination with electrons, but if they could be produced experimentally in high-vacuum they would be quite stable and amenable to observation.*

Despite such striking perspicacity, Dirac's conservative testimony that in nature anti-electrons would be so exceptionally impermanent as to be beyond observing, was swiftly proved inaccurate.

Two years after the publication of Dirac's antiparticle hypothesis, Carl Anderson [1933] made the momentous claim of having photographed ionisation tracks of positive electrons (figure 1.1); also termed *positrons* and expeditiously identified as Dirac's theorised anti-electron. It seems likely that positrons had been observed in similar cosmic-ray studies before [see Hanson, 1961], however Anderson was the first to unambiguously negate the possibility of such particles being protons or 'backwards' electrons. For his discovery of the positron, Anderson was awarded a share of the 1936 Nobel prize.

It is now generally accepted that Dirac's intuition was correct, in that all types of matter particle have an antiparticle analogue, identical in mass and lifetime (in vacuum) and with equal but opposite electric charge and spin; in some special cases, such as the photon, a particle is its own antiparticle. With sufficient energy, particles and antiparticles can be created (pair production); equivalently, particles and their antiparticle counterparts can annihilate, the mass of each being converted into energy in accordance with Einstein's famous equation,

$$E = mc^2 \,. \tag{1.1}$$

In the case of electron-positron annihilation, the energy will most often take the form of a pair of 511 keV gamma-rays.

Due to the relatively large rest-mass of baryons, the development of particle accelerators with collision energies greater than 2 GeV was necessary before pair-production of protons could be realised. Consequently, it wasn't until 1955 that the antiproton ($\bar{\mathrm{p}}$) was observed, by Chamberlain *et al.* at the newly commissioned Bevatron proton accelerator located at Lawrence Berkeley National Laboratory in California. A year later the same machine also facilitated the discovery of the antineutron ($\bar{\mathrm{n}}$) [Cork *et al.*, 1956].

Composite antimatter structures were later realised with the discovery of the antideuteron ($\bar{\mathrm{p}}\bar{\mathrm{n}}$), both at Brookhaven National Laboratory in New York [Dorfan *et al.*, 1965], and independently at the Proton Synchrotron (PS) based at CERN in Geneva [Massam *et al.*, 1965].

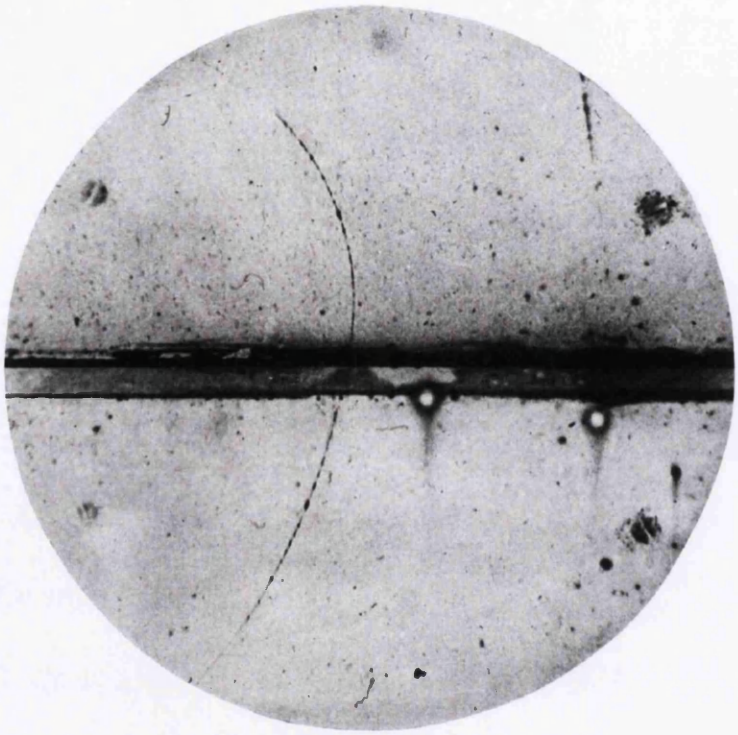

Figure 1.1: A 63 million volt positron ($H\rho = 2 \times 10^5$ gauss-cm) passing through a 6 mm lead plate and emerging as a 23 million volt positron ($H\rho = 7.5 \times 10^4$ gauss-cm). The length of the latter path is at least 10 times greater than the possible length of a proton path of this curvature. *N.B.* the magnetic field amplitude, H, is 15 000 gauss and ρ denotes the radius of curvature. [Anderson, 1933, Fig. 1, p. 495]

Anti-atoms are of especial interest, in particular antihydrogen ($\overline{\mathrm{H}}$) - the antimatter equivalent of the simplest and the most abundant element in the Universe. Spectroscopic studies of $\overline{\mathrm{H}}$ have the potential to exquisitely test the combined symmetry of Charge conjugation, Parity and Time reversal (CPT) that underpins the Standard Model, and restricts the quantum states of hydrogen and antihydrogen into exact accord.

The first observation of antihydrogen was made by the PS210 experiment [Baur *et al.*, 1996] at the Low Energy Antiproton Ring (LEAR) in CERN, where 11 ± 2 antihydrogen events were identified; a similar result was later reproduced by the E862 experiment based at Fermilab [Blanford *et al.*, 1998]. In 2000 the Antiproton Decelerator (AD) began operations at CERN, and within two years both the ATHENA [Amoretti *et al.*, 2002] and ATRAP [Gabrielse *et al.*, 2002] collaborations had reported manufacturing $\sim 10^4$ antihydrogen atoms at the facility. Both experiments utilised similar techniques for cooling and mixing nonneutral plasmas of positrons and antiprotons using specialised Penning-Malmberg traps (see section 2.3.1). This process was further refined by the ALPHA collaboration (AD, CERN) to form $\overline{\mathrm{H}}$ atoms sufficiently cool ($\leqslant 0.5$ K) to be trapped within a co-located magnetic bottle [Andresen *et al.*, 2010]; the same collaboration later reported confinement times of up to 1,000 s [Andresen *et al.*, 2011]. These developments were motivated by the goal of precision spectroscopic measurements of $\overline{\mathrm{H}}$ as a test of CPT symmetry, and although such is yet to be achieved, a proof-of-principle microwave measurement of the ground state hyperfine splitting of $\overline{\mathrm{H}}$ has recently been reported by ALPHA [Amole *et al.*, 2012].

Hybrid matter-antimatter atomic elements have also been artificially created, such as positronium [Deutsch, 1951] (see section 1.3), muonium [Hughes *et al.*, 1960] and antiprotonic helium [see e.g., Yamazaki *et al.*, 2002].

1.2 Positrons

1.2.1 Positron Sources

Anderson's discovery of the positron was contingent upon chance coincidence of infrequent, sufficiently energetic cosmic-rays impinging on a Wilson chamber, and photographic capture of the rare events that resulted in a positron track. For antimatter research to significantly progress, a more abundant source than the skies was required. Fortunately, pair production can be instigated by a variety of adequate energy sources, e.g. particle accelerators and nuclear reactors - two technologies that have undergone aggressive advancement since the 1940s. The mechanism is conventionally achieved by implanting fast electrons from an accelerator into a target with a high atomic number (e.g W, Ta, Pt). The retardation of electrons within the material generates bremsstrahlung radiation, that in turn instigates pair production of positrons and electrons [Howell *et al.*, 1987].

An alternative source of positrons is found in the weak nuclear decay of β^+ emitting radioisotopes, such as ^{64}Cu, ^{22}Na, ^{58}Co and ^{18}F - see figure 1.2.

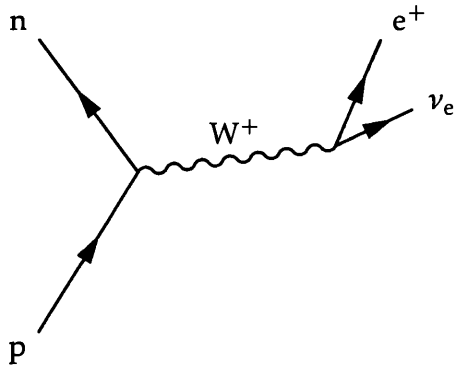

Figure 1.2: Feynman diagram depicting the β^+ decay of a proton (p) into a neutron (n), a positron (e^+) and an electron neutrino (ν_e).

The sodium radioisotope ^{22}Na is particularly well suited for lab-based research, with a large β^+ branching ratio ($\sim$ 90 %), a reasonably long half-life (2.6 years) and source activities as high as 2 GBq commercially available. Furthermore, β^+

decay of ^{22}Na yields an excited state of neon that decays rapidly with emission of a 1.274 MeV photon (see equation 1.2), providing a convenient *start* signal for positron annihilation lifetime measurements [see Knoll, 2000, for further details].

$$\begin{array}{rcccccl} {}^{22}_{11}\mathrm{Na} \rightarrow & {}^{22}_{10}\mathrm{Ne}^{*} & + & \mathrm{e}^{+} & + & \nu_{\mathrm{e}} & (2.6\ \mathrm{yr}) \\ & \hookrightarrow & & {}^{22}_{10}\mathrm{Ne} & + & \gamma & (3.7\ \mathrm{ps}) \end{array} \tag{1.2}$$

A disadvantage of source based beams is the broad energy spread of the emitted positrons; those emitted from ^{22}Na range in energies up to 545 keV, with an expectation value of 120 keV [Hugenschmidt, 2009].

1.2.2 Positron Moderation

One of the most significant developments in positron beam technologies originates in the serendipitous discovery of positron moderation [Cherry, 1958]. During his postgraduate research, Cherry noted that the energy distribution of positrons impinging on a sample of chromium-on-mica was partially reduced upon re-emission from the sample surface. Although Cherry's discovery took some time to catch the attention of the antimatter community at large, positron moderation later became one of the most hotly pursued interests in the field.

Emission into vacuum of positrons implanted into solid sample surfaces is possible when the average diffusion length before annihilation (L_+), is comparable to the depth at which the positrons thermalise in the bulk, through e.g. inelastic collisions with core and conduction electrons, plasmon excitation and phonon scattering. For samples with a negative positron work-function (φ_+), positrons arriving back at the surface may be emitted as free positrons into vacuum at greatly reduced energies (see figure 1.3). Presently, the most widely used metallic moderator is tungsten, with a large positron work-function ($\sim$ 3 eV) and fast-slow positron conversion efficiencies as high as $\epsilon \sim 2 \times 10^{-3}$ [Dale *et al.*, 1980]; such efficiencies require annealing of the material, to minimise defects that might otherwise capture diffusing positrons.

Other moderating materials of interest include the solid rare-gases (e.g. Ne, Ar, Kr, Xe), despite the fact that such substances posses positive positron work-functions. Positrons implanted into such materials may only overcome φ_+ at the surface, if upon arrival they are yet to be completely thermalised, and have thereby retained sufficient energy to do so - such is termed epithermal (hot) emission [Gullikson and Mills, 1986]. This processes is only possible when L_+ within the bulk is very long - as is typical of rare-gas solids. In general, both the angular and energy distribution of positrons emitted epithermally is somewhat broader than is the case with the best metallic moderators [Coleman, 2000], however significantly higher efficiencies are attainable - e.g. up to 1 % with solid neon. As with tungsten, the most efficient rare-gas moderators are obtained with annealing [Özen *et al.*, 2000]; yet further yield improvements are reported with the addition of surface containments, such as water [Petkov *et al.*, 1996], surface charging [Merrison *et al.*, 1992], and refinement of the moderator substrate geometry [Khatri *et al.*, 1990].

Solid rare-gas moderators have a number of practical disadvantages, principal among which is that they require cryogenic apparatus for condensing the gases directly onto the positron source mount. Furthermore, the growth of such moderators is difficult to consistently reproduce, as the efficiency is highly sensitive to temperature, vacuum conditions and contaminants, and also exhibits degradation - necessitating frequent re-growth procedures and curtailing the equability of long experimental runs.

1.2.3 Positron Accumulation

The significant advancements in positron moderation (see section 1.2.2) later facilitated invention of a device to accumulate positrons from a low energy, continuous source, into a dense non-neutral plasma which could be ejected as an intense pulse. The first such device was designed and built by Surko *et al.* [1988; 1992], and is consequently often refereed to as a *Surko trap*. The design has found applications in the study of positron interactions with atoms, molecules and materials, and has been a key element to many positronium and antihydrogen experiments.

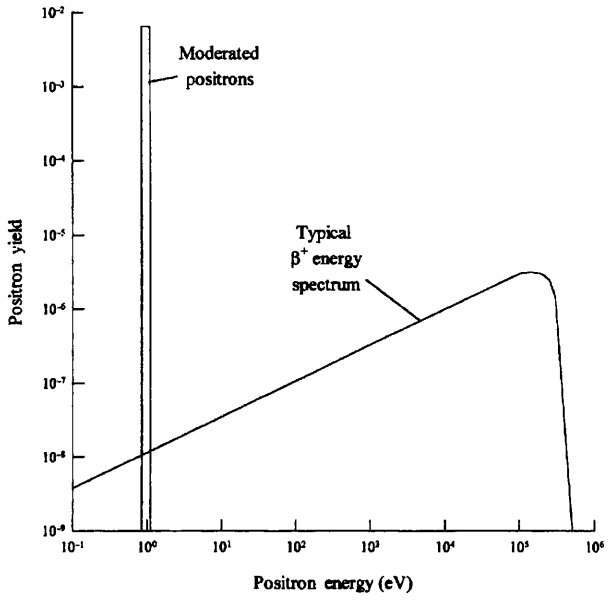

Figure 1.3: Comparison of the energy spectrum of β^+ particles from a radioactive source with that for moderated positrons. [Charlton and Humberston, 2001, Fig. 1.7, p. 17]

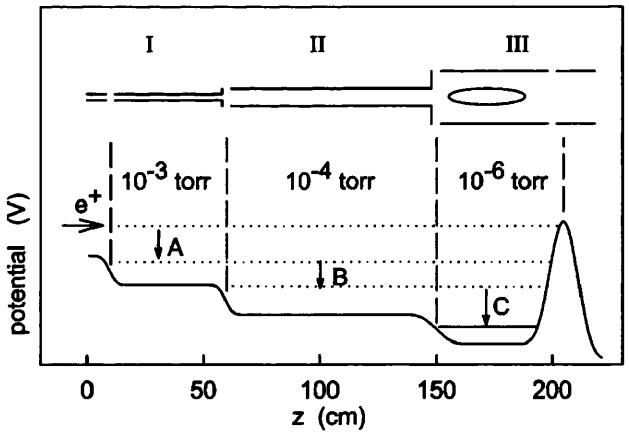

Figure 1.4: Buffer gas trapping scheme, showing the electrode geometry of the modified Penning-Malmberg trap (above), and the axial potential profile (below). There is an applied uniform magnetic field in the z direction. [Surko and Greaves, 2004, Fig. 2, p. 2336]

The Surko trap is based on a cylindrical Penning-Malmberg trap (see section 2.3.1), which confines charged particles radially with a magnetic field and axially with an electrostatic minimum. The Surko trap differs from the Penning trap in that the electric potential is axially asymmetric, in order that incident particles may surmount the entrance potential yet be reflected by that of the far end. Furthermore, the trap contains a low density buffer gas[1] that causes particles traversing the trap to lose energy via inelastic collisions, resulting in confinement. The requisite buffer gas is inevitably detrimental to the lifetime of trapped positrons, therefore the device contains three stages of increasing electrode diameter which - in conjunction to differential pumping - establishes a relatively high buffer gas pressure in the first stage to optimise the trapping rate, withal harbouring significantly lower pressures in the final stage, to where the positrons rapidly cool. Such an instrument is termed a three-stage buffer gas accumulator, and the concept is illustrated as a schematic in figure 1.4.

A subtle variant of the Surko trap is the two-stage buffer gas accumulator (see section 2.3), which in lieu of the third stage sacrifices trapping lifetime, for a simpler and cheaper set-up that is nevertheless well suited for rapid cycle operation - on the order of 0.1 Hz to 100 Hz. A two-stage device may also be coupled to a separate high vacuum third stage, loaded from the former by means of pulsed transfer and dynamic capture [Cassidy *et al.*, 2006a]. Such a hybrid configuration may exceed the long confinement times and high particle numbers offered by even the original three-stage design.

A more radical extension to the Surko trap is the multi-cell trap. This concept is currently under development by a few groups, with designs ranging from several cells [Surko and Greaves, 2003], to several thousand micro-traps [Baker *et al.*, 2012]. There are a number of advantages to the multi-cell design which ultimately increases the total number of positrons that it's practical to accumulate, however there are also many engineering challenges which are yet to be fully addressed.

[1] Typically N_2 is used as a buffer gas. See section 2.3.2.

1.3 Positronium

Positronium (Ps) is a quasi-stable atomic entity comprised of the bound-state of an electron and its antiparticle, the positron. The postulation of such an element was first made by Mohorovičić [1934], who incorrectly attributed *electrum* to the cause of unexplained stellar spectra. The since established term for such an atom, *positronium*, was later coined by Ruark [1945] in a letter of the selfsame title to Physical Review, wherein he describes some of the anticipated spectroscopic properties of the Ps atom.

As elementary in structure as the more familiar hydrogen atom, positronium is well characterised - in terms of the properties and distribution of its quantum energy states - through tried and tested atomic theory. Moreover, as positronium is comprised exclusively of leptons, the fine-structure details are calculable from quantum electrodynamics alone, avoiding the extra complications and uncertainty which encumber the equivalent computations for hadronic structures.

The simplest estimation of the Ps principal quantum energy levels ($n = 1, 2, 3, \ldots\infty$) may be made by trivial adaptation of the Bohr model, yielding a binding energy of 6.8 eV,

$$E_n = \frac{m_e e^4}{16\epsilon_0^2 h^2 n^2} \approx \frac{6.8}{n^2} \text{ [eV]} . \tag{1.3}$$

The positronium ground-state ($n = 1$) is separable into singlet ($s = 0$ para-positronium, p-Ps) and triplet ($s = 1$ ortho-positronium, o-Ps) spin states. The singlet and triplet states are distinctly characterised by their mean lifetimes in vacuum, against the mutual annihilation of their particle-antiparticle components, namely $\tau_{p-Ps} \approx 1.2 \times 10^{-10}$ s and $\tau_{o-Ps} \approx 1.42 \times 10^{-7}$ s. Additionally, conservation of angular momentum ensures that p-Ps self-annihilation in vacuum results in an even number of photons, whereas o-Ps must produce an odd number $\geqslant 3$ [Charlton and Humberston, 2001].

Denoting the four individual sub-states of the ground-state in accord with the

Dirac notation of the form $|s, m_s\rangle$, the spin of the individual constituent particles may be explicated, as in equation 1.4.

$$\begin{aligned} |0,0\rangle &= \tfrac{1}{\sqrt{2}}(|\uparrow,\downarrow\rangle - |\downarrow,\uparrow\rangle)\,, \\ |1,0\rangle &= \tfrac{1}{\sqrt{2}}(|\uparrow,\downarrow\rangle + |\downarrow,\uparrow\rangle)\,, \\ |1,1\rangle &= |\uparrow,\uparrow\rangle\,, \\ |1,-1\rangle &= |\downarrow,\downarrow\rangle\,. \end{aligned} \tag{1.4}$$

1.3.1 Ps Formation

Although there is evidence for extra-terrestrial positronium in the form of annihilation radiation originating in the Galactic centre [Leventhal *et al.*, 1978], the apparent scarcity of positrons, in addition to the ephemeral nature of Ps, renders it a vanishingly rare substance on earth. Notwithstanding an inherent predisposition for non-existence, Ps atoms may be engineered with relative profusion in the laboratory, where in general its production is attributable to simple electron capture from collision between a positron and target atom or molecule (X),

$$e^+ + X \rightarrow Ps + X^+\,. \tag{1.5}$$

When a positron enters a gaseous medium it will rapidly slow due to inelastic collisions. At energies below the lowest excitation energy of the atoms/ molecules the cross section for Ps formation is greatly enhanced [Massey and Mohr, 1954; Sperber *et al.*, 1992], provided that the positron's kinetic energy (E_+) is still above the ionisation energy of the medium (E_i), less the Ps binding energy,

$$E_+ \geqslant E_i - E_n\,. \tag{1.6}$$

Ps can similarly form in the bulk of solid insulators. Although screening of the positron charge by conduction electrons inhibits such occurring in the bulk of metals, Ps formation may yet take place in the low density electron cloud at a

metal's surface. The average Ps lifetime within a dense medium is significantly reduced from that in vacuum, due to either direct annihilation of the positron component with an atomic electron, or collisions involving spin exchange which effectively mixes the o-Ps and p-Ps states.

Positronium formation was first demonstrated by Deutsch [1951] through measurement of positron lifetimes in various gases, and identification of an o-Ps component that was largely independent of gas pressure. The argument was reinforced by gamma-ray spectroscopy, reasoned upon the principle that the ratio of 2γ to 3γ annihilation of free positrons is roughly 372:1, whereas the equivalent for Ps annihilation is dominated by the spin ratio of p-Ps and o-Ps (equation 1.4), and is therefore approximately 1:3, [Debenedetti and Corben, 1954].

The formation of Ps has since been reported in a great variety of materials, including: powdered oxides [Paulin and Ambrosino, 1968]; solid surfaces [Canter *et al.*, 1974]; mesostructured silica films [Liszkay *et al.*, 2008b]; and aerogels [Edwardson *et al.*, 2011]. For a detailed discussion of Ps emission to vacuum from porous SiO_2, see section 2.5.1.

Advances in positron beam and Ps formation technologies has facilitated discovery of the positronium molecule (Ps_2) [Cassidy and Mills, 2007]. It is envisioned that ever increasing Ps densities and developments with laser cooling [Liang and Dermer, 1988], may eventually realise a Bose-Einstein condensate of positronium, which could - in principle - be used to create an intense pulse of coherent annihilation photons [Mills, 2002].

1.3.2 Ps Spectroscopy

With an elementary two-body composition and leptonic purity, a complete QED description of the positronium atom has been applied to calculations of its fine structure state energies and lifetime in vacuum (in particular $n = 1, 2$ - see figure 1.5) - a historical review of the theoretical developments is given by Rich [1981]. Over the course of the last half a century or so the precision of these calculations

has advanced to exceed that which has been measured experimentally, with only a few exceptions - e.g. the Doppler-free measurement of the $1^3S - 2^3S$ interval by Chu *et al.* [1984]. This is in contrast to most other realms of atomic physics, due not only to the relative simplicity of the theoretical model, but also the experimental difficulty in isolating positrons from matter.

Positronium, being an uniquely light element, will undergo significant Doppler shifts at relatively low kinetic energies. This effect can limit the resolution of spectroscopic measurements, though was deliberately exploited by Mills [1981] in discovery of the positronium negative ion (Ps^-), observing blue shifted annihilation gammas from Ps^- accelerated in an electric field.

As an extended consequence of positronium's susceptibility to such shifts, a thermal distribution of Ps atoms will exhibit atomic transition frequencies (ν_0) with line-shapes that are typically dominated by Doppler broadening - assuming a Maxwellian energy distribution, the profile of which is given as,

$$P(\nu)\,\mathrm{d}\nu = \frac{1}{\nu_0}\sqrt{\frac{mc^2}{2\pi k_B T}}\exp\left(\frac{mc^2(\nu-\nu_0)^2}{2k_B T\nu_0^2}\right)\mathrm{d}\nu\,, \tag{1.7}$$

i.e. a Gaussian line-shape centred about ν_0 with a full width at half the maximum,

$$\Delta\nu_{\mathrm{FWHM}} = \nu_0\sqrt{\frac{8k_B T\ln 2}{mc^2}}\,. \tag{1.8}$$

For instance, the 243 nm Lyman-α transition of Ps has a natural linewidth of 50 MHz (Lorenzian FWHM), whereas a thermal distribution with a temperature of 300 K has a Doppler width of 460 GHz.

The broad Doppler linewidth of the Lyman-α interval means that laser excitation of the transition is complicated by the fact that typical laser technologies produce linewidths which are narrow in comparison; consequently having little frequency overlap. This issue was addressed by Ziock *et al.* [1990b], who pumped the $1^3S - 2^3P$ transition using a specially adapted frequency doubled dye-laser with a linewidth of $\approx$ 350 GHz. Excitation events were inferred by a measured reduc-

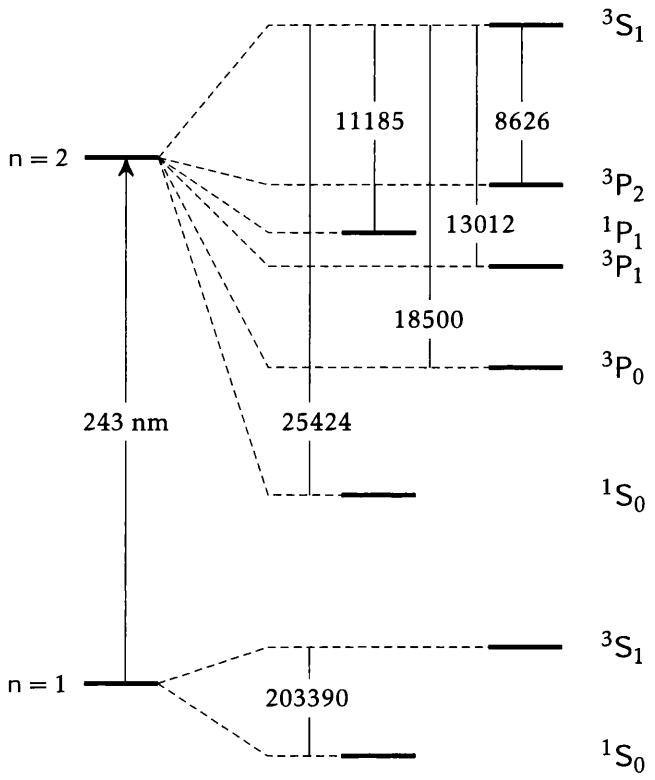

Figure 1.5: Schematic diagram of the lowest energy levels of positronium ($^{2s+1}L_J$). The numbers representing the differences between energy levels are in MHz. The Lyman-α wavelength indicating the distance between the levels n = 1 and n = 2 is in the optical ultraviolet region and given in nm. [reproduced from Ley, 2002, Fig. 1, p. 302]

tion in the mean Ps lifetime, which was attributed to Zeeman mixing of the triplet population with singlet states (magnetic quenching). See Dermer and Weisheit [1989] for a perturbative QED theory applied to radiative transitions between the $n = 1$ and $n = 2$ states of Ps in electric and magnetic fields.

Rydberg Ps

The majority of experimental work with positronium performed to date has been restricted to the $n = 1$ and $n = 2$ states, however there is significant motivation for pursuing a means to obtain highly excited ($n \gtrsim 10$) so-called Rydberg states (Ps*) - not least because the lifetime against self-annihilation scales as $\mathcal{O}(n^3)$.

An interesting application of Rydberg Ps is in the formation of antihydrogen,

$$Ps^* + \bar{p} \rightarrow \overline{H} + e^- , \tag{1.9}$$

where the cross section for such a process scales as $\mathcal{O}(n^4)$ [Charlton, 1990]. This technique has been demonstrated by Storry *et al.* [2004], who utilised collisions between laser pumped Cs* atoms and positrons to create Ps*, which were subsequently passed through a plasma of $\bar{p}$'s to form $\overline{H}$ (equation 1.9). Future potential applications for Ps* include: loading of positrons and electrons into a stellerator [Sunn Pedersen *et al.*, 2012]; formation of Ps-atom bound states [Cheng *et al.*, 2011]; gravitational measurements of positronium in free fall [Mills and Leventhal, 2002].

The first observation of resonantly excited Rydberg states of positronium was made by Ziock *et al.* [1990a]. They saturated the $1^3S - 2^3P$ transition with a 243 nm laser, and from $n = 2$ the high-n states were optically pumped with a tunable infra red dye-laser. Using deviations in the measured lifetime to infer excitation, this technique resolved transitions to $n = 14$ and $n = 15$. A more recent experiment based upon similar methods was able to resolve levels $n = 10$ to $n = 15$, with a significantly higher signal-to-noise ratio [Cassidy *et al.*, 2012].

1.4 Thesis Outline

This introduction was written to give an overview of the field of positron and positronium physics, with a view to putting the work presented herein into context with the relevant historical - and contemporary - experiments. In the following chapters we outline the apparatus, methodology and results of an investigation into laser excitation of the Doppler broadened Lyman-α transition of the positronium atom:

Chapter 2 provides an overview of the Swansea University positron beamline and its operation. This includes a discussion of the vacuum system, as-well as the magnets used to guide positrons along it. The main experimental regions are discussed in some detail, including the positron source, two-stage accumulator, and the positronium converter. Furthermore, the rotating-wall technique (positron cloud compression in a rotating dipole field) is reviewed, and the detectors used to characterise the accumulated clouds and to measure the positronium decay rate are also described.

Chapter 3 is dedicated to the UV laser which was built and characterised as part of this study. This includes: an overview of the requirements for efficient excitation of Ps atoms; a description of the main components of the UV laser hardware; calibration of the spectrometer used to measure the laser wavelength; an estimate of the linewidth of the UV beam.

Chapter 4 presents techniques for manipulating positrons in the accumulator. These are employed to explain phenomena we observe as a consequence of simultaneous accumulation and compression of positrons. Additionally, this chapter contains an investigation into the effect of the build-up of space-charge on the positron accumulation dynamics.

Chapter 5 discusses techniques employed in the creation of positronium with silica targets, and the detection methods used to find the amount Ps emitted to vacuum as a fraction of incident positrons. Methods for exciting Ps atoms with a UV laser and inference of such are also given. Furthermore, we here present results of some preliminary spectroscopic measurements of the Doppler width of the $1S - 2P$ transition.

Chapter 6 summarises the work presented in this thesis, and further outlines some suggestions for advancing this proof-of-concept study.

Chapter 2

Positron Beamline

2.1 The Beamline

The Swansea University positron beamline has been in development since the year 2000, with the first positron source installed by 2002, and a novel two-stage buffer-gas positron accumulator operating within a year [Clarke *et al.*, 2003, 2006]. The design and assembly of the beamline has been conducted by a number of post-docs and postgraduate students, under the supervision of Prof. Michael Charlton and Dr Dirk Peter van der Werf. The principal purpose of the beamline is to research, develop and advance techniques in positron accumulation and positronium studies, for application in antihydrogen production in association with the ATHENA and ALPHA collaborations (CERN).

The positron beamline is a 5 m long modular vacuum system, comprised of the positron source chamber followed by four six-way DN160 conflat crosses (henceforth notated with Latin numerics and numbered sequentially as placed from the source), interconnected via various pumping restrictions and vacuum tubes. The aforementioned positron accumulator is located between crosses I and II. A number of coils and solenoids are used to create an axial magnetic field along the system, guiding positrons from the source and through the apparatus - see section 2.1.2

for further details. The vacuum chambers, high-vacuum pumps, and magnets are illustrated in cross section, in figure 2.2a.

In summary, the contents and primary function of each cross are as follows:

Cross I houses an electron gun which is used for alignment purposes and for testing the accumulator with electrons.

Cross II contains a stainless-steel plate with a 2 mm diameter hole which is used for diagnostics of the positron beam and accumulated clouds.

Cross III contains a Microchannel Plate (MCP) and phosphor screen assembly (see section 2.6.1) that is employed in imaging particle clouds.

Cross IV accommodates the positronium conversion target (porous silica - see section 2.5.1), and laser interaction region.

The e-gun, plate, MCP and silica target are all mounted to vertically actuating linear manipulators, which allows for each to be manually lowered into, or removed from, the path of the beam.

2.1.1 Vacuum System

In order to prolong the lifetime of the antiparticles - naturally very short in a matter based lab - the beamline is pumped to ultra-high vacuum using a combination of cryo and turbo pumps (table 2.1). The two cryo pumps are run with a single *APD Cryogenics* HC-4 compressor, and the turbo pumps are backed with *Edwards Vacuum* XDS10 scroll pumps. The vacuum system is depicted topologically in figure 2.1.

The pressure within the beamline is monitored using a combination of eleven *Pfeiffer Vacuum* gauges (table 2.2). Capacitance gauges are utilised for the higher pressure range of 10^{-2} mbar to 10^{3} mbar (e.g. gas lines); Pirani gauges are used for the mid range pressures of 10^{-4} mbar to 10^{2} mbar; and cold-cathode ion gauges

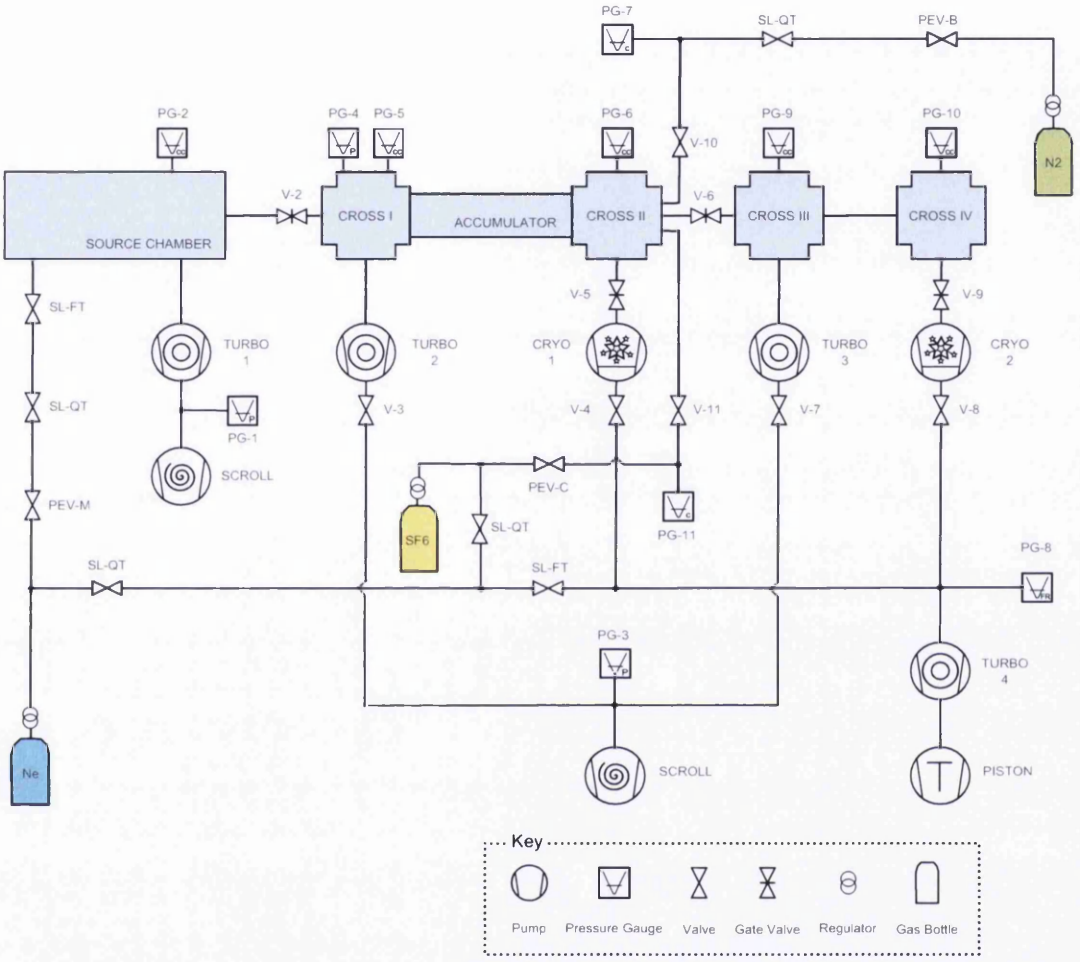

Figure 2.1: Topological diagram of the vacuum and gas systems for the positron beamline - key inset. Includes: pressure gauges (PG), numbered 1-11, each marked in accord with type (Cold Cathode (CC), Pirani (P), Capacitance (C), or Full Range (FR)); vacuum pumps, type indicated and numbered; pneumatic valves (V), numbered 1-11; piezo-electric valves (PEV), for the moderator (M), buffer gas (B) and cooling gas (C) flow control; Swagelok® full-turn (SL-FT) and quarter-turn (SL-QT), manual valves.

operate in the lower range of 10^{-9} mbar to 10^{-3} mbar. The full-range gauge combines a Pirani and cold-cathode gauge in a single unit. All of the gauges are read using two 6-channel MaxiGauges,™ linked via RS485 serial to a PC for display and data logging (see section A.1).

Eleven remote controlled, pneumatic valves are used to manage the pumping of the system, and to allow for isolation of the three distinct sections: the source chamber; the accumulator (crosses I and II); the MCP and laser interaction region (crosses III and IV). Control of the valves is hardware interlocked against potentially damaging operation by means of a simple relay network, which employs switches from each MaxiGauge™ that respond to pressure readings based upon user specified limits. For instance, valve-2 connects the source chamber to the accumulator and is inhibited from being open if PG-2 reads above 1×10^{-7} mbar.

The moderator growth (section 2.2), accumulator (section 2.3) and rotating wall (section 2.4), require a variety of gases be introduced into the system, in a controlled and reproducible manner. This is achieved with three separate regulated gas supplies, connected to the beamline through a system of 1/4″ Swagelok® pipes and valves. The flow of the gases is regulated using *Key High Vacuum* PEV-1 piezoelectric valves, which can be remotely opened to a variable degree with an applied voltage. The control voltages are provided by $\times 14$ amplification of analogue output channels from a *National Instruments* PCI-6221, and are set using a Labview™ software PID control. The readings of pressure gauges 2, 7 and 11 are used as feedback for the moderator, buffer and cooling gas PID controllers respectively.

2.1.2 Magnetic Fields

Positrons are guided along the beamline using the magnetic fields created in passing electric currents through a number of coils and solenoids - see figure 2.2. The first set of magnets consists of three "pancake coils", which are positioned to form a step in the field lines that acts as an energy filter, arranged to steer the low-energy moderated positrons from the source mount and into the first pumping restriction.

Table 2.1: Summary of the beamline high-vacuum pumps.

Pump	Manufacturer	Model	Location
Turbo-1	Pfeiffer Vacuum	TMU 520	Source Chamber
Turbo-2	Oerlikon Leybold	Turbovac 340 M	Cross I
Cryo-1	APD Cryogenics	AP-6	Cross II
Turbo-3	Oerlikon Leybold	Turbovac 340 M	Cross III
Cryo-2	APD Cryogenics	AP-6	Cross IV
Turbo-4	Pfeiffer Vacuum	TMU 064	Backing Line

Table 2.2: Summary of the beamline pressure gauges. Typical readings are base pressures when the accumulator is not running and no moderator is present; where relevant, the contrariwise values are juxtaposed in brackets. A '<' ('>') comparator indicates typical readings as under-range (over-range). The capacitance gauges 7 & 11 are not calibrated and are only used as feedback for PID control.

Gauge	Type	Location	Typical Reading [mbar]	
1	Pirani	Turbo-1 Backing	3×10^{-2}	
2	Cold Cathode	Source Chamber	1×10^{-9}	(5×10^{-8})
3	Pirani	Turbos 2 & 3 Backing	5×10^{-2}	
4	Pirani	Cross I	$< 1 \times 10^{-3}$	
5	Cold Cathode	Cross I	$< 2 \times 10^{-9}$	(1×10^{-5})
6	Cold Cathode	Cross II	1×10^{-9}	(4×10^{-6})
7	Capacitance	Buffer Gas Line	$> 1 \times 10^{3}$	(3×10^{2})
8	Full Range	Backing Line	2×10^{-6}	
9	Cold Cathode	Cross III	$< 2 \times 10^{-9}$	(2×10^{-7})
10	Cold Cathode	Cross IV	1×10^{-9}	(2×10^{-8})
11	Capacitance	Cooling Gas Line	$> 1 \times 10^{1}$	(4×10^{-1})

(a)

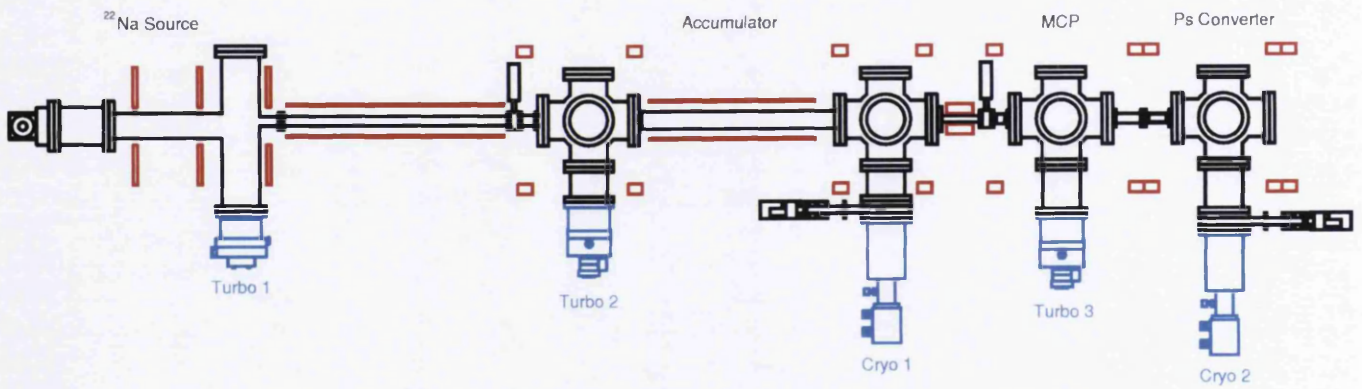

(b)

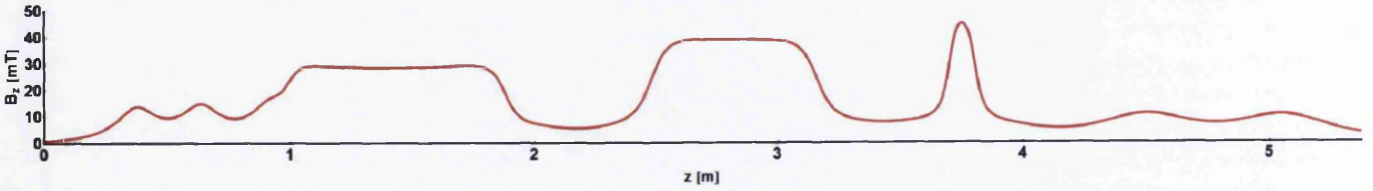

Figure 2.2: (a) Schematic in cross section (approx. to scale) of the positron beamline vacuum system (black), high-vacuum pumps (blue), and magnetic coils/ solenoids (red) - *N.B.* each coil is aligned to be approximately coaxial with the long axis of the vacuum system. (b) On-axis, axial component of the magnetic field for the coil specifications outlined in table 2.3. Calculation performed using *Wolfram* Mathematica® and Radia (a magnetostatics modelling package by ESRF).

Encasing the long pumping restriction, solenoid-1 is used to transport positrons from the source chamber into cross I, from where the beam enters the accumulator (section 2.3.2) - the magnetic field for which is provided by solenoid-2. Clouds of positrons ejected from the accumulator are guided into cross III using a short, fan cooled transport coil. This coil increases the field significantly in the region of a narrow pumping restriction, compressing clouds therein and thereby increasing transport efficiency into cross III.

Additionally, nine large diameter steering coils are positioned either side of each cross in a repeating (near) Helmholtz configuration, maintaining a continuous field along the beamline. A set of two pairs of such coils are utilised to generate the field in cross IV. Adjustments to the position and orientation of each coil are made to best centre the beam path throughout the apparatus. For a summary of the coil specifications see table 2.3.

Table 2.3: Summary of the beamline magnet specifications and nominal applied current.

Coil(s)	Dimensions [mm]			Turns	I [A]
	Length	Inner Radius	Outer Radius		
Pancake Coils (1-3)	18	72	238	160	16
Solenoid-1	890	60	68	888	22
Solenoid-2	680	73	81	680	30
Transfer Coil	103	22	62	40	100
Steering Coils (1-9)	60	263	300	400	6

The coils are powered using a combination of current supplies, of which that for solenoid-2 (*Aim and Thurlby Thandar Instruments* QPX1200) is remotely steered using LAN Ethernet communication. Water cooling is provided to the pancake coils and two solenoids using a closed cycle water circulation and refrigeration system, running at roughly 16 °C and 6 bar. The steering coils are not actively cooled.

It is instructive to note the effect that the non-uniform magnetic field of the

beamline has on the distribution of particles travelling along it. In general, the transport of moderated positrons is slow enough through the changing fields to be considered adiabatic, as such conserving the so-called *first adiabatic invariant of plasma physics*, namely the magnetic moment of a gyrating particle:

$$\mu = \frac{\frac{1}{2}mv_{\perp}^2}{B_z}. \tag{2.1}$$

From equation 2.1 the perpendicular (radial) position of a given positron travelling between two points, can be determined from its initial position (r_0, z_0) and the relative difference in magnetic field,

$$r = r_0\sqrt{\frac{B_z}{B_{z_0}}}. \tag{2.2}$$

In qualitative terms, the particles simply follow the magnetic field lines, diverging in regions of low field and compressing in regions of high field. A consequence of such is that a positron cloud inside of the accumulator will nominally have a radius which is a factor of 2.6 smaller than will be imaged at the MCP - see section 2.6.1.

2.2 Positron Source and Moderation

The positron source for the beamline is the sodium radioisotope ^{22}Na (see section 1.2.1), with an activity of 2 GBq at the date of manufacture by *iThemba Labs* (South Africa), April 2012. The radioactive salt crystal is held in a tantalum backed casing that is capped with a 5 μm titanium foil. This configuration exploits backscattering from the high-Z tanatalum base to maximise forward projection (through the foil) of the positrons, which would otherwise be emitted isotropically.

The source capsule is attached to a mount (figure 2.3) which has been designed to be thermally sunk with, yet electrically isolated from, the cold-finger of a *Sum-*

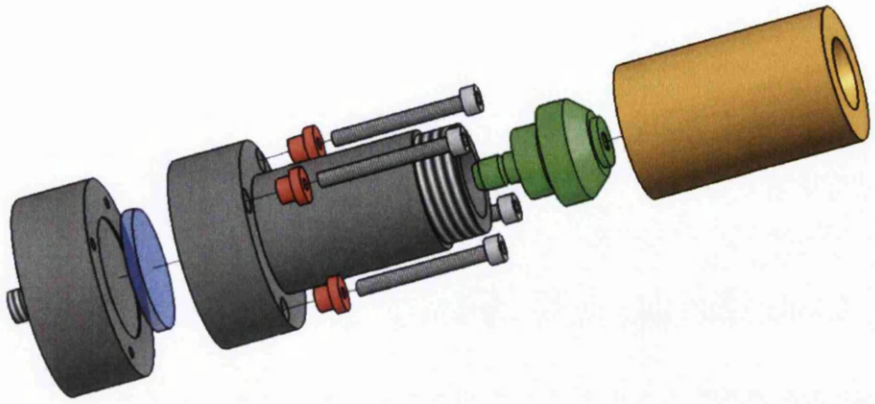

Figure 2.3: False colour, exploded view schematic of the source-capsule (green), moderator cone (gold) and Elkonite® base (grey). Electric isolation is provided by the sapphire disc (blue) and PEEK (polyether-ether-ketone) spacers (red), [adapted from Isaac, 2010, Fig. 2.2, p. 18].

itomo Cryogenics RDK408-L2 cold-head. Electrical isolation is achieved with a disc of insulating sapphire, enabling biasing of the source and thereby selection of the positron beam energy. Discs of indium foil are employed to achieve good thermal contact between the material interfaces, e.g. the sapphire disc and Elkonite® base. A cartridge heater facilitates temperature adjustment and annealing during moderator growth. The heater is powered by a *Lakeshore* Model 331 temperature controller and regulated using the inbuilt PID, with feedback provided by a Chromel-AuFe thermocouple.

During moderator growth the source mount is cooled to between 5 K and 10 K, and Ne gas admitted to the chamber at a pressure regulated to $\sim 2 \times 10^{-3}$ mbar on PG-2. A copper cylinder with a conical hollow is attached to the front of the source mount; this substrate is shaped to maximise the yield of positrons which are epithermally moderated in passing through the solid Ne that condenses on its surface [Khatri *et al.*, 1990].

The energy-spread of the fraction of the positrons which are moderated is re-

duced from approximately 0.5 MeV to 1 eV, with a mean energy typically selected (with an applied bias) to be 50 eV. A CsI/diode detector (see section 2.6.2) connected to a *Canberra* 2015A AMP/TSCA and *NI* PCI-6221 counting input, indicates the rate of positrons annihilating at valve-2 with a total efficiency of 0.4 %. For seemingly identical growth parameters, the slow yield of moderators is found to vary by as much as 40 %. Figure 2.4 shows an example moderator growth curve, illustrating the rate of moderated positron emission as a function of growth time; a good moderator will have a slow yield in the region of 5 million e^+/s.

In the event that the polarity of the source bias is reversed (e.g. -50 V), secondary electrons excited from the moderator are emitted instead of positrons [see Coleman, 2000, p. 165]. The energy distribution of the electrons is comparable to moderated positrons, however the rate of electron emission is estimated to be a factor of roughly 100 greater. This technique provides a convenient pre-aligned electron source which can be used, for instance, in testing the MCP.

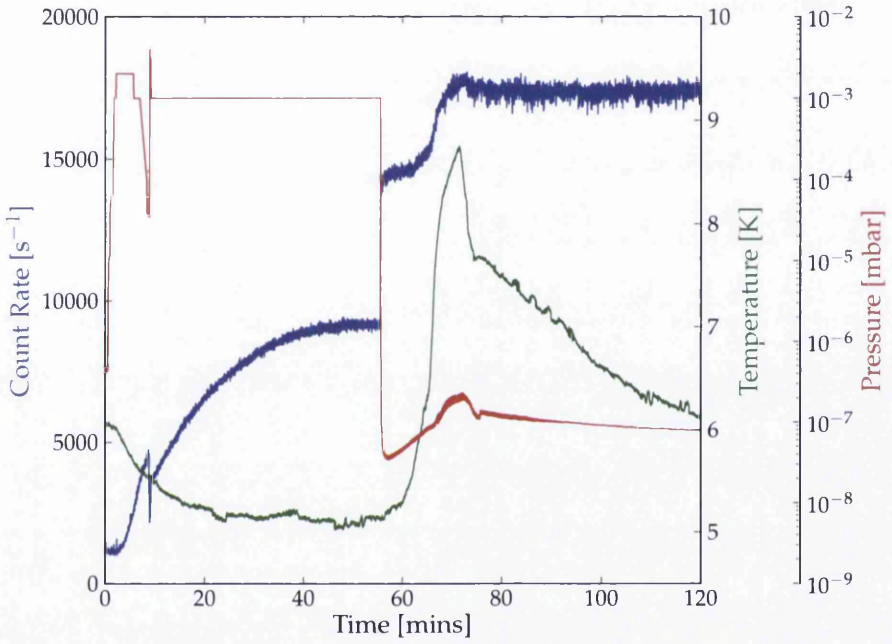

Figure 2.4: Example moderator growth curve. The count rate (blue) increases steadily during the growth procedure, then rises sharply when the Ne gas is removed. The count rate increases by a further 10 % as the moderator is annealed.

2.3 Positron Accumulator

The heart of the positron beamline and crux upon which the experimental studies described herein are founded, is a two-stage buffer gas accumulator [Clarke *et al.*, 2006]. The origins and principles of positron accumulation have been briefly outlined in section 1.2.3, and the specific details of the Swansea positron beamline accumulator are given in section 2.3.2.

2.3.1 Penning Traps

The Penning trap is the basis for the accumulator design, and as such the charged particle dynamics outlined in this section are pertinent to the mechanics of accumulating positrons, as will be discussed in the subsequent sections.

The invention of the Penning trap is by and large attributed to Dehmelt [1968], though its name is derived from the "cold-cathode" ion gauge devised by Penning [1936], which employs a similar configuration of magnetic and electric fields to accrue a measurable ion current in an electrical discharge tube.

The Penning trap is widely used in the fields of ion trapping, non-neutral plasmas and precision mass-spectrometry. The typically long lifetimes of trapped species enables near indefinite confinement of even a single particle [Wineland *et al.*, 1973], as was required in exquisite measurement of the electron anomalous g-factor [Hanneke *et al.*, 2008]. The extreme precision of such measurements is contingent upon reliably reproducing what is generally refereed to as the ideal Penning trap - outlined in the next section.

Much of the following overview is compiled from chapter 3 of *Charged Particle Traps*, by Major, Gheorghe and Werth [2005]. For further details of trapping dynamics see the comprehensive Penning review article by Brown and Gabrielse [1986].

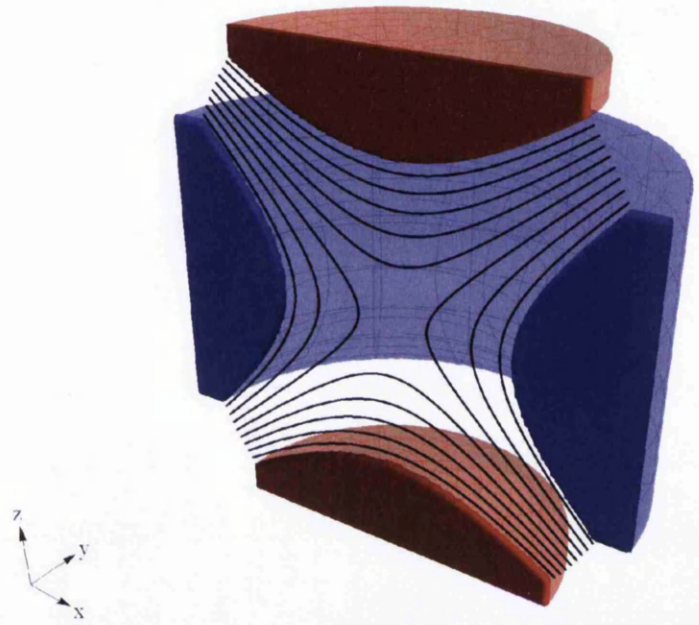

Figure 2.5: Truncated ring electrode (blue) and hyperbolic end-caps (red) of a Penning trap displayed in cross section. Overlaid in the plane of xz ($y = 0$) are lines of equipotential illustrating the quadratic electric potential produced when the ring is biased w.r.t. the end-caps. A uniform magnetic field is aligned to the z-axis.

The Ideal Penning Trap

The Penning trap confines charged particles in the axial direction with an electric potential ϕ, that is a minimum at the origin along z. In the case of the ideal Penning trap a ring electrode biased with U_0 and two grounded, hyperbolic end-caps (figure 2.5) produce a harmonic potential of the form,

$$\phi(r,z) = U_0 \frac{2z^2 - r^2}{2z_0^2 + r_0^2}, \tag{2.3}$$

where $2z_0$ and r_0 is the minimum separation between the two end-caps and minimum inner radius of the ring electrode respectively. A positively charged particle bounded therein would undergo axial harmonic oscillations characterised by an angular frequency of,

$$\omega_z = \sqrt{\frac{4qU_0}{m(2z_0^2 + r_0^2)}}. \tag{2.4}$$

Equation 2.3 describes a saddle point potential centred at the origin that, whilst forming a minimum in z, also diverges from a maximum in the radial directions and thus cannot fully confine the particles. Consequently, a homogeneous, axial magnetic field $\vec{B} = B\hat{z}$ is superposed to obtain confinement in the radial plane.

In isolation such a magnetic field would induce cyclotron orbits with an angular frequency,

$$\Omega_c = qB/m, \tag{2.5}$$

however in combination with the perpendicular electric field $\vec{E} = \vec{\nabla}\phi$ the radial motion becomes somewhat more complex. In the $\vec{E} \times \vec{B}$ fields the cyclotron motion is slightly perturbed to orbits with a modified cyclotron frequency ω_+, in addition to which the particles experience a slower magnetron orbit with frequency ω_-, where

$$\omega_\pm = \frac{1}{2}\left(\Omega_c \pm \sqrt{\Omega_c^2 - 2\omega_z^2}\right). \tag{2.6}$$

The three motional frequencies form a set of eigenvalues that are characteristic

of the trap and trapped species, and which generally conform to the hierarchy,

$$\omega_+ \gg \omega_z \gg \omega_- \,. \tag{2.7}$$

The combined cyclotron and magnetron motion traces an epitrochoid in the radial plane. The full three dimensional motion of a single charged particle confined in an ideal Penning trap is illustrated in figure 2.6.

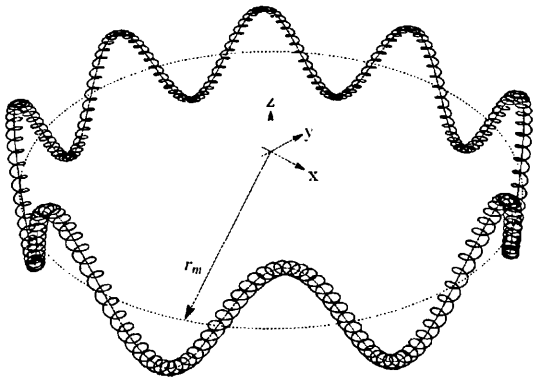

Figure 2.6: The motion of a single charged particle confined in a Penning trap (black), the component magnetron motion (blue) with radius r_m, and the so-called "guiding centre" combination of the axial and magnetron motion (red).

The Penning-Malmberg Trap

Although conceptually simple, the ideal Penning trap has some practical disadvantages - for instance, without modification the design does not offer any path to load particles into the trap. This is addressed by the so-called Penning-Malmberg trap, where both the ring electrode and end-caps are replaced by coaxial cylindrical electrodes (figure 2.7), allowing for easy loading along the magnetic field lines [Malmberg and Driscoll, 1980].

Furthermore, the simple geometry of the Penning-Malmberg trap lends it to extension to more complex systems, where for instance an asymmetric well is

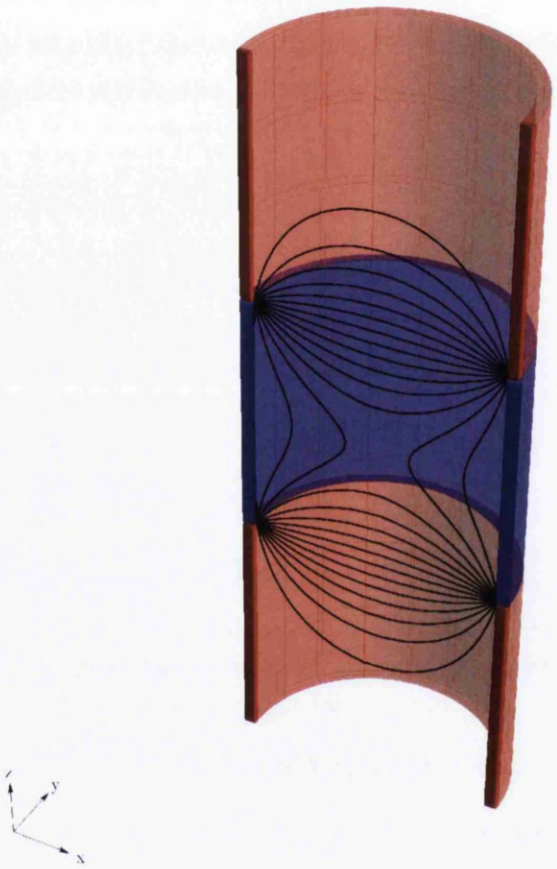

Figure 2.7: The ring electrode (blue) and end-caps (red) of a Penning-Malmberg trap displayed in cross section. Overlaid in the plane of xz ($y = 0$) are lines of equipotential for the approximately quadratic electric potential produced when the ring is biased w.r.t. the end-caps. A uniform magnetic field is aligned to the z-axis.

desired e.g. the Surko trap (section 1.2.3), or where oppositely charged particles need be held in close proximity, as with antihydrogen synthesis [Quint *et al.*, 1993].

The electric potential formed by the cylindrical electrodes is non-trivial to calculate, but can be found by solving the Laplace equation,

$$\nabla^2 \phi = 0\,, \tag{2.8}$$

for given boundary conditions of the electrode geometries and applied voltages. In the simplest case of the three electrode trap, approximated for convenience as having grounded end-caps which are closed at $z = \pm L_z$, an analytical solution can be found,

$$\phi(r,z) = \frac{2U_0}{L_z} \sum_{n=0}^{\infty} \frac{\sin(k_n z_0)}{k_n I_0(k_n r_0)} I_0(k_n r) \cos(k_n z) \tag{2.9}$$

where r_0 is the inner radius of the electrodes, $2z_0$ is the length of the centre electrode, $k_n = \pi(n + 0.5)/L_z$ and I_n is the modified Bessel function of the first kind. So long as the end-caps are at least comparable in length to the centre electrode, the value of L_z only weakly influences the result; the solution is also generally found to compare closely to numerical calculations for the open end-cap configuration.

To first approximation and for small r and z, equation 2.9 is a quadratic saddle point (i.e. similar to equation 2.3), however there are higher order corrections which may be minimised by use of additional compensation electrodes - for an analysis of quadratic field compensation in many electrode Penning-Malmberg traps, see Estrada [2002]. Two important consequences of the non-ideal properties of this potential are that, unlike in the harmonic case, ω_z is not independent of the parallel energy of the particles, nor is it independent of the radial position (namely, the amplitude of the magnetron orbit r_m).

Whilst more complex configurations can often be solved explicitly, a good approximation can be made to coaxial, many electrode systems by superposition of the three electrode solutions for each electrode contribution with appropriate translations in z; provided that r_0 is consistent (z_0 need not be) and the spacing

between adjacent electrodes is negligible. Furthermore, as equation 2.9 is linear with the applied potential U_0, the solution for a unit bias can be trivially scaled to give the solution for any given applied voltage. For trap configurations with irregular electrode geometries, specialised numerical Laplace solvers are often used, e.g. SIMION®.

2.3.2 Two-Stage Buffer Gas Accumulator

The two-stage buffer gas accumulator is of the Surko trap ilk (see section 1.2.3). A stack of cylindrical electrodes (figure 2.8) encased within solenoid-2 (table 2.3), provide axial and radial confinement respectively. The aluminium electrodes are gold-plated and each is electrically insulated from its neighbours with 2 mm sapphire balls. The solenoid has a typical internal magnetic field of ~ 35 mT.

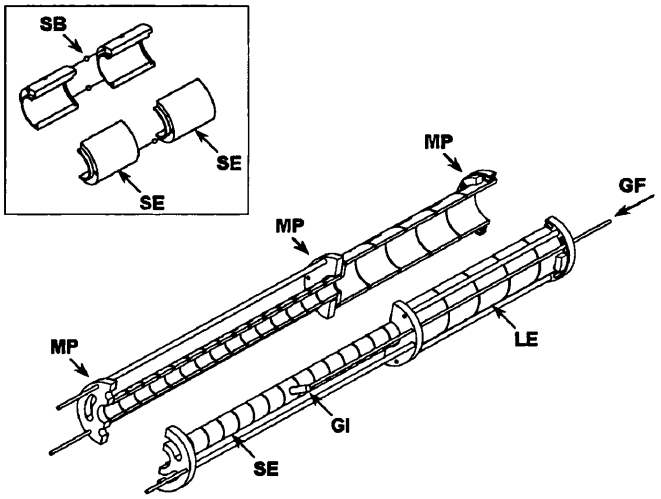

Figure 2.8: Cutaway diagram of the positron accumulator consisting of 15 small electrodes of internal diameter of 16 mm and five large electrodes of internal diameter of 41 mm, insulated from one another by three 2 mm diameter sapphire balls (see insert). The mounting plates were precision machined to fit snugly inside the 66 mm internal diameter vacuum tube. Key: GI, gas inlet; GF, gas flow; SB, sapphire balls; MP, mounting plates; LE, large electrodes; SE, small electrodes. [Clarke *et al.*, 2006, Fig 2., p. 2]

Incident positrons are slowed, and thus trapped, by inelastic collisions with a low density N_2 gas, which is admitted into the first stage of the accumulator at a pressure of $\sim 10^{-3}$ mbar. Nitrogen is uniquely suited for such, having a relatively large cross section for electronic excitation at incident energies ~ 10 eV, relative to loss mechanisms, e.g. positronium formation [Marler and Surko, 2005; Sullivan *et al.*, 2001]. The base of the electric potential well (figure 2.9) is located in the second stage of the accumulator, whereat positrons eventually accumulate. The larger diameter of the second stage electrodes, in addition to rapid pumping, results in lower pressures ($< 10^{-4}$ mbar), and consequently longer e^+ lifetimes, in the region of accumulation. For further details see Clarke *et al.* [2006].

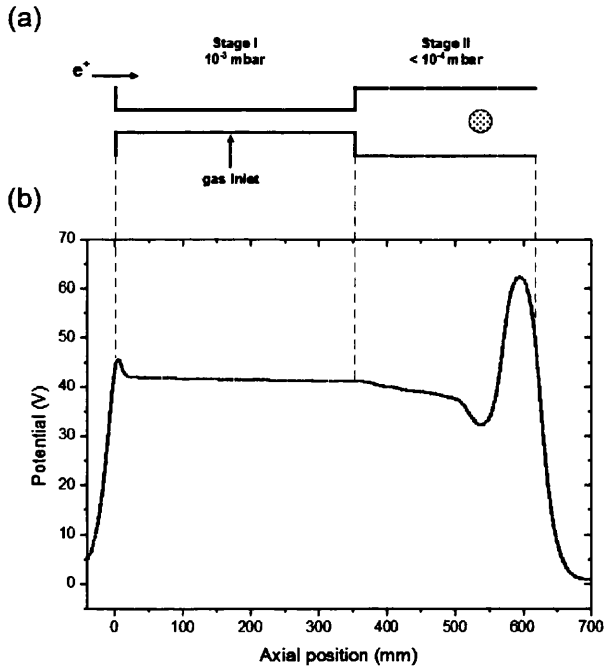

Figure 2.9: (a) Schematic illustration of the electrode structure of the accumulator. (b) The electrical potential along the axis of the trap. [Clarke *et al.*, 2006, Fig 3., p. 3]

The biases applied to the electrodes are selected externally using a combination of voltage supplies and a voltage divider. The latter is used to bias fourteen of

the first stage electrodes with a linear gradient potential; reducing the number of supplies required for which to two (E1,E2). The other supplies number those for the entrance electrode (E0) and the five electrodes of the second stage (E3-E7). Often the exit electrode supply (E7) is connected via a 'fast pulser,' which facilitates rapid gating (20 ns) of the bias with a digital trigger.

Each of the eight voltage supplies are provided by custom $\times 14$ amplifiers (with a slew rate of 3 µs), that act on the ± 10 V analogue outputs of an 8-channel, 12-bit *NI* PCI-6713. Dynamic control of the AO device is facilitated by on-board memory with a 16,384 sample buffer, triggered at a maximum rate of 1 MS /s. The triggers are ministered from an *NI* PCI-7813R: a reconfigurable field-programmable gate array (FPGA) with a minimum step time of 37.5 ns and step resolution of 12.5 ns. The FPGA is additionally used to trigger a second *NI* PCI-6713 AO device, and to also generate digital triggers for other time critical hardware, e.g. the laser system. For an outline of the sequence software control of the FPGA and AO devices see section A.2.1.

Basic Accumulation

In the simplest case, the process of accumulation is as outlined in table 2.4. Positrons surmount the entrance electrode and accumulate in the second stage for a predetermined accumulation time, after which the entrance electrode is raised then the exit electrode lowered to expel positrons from the trap.

Table 2.4: An example of the voltage supplies used in a simple 10 Hz accumulation scheme with slow dump particle ejection.

Description	Step Time	Voltages [V]							
		E0	E1	E2	E3	E4	E5	E6	E7
Accumulate	100 ms	45	44	38	35	34	33	28	140
Close well	3 µs	140	44	38	35	34	33	28	140
Empty trap	3 µs	140	44	38	35	34	33	28	0

Positrons are accumulated in this manner with an efficiency of roughly 10 %. As the flux of moderated positrons is approximately constant at 5 million e^+/s, this results in a fixed rate of accumulation $R \approx 5 \times 10^5$ e^+ /s. The accumulation rate competes with the positron loss rate Γ, such that the rate of change of the number of particles within the trap is given by

$$\frac{dn}{dt} = R - \Gamma n , \tag{2.10}$$

from which the number of particles accumulated as a function of time is

$$n(t) = \frac{R}{\Gamma}(1 - \exp(-\Gamma t)) . \tag{2.11}$$

The above asymptotes to $\lim_{t\to\infty} n(t) = R/\Gamma$, i.e. the capture and loss rates equilibrate and the trap saturates. The mean lifetime is a useful measure, given as $\tau = 1/\Gamma$.

By adjusting the time for which positrons are accumulated and measuring the corresponding number which annihilate on the steel plate in cross III (measured using a CsI/diode detector - section 2.6.2), an accumulation curve of the form given by equation 2.11 can be produced - e.g. figure 2.10.

A least squares fit of equation 2.11 to the accumulation curve (green dashed line, figure 2.10) reveals a trap lifetime of 290 ms. The reciprocal loss rate, $\Gamma = 3.45\ s^{-1}$, is significantly higher than can be ascribed to annihilation with the buffer gas, $\Gamma_a \approx 0.55\ s^{-1}$ at 10^{-4} mbar, as estimated using,

$$\Gamma_a = \frac{e^4 n Z_{\text{eff}}}{16\pi\epsilon_0^2 m_e^2 c^3} , \tag{2.12}$$

where n is the number density of the target and Z_{eff} is the number of electrons per molecule (N_2) that are "seen" by an incident positron.

To first approximation Z_{eff} is given by the number of electrons in the target (Z), however distortions of the positron wave-function by e.g. the dipole polarisation potential of the target, can result in large correction factors [Gribakin *et al.*, 2010].

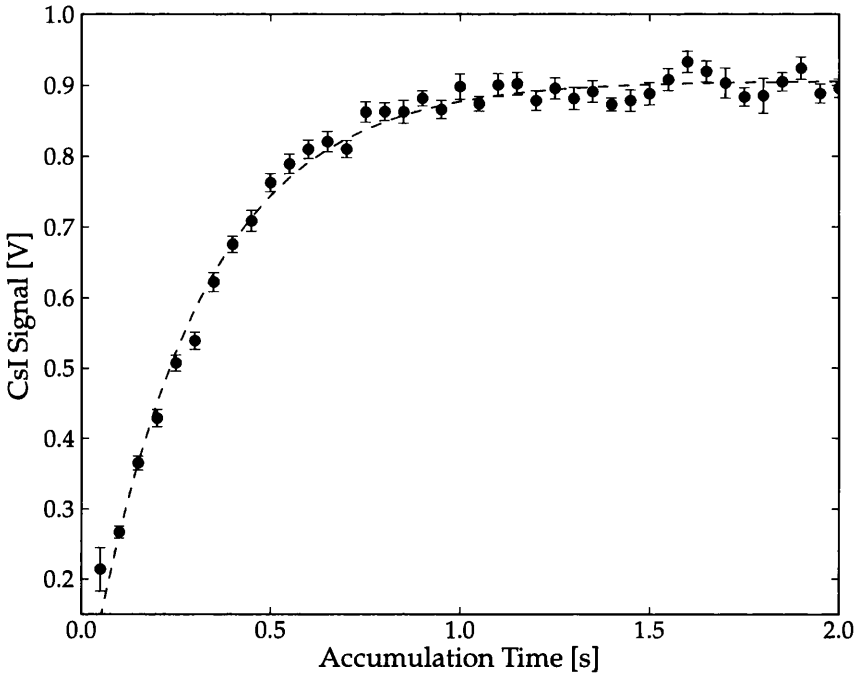

Figure 2.10: Example accumulation curve for the simple trapping scheme described in table 2.4. The green dashed line represents a fit of the form given in equation 2.11, yielding a mean lifetime $1/\Gamma = 290 \pm 4$ ms. The error-bars indicate the the statistical uncertainty derived from repeat measurements.

For certain substances (in particular hydrocarbons) Z_{eff} can be incredibly large, with enhancement factors in excess of 10^4 - see table 2.5 for a number of examples.

Table 2.5: A selection of positron Z_{eff} values, from Iwata *et al.* [1995].

Molecule	Formula	Z	Z_{eff}
Helium	He	2	3.94
Neon	Ne	10	5.99
Hydrogen	H_2	2	14.6
Nitrogen	N_2	14	30.5
Oxygen	O_2	16	36.7
Carbon tetrafluoride	CF_4	42	54.4
Carbon dioxide	CO_2	22	54.7
Sulphur hexafluoride	SF_6	70	86.2
Water	H_2O	10	319
Methanol	CH_3OH	18	1510
Benzene	C_6H_6	42	15 000
Acetone	CH_3COCH_3	32	98 400

To ensure a reasonable lifetime it is therefore strictly necessary to avoid introducing compounds with very large Z_{eff} into the vacuum system; such precludes, for instance, the use of oil pumps. Assuming adequate vigilance such that these contaminants are negligible, another plausible loss mechanism - albeit indirect - is collisions with neutrals (N_2 molecules) [Driscoll and Malmberg, 1983]. This imparts drag which expedites positrons diffusing to the inner surface of the electrodes and there annihilating.

The rotating wall technique (section 2.4) can be employed to effectively cut-off radial transport. Its use is found to significantly increase the lifetime of positrons within the trap, and furthermore can induce inward transport i.e. compression, which is employed to obtain higher density (brightness enhanced) beams.

2.4 Rotating Wall

2.4.1 Overview

The Rotating Wall (RW) technique provides a means to compress trapped species and reduce radial loss, and is widely employed in the fields of ion storage [Huang *et al.*, 1997] and nonneutral plasmas [Greaves and Surko, 2001]. What's more, the technique is now practically ubiquitous among low energy antimatter experiments, where the limited antiparticle supply renders any means to improve trap lifetimes and beam quality a valuable resource. See chapter 4 for a study of RW use in optimising positron accumulation.

The RW technique simply involves creating a dipole (or quadrupole) electric field in the radial plain of a Penning trap, and inducing the field to rotate about the trap long axis. Such a rotating field may be realised by applying time varying sinusoidal voltages to each sector of an azimuthally segmented cylindrical electrode, with an appropriate phase (φ) for each sector,

$$V_{RW}(t) = V_r \sin(\omega_r t + \varphi) , \tag{2.13}$$

where ω_r is the angular frequency of rotation, and V_r is the RW amplitude. In the case of the dipole field applied using an electrode segmented into quadrature (see figure 2.11), φ must differ by $\pi/2$ for adjoining segments.

With a finite number of electrode segments the ideal RW field is only ever approximated - to find the true potential, the Laplace equation (2.8) must be solved. The problem is simplified to two dimensions by assuming an infinitely long electrode, for which the general solution is given by,

$$\phi(r,\theta) = \frac{1}{2}a_0 + \sum_{n=1}^{\infty}\left(\frac{r}{r_0}\right)^n (a_n \cos(n\theta) + b_n \sin(n\theta)) , \tag{2.14}$$

where a_n and b_n are the coefficients of the Fourier series approximation to the piecewise boundary condition $\phi(r_0,\theta)$ (i.e. the bias potential $U_{RW} = qV_{RW}$, applied

to each segment) - explicitly:

$$\begin{aligned} a_n(t) &= \frac{1}{\pi}\int_0^{2\pi} U_{RW}(\theta,t)\cos(n\theta)\,\mathrm{d}\theta\,; \\ b_n(t) &= \frac{1}{\pi}\int_0^{2\pi} U_{RW}(\theta,t)\sin(n\theta)\,\mathrm{d}\theta\,. \end{aligned} \tag{2.15}$$

The potential of the approximately dipole field generated with a four sector electrode is illustrated in figure 2.11. The amplitude, frequency and direction of rotation of the field are intricately linked to the RW's influence on the distribution (energy and spatial) of a trapped species.

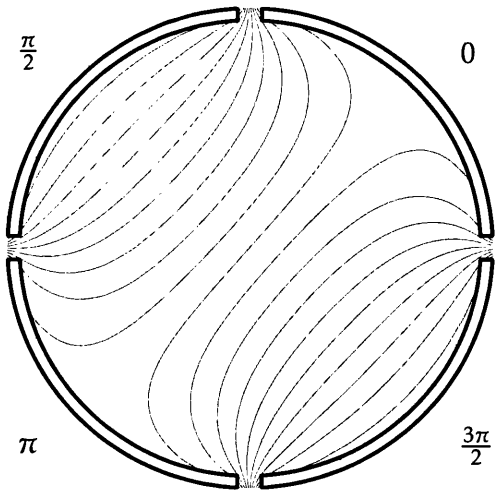

Figure 2.11: Schematic in cross section of a segmented electrode in the plane of xy, overlaid with the lines of equipotential, as given by equation 2.14 (Fourier terms up to $n = 40$). The labels indicate the phase (φ) of the sinusoidal voltage applied to each quadrant (equation 2.13).

2.4.2 Modes of Operation

Nonneutral Plasmas

The RW is shown to impart torque - and thus compress - nonneutral plasmas at specific drive frequencies, identified as corresponding to Trivelpiece-Gould modes particular to the given plasma [Anderegg *et al.*, 1998; Cluggish and Driscoll, 1995; Soga *et al.*, 2006].

These (and similar) electro-mechanical modes are characteristic of nonneutral plasmas, where the self-electric fields of the particles dominate motion and external fields are effectively screened. Such occurs when the Debye length

$$\lambda_D = \sqrt{\frac{\epsilon_0 k_B T}{n_0 e^2}}, \tag{2.16}$$

is small relative to the plasma dimensions.

Furthermore, in certain conditions a RW field has been found to compress long, dense plasmas in high magnetic fields, by coupling the RW drive frequency to the plasma $\vec{E} \times \vec{B}$ rotation frequency,

$$\omega_D = \frac{n_0 e}{2\epsilon_0 \vec{B}}. \tag{2.17}$$

Provided that the amplitude of the RW is sufficiently high to overcome the drag induced by trap asymmetries driving counter-propagating rotational modes, densities (n_0) can effectively be selected by tuning ω_r. In contrast to coupling to plasma modes, in this manner the RW is found to be effective over a broad range of drive frequencies - such is termed operation in the "strong-drive" regime [Danielson and Surko, 2005]. The maximum density obtainable is fundamentally constrained by the Brillouin [1945] limit,

$$n_B = \frac{\epsilon_0 B^2}{2m_e}, \tag{2.18}$$

however in practice this is not generally achieved.

Independent Particles

For low density clouds the particles are largely non-interacting, therefore plasma modes cannot propagate and the trapping fields dominate the particle dynamics. Compression is nevertheless observed in the so-called independent particle regime, if the RW is driven close to the axial bounce frequency of the trap [Cassidy *et al.*, 2006a; Greaves and Moxom, 2008].

A simple analytical model of independent particles RW compressed in an Penning trap has recently been reported by Isaac [2013]. The author adds a rotating dipole term,

$$\phi_r = a\frac{m}{q}z[x\,cos\,(\omega_r t) - y\,sin\,(\omega_r t)]\,, \tag{2.19}$$

to the ideal Penning potential (equation 2.3), where a is proportional to the RW drive amplitude. Furthermore, a Stokes viscous drag term $\vec{F} = -\kappa\vec{v}$, is incorporated into the model to describe cooling of the particles.

The solution to the equations of motion for such a system is reported to couple the axial and magnetron motion, which results in a reduction in the amplitude of the magnetron orbit. Such is predicted to occur at RW drive frequencies close to the upper sideband,

$$\omega_0 = \omega_z + \omega_-\,. \tag{2.20}$$

Isaac further determines the rate of compression, Γ_r, which is found to vary as a function of the cooling rate (i.e. κ), RW drive amplitude and detuning of the drive frequency from the sideband,

$$\Gamma_r = \frac{\kappa}{4}\left(1 - \sqrt{\frac{(\omega_r - \omega_0)^2}{\delta^2 + (\omega_r - \omega_0)^2}}\right)\,, \tag{2.21}$$

where $\delta^2 = a^2/\omega_z(\omega_+ - \omega_-)$.

Although idealised, the theory is found to be in excellent agreement with low density experimental studies, despite the non-ideal Penning and RW potentials which these employ [Isaac *et al.*, 2011] - see figure 2.12.

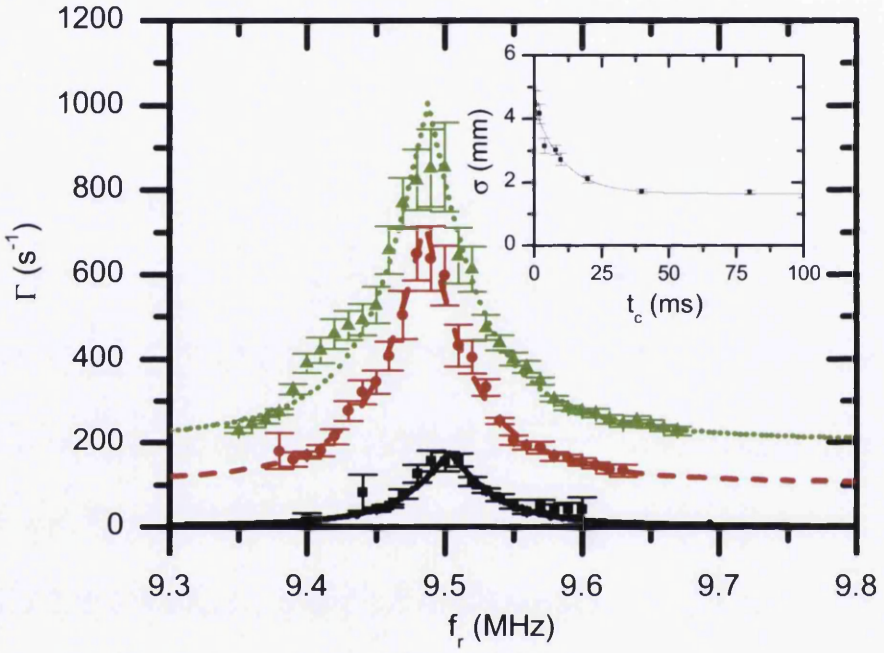

Figure 2.12: Compression rate as a function of the RW frequency for amplitudes of 75 mV (■), 150 mV (•), offset by 100 s^{-1} and 225 mV (▲), offset by 200 s^{-1}. The line is fitted using equation 2.21 [Eq. 5 in reference]. Inset: Ejected cloud radius versus the RW on-time. The uncertainties on the points in both graphs are due to scatter on repeated measurements. [Isaac *et al.*, 2011, Fig. 2, p. 3]

Cooling

Cooling is a requirement common to all (non destructive) applications of the RW technique, being necessary to counteract the heating that the rotating field induces through resonant interaction with the particle motion. For electrons/ positrons confined in a high magnetic field, the energy radiated by the rapid cyclotron motion is usually sufficient, with a cooling time given by,

$$\tau_c = \frac{3\pi\epsilon_0 m_e^3 c^3}{e^4 B^2} . \tag{2.22}$$

However, in fields below 100 mT this is very slow ($\tau_c \gtrsim 260$ s) and an additional cooling mechanism is needed, such as inelastic collisions with a suitable gas [Bertsche and Fajans, 2003].

As N_2 is already employed as a buffer gas in positron accumulators, it would seem a natural choice to combat RW heating. However, whilst electronic excitation of N_2 results in significant energy loss, cooler positrons cannot access this channel and thus the prevalent inelastic interaction defaults to excitation of its vibrational states, the cross section for which is comparatively small. Fortunately there exist a number of alternative gases with more efficient cooling potential, e.g. sulphur hexafluoride - see table 2.6.

Table 2.6: Parameters for cooling gases at 2.7×10^{-8} mbar: annihilation time, τ_a, measured cooling time, τ_c, and vibrational quanta, E_v. [adapted from Greaves and Surko, 2001, Tbl. 1, p. 1881].

Molecule	Formula	τ_a [s]	τ_c [s]	E_v [eV]
Sulphur hexafluoride	SF_6	2190	0.36	0.076, 0.188
Carbon tetrafluoride	CF_4	3500	1.2	0.157
Carbon dioxide	CO_2	3500	1.3	0.291, 0.083
Carbon monoxide	CO	2400	2.1	0.266
Nitrogen	N_2	6300	115	0.292

2.4.3 Implementation

The RW field is deployed using an electrode from the second stage of the accumulator, that has been axially bisected and one half of which has been azimuthally segmented into quadrature - figure 2.13.

The required sinusoidal voltages are generated with a *NF Corporation* Wavefactory multifunction synthesizer (WF1946B), with a 16-bit ± 10 V waveform output capable of frequencies from 0.01 μHz to 15 MHz. Generally the output is gated using an external trigger connected to a digital output of the FPGA. Control of the device configuration is facilitated by GPIB communication and Labview™ software. Two channels of the Wavefactory are phase locked with a relative difference of $\pi/2$, and each output is split through an inverting device. The four signals are then superposed onto the usual electrode bias voltage (E6) using a high pass filter, and connected to the appropriate electrode segments via BNC feedthroughs on cross II.

Collisional cooling of RW compressed particles is achieved by admitting a low pressure gas into cross II - section 2.1.1. For positron work SF_6 is typically used, however this gas has a particularly high affinity for electron capture [Gerchikov and Gribakin, 2008], therefore when RW compressing electrons CO_2 is used instead.

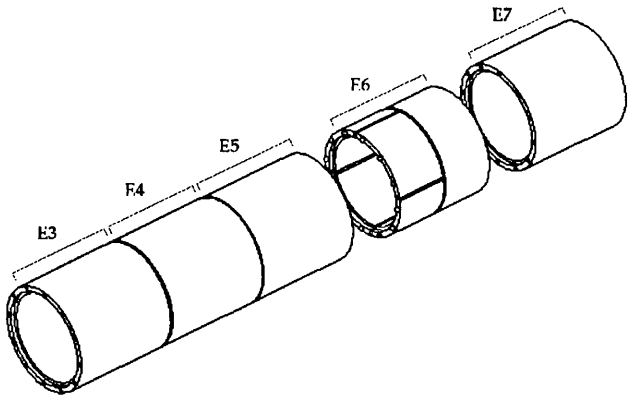

Figure 2.13: Exploded view schematic of the second stage of the accumulator, indicating the segmented electrode used for RW compression. The labels represent bias supplies - see section 2.3.2. [adapted from Isaac, 2010, Fig. 2.6. p. 24]

2.5 Positronium Production

2.5.1 Porous Silica

Positrons implanted into a mesostructured porous silica film can experience a variety of interactions with the bulk material (e.g. figure 2.14), typically losing energy via collisions and phonon scattering [Schultz and Lynn, 1988], and eventually succumbing to direct annihilation with electrons or binding with such to form positronium - equation 1.5. The Ps atoms can diffuse to and be captured by the pervasive pore structure, wherein they may survive for some significant fraction of their vacuum lifetime, circumscribed by the dimensions of the pores (see below). Assuming that these are interconnected and extend to the sample surface, the positronium may arrive at the latter and be emitted to vacuum as free Ps.

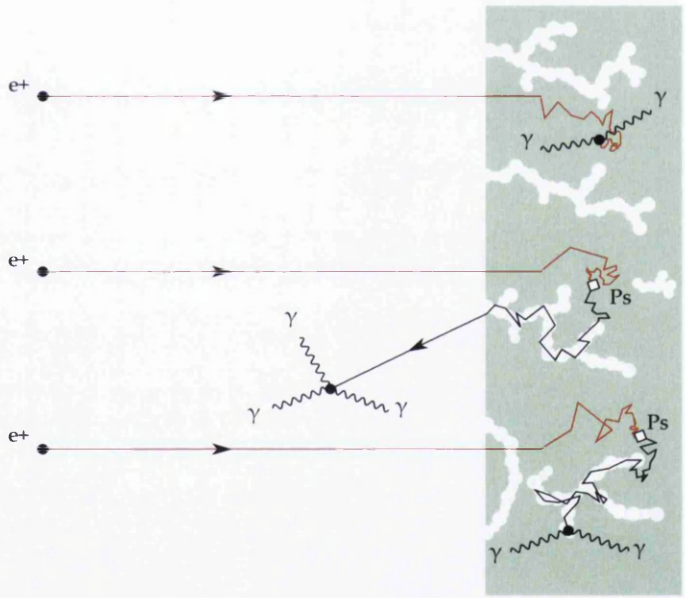

Figure 2.14: Schematic illustrating examples of positron interactions with porous silica, including: direct annihilation (top); Ps formation and emission to vacuum (middle); Ps formation and annihilation within a pore (bottom).

Positronium captured by the porous cavities will likely undergo inelastic scattering [Nagashima *et al.*, 1998] from the inner pore structure, losing energy and - assuming the implantation depth is sufficient ($\gtrsim 300$ nm) - arriving at the surface (predominately o-Ps) with approximately thermal energies. This is observed if the positrons are implanted with kinetic energy in excess of ~ 2 keV [Crivelli *et al.*, 2010; Yu *et al.*, 2003]; although naturally the increased time within the material [Cassidy *et al.*, 2010a], and further the risk during collisions of pick-off annihilation or spin exchange, decreases the Ps fraction which does survive to the surface.

When the pore structure is very small ($\lesssim 10$ nm), its interaction with positronium will exhibit quantum phenomena, particularly as the Ps cools. The shift from a classical to quantum regime complicates modelling the behaviour accurately, however the energy to which the Ps possibly *can* cool is easily approximated in analogy with suchlike in a quantum well of dimensions similar to the pore size. Explicitly, a Ps atom confined within a spherical pore of diameter $\varnothing = 2r_0$ has ground-state energy given by,

$$E_0 = \frac{\pi^2 \hbar^2}{4 m_e r_0^2} \, ; \tag{2.23}$$

e.g. for $\varnothing = 5.5$ nm this yields $E_0 \approx 25$ meV. A rough estimate of the o-Ps annihilation rate in the pore can be made by determining the fraction of the wave-function which falls inside an electron layer in the region of the pore surface, defined as $r_1 < r < r_0$ (where $r_0 - r_1 \approx 0.16$ nm), within which a spin averaged lifetime of 0.5 ns is assumed [Eldrup *et al.*, 1981; Kobayashi *et al.*, 1989; Tao, 1972]:

$$\Gamma = 2[\mathrm{ns}^{-1}](1 - \frac{r_1}{r_0} + 0.159 \sin(2\pi r_1 / r_0)) \, . \tag{2.24}$$

Advanced theoretical treatments provide a more complete picture of the Ps interaction with the pore structure [Dull *et al.*, 2001; Gidley *et al.*, 1999; Kobayashi *et al.*, 2007]. These allow Ps to be used as a powerful material probe when employed in conjunction with diagnostics, such as: positron annihilation γ-ray spectroscopy (PAS); positron annihilation lifetime spectroscopy (PALS); time of flight measurements (TOF); angular correlation of annihilation radiation (ACAR).

2.5.2 Implementation

Positrons from the accumulator are implanted into a mesostructured porous silica film, kindly provided by Liszkay *et al.* [2008a]. These 400 mm^2 films are grown using Pluronic® F-127 ethyleneoxide/propyleneoxide block copolymer (BASF), with 0.016 F-127/Si molar ratio. The films are deposited 700 nm thick onto silicon by spin coating at 2000 rpm, after which the porogen is removed by heating to 400 °C in air. At Swansea the sample was again slowly heated to 400 °C in air, to remove containments (e.g. water) prior to installation in vacuum. The total conversion efficiency for incident positrons to free positronium is expected to be in the region of 30 %.

The silica substrate is mounted onto an electrode assembly (figure 2.15) that includes target, grid and ring electrodes. The ring electrode is employed in alignment of the positron beam, and the region between the grid and target is used for laser interaction with Ps - see chapter 5. A clamp on the rear of the target holds a neodymium permanent magnet ($\varnothing$ = 20 mm, L = 20 mm), which produces a field of roughly 100 mT at the converter. The assembly is attached to a vertical manipulator in cross IV, and in-vacuum Kapton® insulated wiring connects the target, grid and electrode to SHV feed-throughs for HV biasing.

2.6 Detection and Diagnostics

2.6.1 MCP and Imaging Assembly

A microchannel plate detector (MCP) [Wiza, 1979] and phosphor screen assembly is located in cross III - this is primarily employed for analysis of the areal distribution of the accumulated positron clouds.

An MCP plate consists of several million hollow microchannels (typically leaded glass, $\varnothing \sim 10$ μm) arranged in a tightly packed array ($a \sim 12$ μm). An energetic charged particle striking the interior surface of a channel liberates a number of sec-

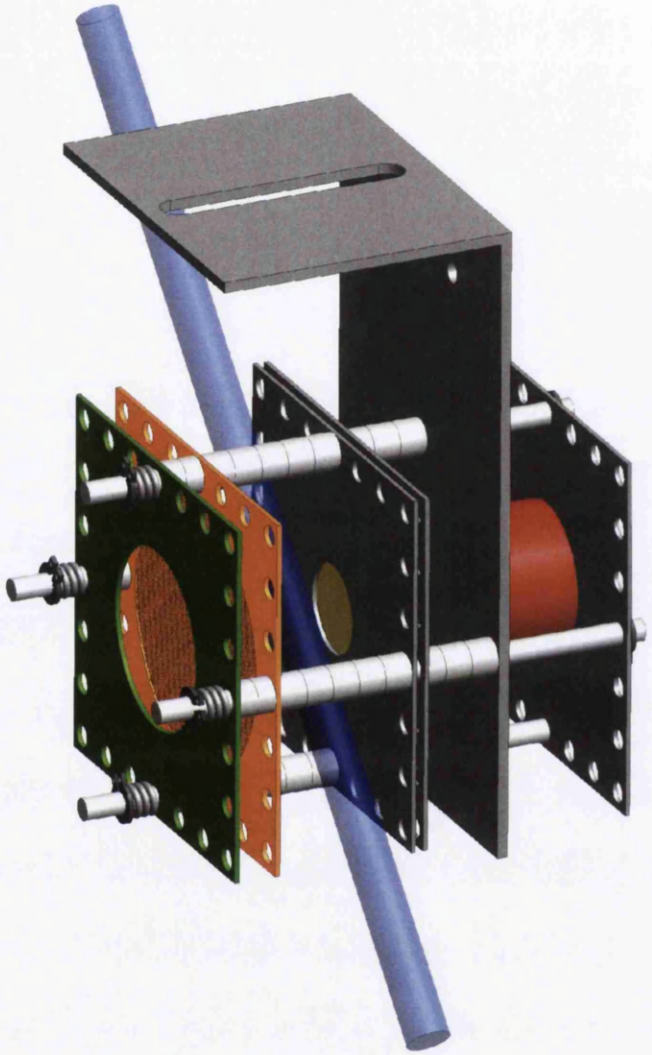

Figure 2.15: False colour, scale drawing of the Ps converter assembly, including: alignment electrode (green); grid (orange); porous silica target (yellow); permanent magnet (red). Assembled with *Kimball Physics* eV Parts®. The path of the UV laser - see chapter 3 - is also illustrated (blue).

ondary electrons, which will experience subsequent impact within the channel and likewise produce more secondary electrons. Numerous iterations of this process culminates in extremely high current amplification, whilst the channel structure helps to retain some spatial information of the source particle distribution. The front and back of the plate is coated with a conducting material, so that a high electric field may be applied along the channels; this is necessary to obtain sufficiently high electron impact energies to sustain amplification.

The MCP assembly was provided by *Lambert Instruments* and consists of two MCP plates with an active area 40 mm in diameter, stacked upon a phosphor screen of similar dimensions - figure 2.16. Positrons impinging on the plates produce an amplified electron current which strikes the phosphor screen, exciting electron-hole pairs that de-excite through emission of photons. The phosphorescent material is P43 (GdO_2S:Tb), which emits visible light peaked at a wavelength of 545 nm (green). The decay time of the phosphor glow is $\sim$ 650 µs.

Figure 2.16: Photograph of the MCP and phosphor screen assembly.

The MCP assembly is attached to a support jig (figure 2.17) which securely mounts it to a vertical manipulator, adjusted to correctly position the assembly in the centre of the beamline. The jig contains electrical breakouts to the high voltage connectors for both the MCP and phosphor screen, and further includes a fine mesh grid mounted in-front of the MCP, to shield incoming particles from the electric

fields of the HV connectors. A mirror mounted at 45° behind the screen, reflects the phosphorescent image through a window (DN160 CF flange mount) and out of the vacuum system, where it is captured by a *Hamamatsu* Orca-R2, 1.3 megapixel CCD camera, then processed and recorded with Labview™ (see section A.2.3).

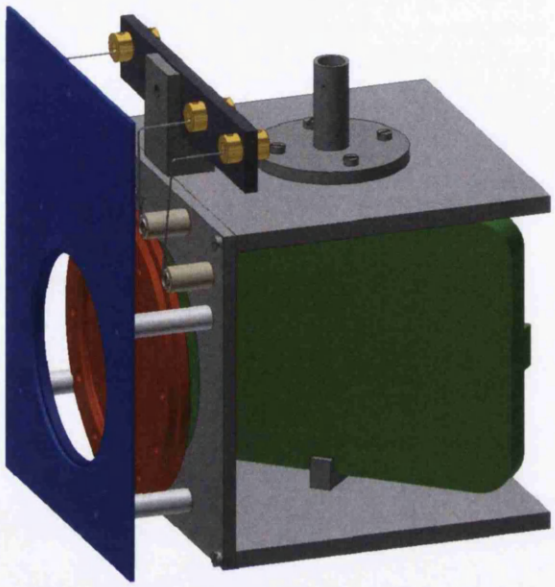

Figure 2.17: A false-colour, scale drawing of the MCP assembly jig, including: grid mount (blue); MCP assembly (red); manipulator mount; HV connectors (gold); mirror (green). The drawing was created from an *Autodesk* Inventor™ design, courtesy of Tim Mortensen.

For positron work, typically the front of the MCP is biased at −1.4 kV using an *Ortec* 659 HV power supply, whilst the back is grounded to the system. This provides amplification of approximately $\times 10^6$, however the front bias is often altered in accordance with the brightness of the accumulated beam, to avoid saturating the camera. The phosphor screen is usually biased at 3 kV using an *Ortec* 660 HV power supply; this shuts down in response to a MaxiGauge™ relay, triggered if the reading on PG-9 exceeds 5×10^{-5} mbar. In principal the phosphor screen can be used as an anode to measure the amplified electron current, however this facility has not been employed in these studies.

Retarding Potential Analyser

By application of a retarding potential bias to the grid (see figure 2.17), only those positrons with energies $E_{\|} > U_{grid}$ can pass and be detected (Q). A series of accumulation measurements where the bias is scanned through some suitable range (e.g. figure 2.18), will hence reveal the integrated parallel energy distribution of the accumulated cloud [Eggleston *et al.*, 1992]. It is typically found that such data is fitted well by the complementary error-function,

$$Q(E) = \frac{N}{\sigma\sqrt{2\pi}} \int_E^{\infty} exp\left(\frac{-(E' - E_0)^2}{2\sigma^2}\right) \mathrm{d}E' , \tag{2.25}$$

from which both the mean parallel energy $E_0 = \frac{1}{2}m\left\langle \vec{v}_z^{\,2} \right\rangle$ and FWHM energy spread $\Delta E = 2\sqrt{2\log 2}\,\sigma$ of the cloud can easily be deduced.

Note that E_0 as measured in figure 2.18 is significantly higher than the base of the potential well of the accumulator ($\sim$ 30 eV). This largely results as the positron transport is adiabatic, and the decreasing magnetic field allows for perpendicular cyclotron energy in the accumulator to be transferred into parallel energy at the MCP in cross III.

2.6.2 Scintillation Detectors

Scintillating materials undergo luminescence when exposed to ionising radiation. This property makes such instrumental in the detection of positron-electron annihilations, effectively converting the resulting gamma rays into frequencies better suited to detection via e.g. diode detectors or PMTs.

There exist a great variety of known scintillating materials, each exhibiting a unique luminescent response to radiation. These include organic compounds (such as various plastics) for which molecular states are excited to subsequently fluoresce with typically fast timing characteristics. Conversely, inorganic scintillating crystals often exhibit slower fluorescence from 'forbidden' states in the crystal's band

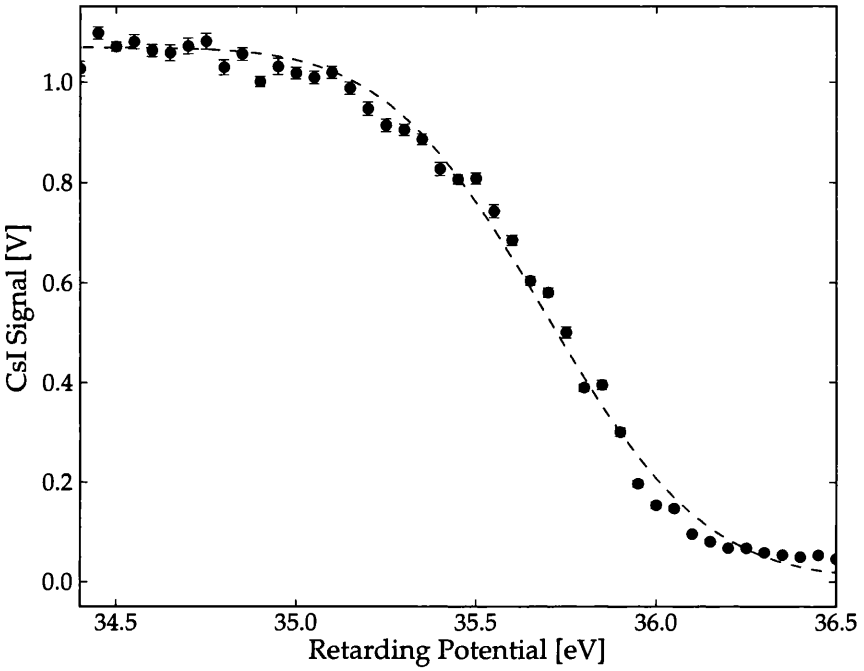

Figure 2.18: Example energy spectrum curve for the simple trapping scheme described in table 2.4. The green dashed line represents a fit of equation 2.25 to the data, yielding a mean energy $E_0 = 35.7$ eV and FWHM $\Delta E = 0.8$ eV. The error-bars indicate the the statistical uncertainty derived from repeat measurements.

gap, but are well suited to gamma ray detection due to the relatively high density - thus high gamma ray absorption - common to such compounds.

Characteristics of interest with regard to scintillating materials include: luminosity (LO); peak emission wavelength (λ_{peak}); density (n); linearity; energy resolution; rise time; decay components; primary decay time (τ_D); resilience to radiation; mechanical stability; production cost. As no one material is superior in every aspect, the specifics of any given application will determine which features need be prioritised. A number of materials favoured in positron and positronium studies are outlined in table 2.7.

Table 2.7: Properties of a selection of inorganic scintillators [Derenzo *et al.*, 2013].

Formula	n[g/cm^3]	LO[γ /keV]	λ_{peak}[nm]	τ_D[ns]
NaI:Tl	3.67	44	415	250
CsI:Tl	4.51	56	530	980
CsI:Na	4.51	41	425	630
$PbWO_4$	8.28	0.2	420	6

CsI Diode Detector

Caesium Iodide (CsI) crystals are utilised in detection of annihilation gamma rays to infer positron numbers following accumulation, or in counting to estimate moderator efficiency. These crystals have a large light output and an emission spectrum well suited to coupling with silicon photodiodes. The slow timing properties of the crystal renders them unsuitable for fast (< 10 µs) applications. On the beamline we regularly employ two CsI/diode assemblies, at varied locations.

In conjunction with the retractable plate in cross II, these detectors may be utilised to characterise the spatial distribution of the beam. A series of measurements of the annihilation signal as the plate is incrementally moved through the beam path, can be used to infer it's location and width. Alternatively, an estimate of the cloud width can be achieved in a single shot by use of a hole drilled in the centre

of the plate, from the measured ratio of the annihilation signal at the plate to that which passes through (assuming a Gaussian beam profile and its alignment with the hole). Such was utilised in previous investigations of the RW technique [Isaac, 2010; Isaac *et al.*, 2011]. Since installation of the MCP, these methods are generally only used to assist in beam alignment.

Lead Tungstate and PMT assembly

For applications where fast timing detection of gamma rays is necessary (such as SSPALS - see section 5.1) a lead tungstate ($PbWO_4$) crystal is used ($\varnothing = 50$ mm, $L = 40$ mm). This material was selected for its high density and fast decay time; the low light-output is mitigated by amplification of the signal with a PMT (see below). The crystal was purchased from *Shanghai Institute of Ceramics, Chinese Academy of Sciences* in February 2013.

The luminescence from the crystal must be converted into an electronic signal for measurement with an oscilloscope. This is achieved with a *Hamamatsu* R2083 (H2431-51 assembly) photomultiplier tube (PMT). Incident light enters the tube through a window and impinges on a photo-cathode, exciting photoelectric electrons. These are accelerated and focused in vacuum onto the first dynode, and there generate secondary electrons. A series of dynodes further amplifies the signal, which ultimately arrives at the anode where the current is measured.

For placement of the crystal very near to the Ps formation region, a so-called "top hat" flange is employed, which features a cylindrical hollow that extends from the exterior face of the flange into the vacuum system (figure 3.7). This facilitates positioning of the crystal with roughly 14 % solid angle coverage of gamma-ray photons originating from the centre of the cross. However, as photomultiplier tubes are sensitive to magnetic fields it is necessary to distance the PMT from the beamline. This is achieved by coupling the PMT to the PWO via a plastic light guide ($\varnothing = 50$ mm, $L = 0.6$ m), shielded from background light in an aluminium tube and held securely in a clamp assembly. The detector assembly is shown in situ for SSPALS measurements in figure 2.19.

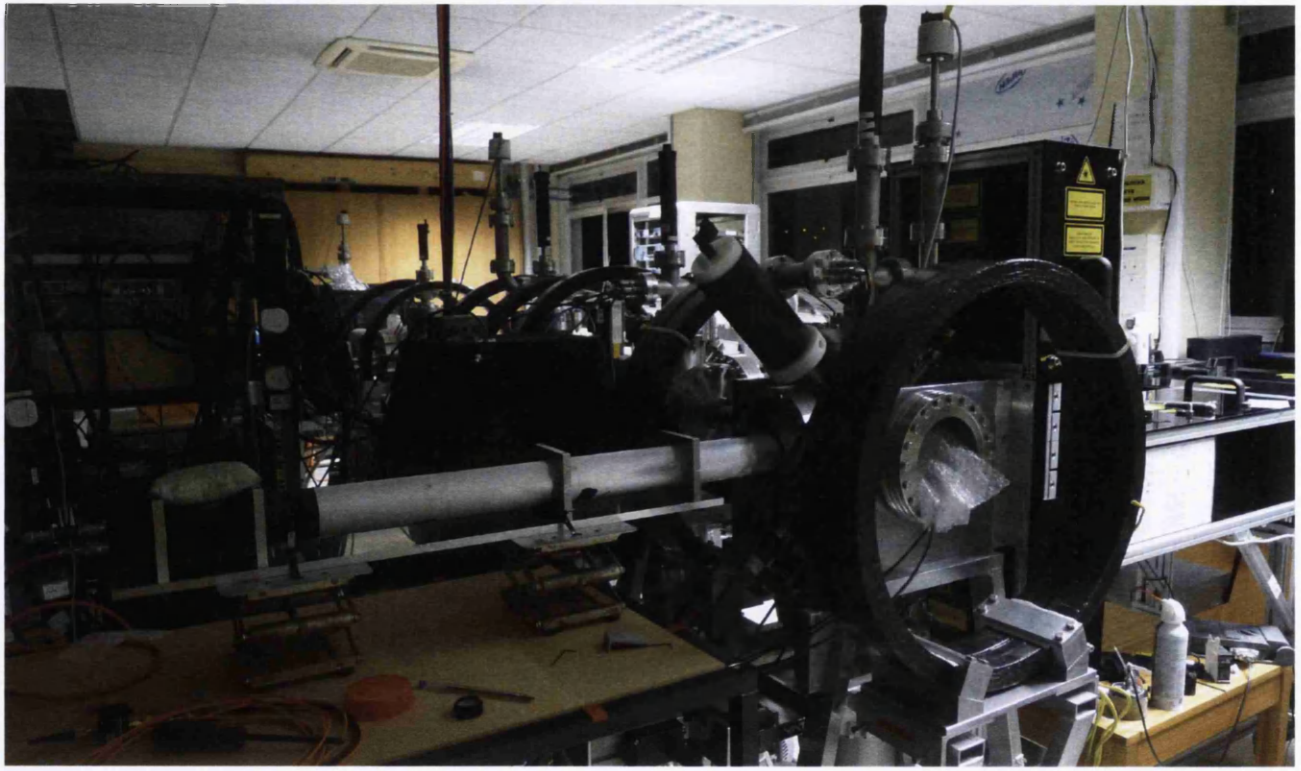

Figure 2.19: Photograph of the PWO/PMT assembly, in position for gamma detection in cross IV.

Chapter 3

Ultraviolet Pulsed Laser

3.1 System Design

There are a number of challenges to be met in designing a laser for excitation of the Lyman-α interval ($1^3S - 2^3P$) of positronium. The vacuum wavelength required for such is 243.0 nm [Canter *et al.*, 1975] - this being ultraviolet is already a little tricky! Furthermore, in order to investigate spectroscopic features across the Doppler broadened interval (see section 1.3.2) any laser for pumping the transition should ideally be tunable over a ~ 1 nm range. Additionally, the anticipated broadening (THz) and the desire for efficient excitation, is incompatible with the narrow linewidths (MHz) of most laser technologies.

Other experiments have addressed the issue of bandwidth by use of a dye laser [Cassidy *et al.*, 2010a; Ziock *et al.*, 1990b], as these have an inherently broad gain-profile, are tunable, and further can be adapted for linewidths in excess of 100 GHz. Although dyes for 243 nm are not available, the range of frequencies over which these lasers can be tuned opens several avenues for achieving the correct wavelength through harmonic, or sum-frequency generation with nonlinear optics (see section 3.3). Pulsed operation of such lasers can achieve high power-densities, maximising the likelihood of exciting the transition during the pulse.

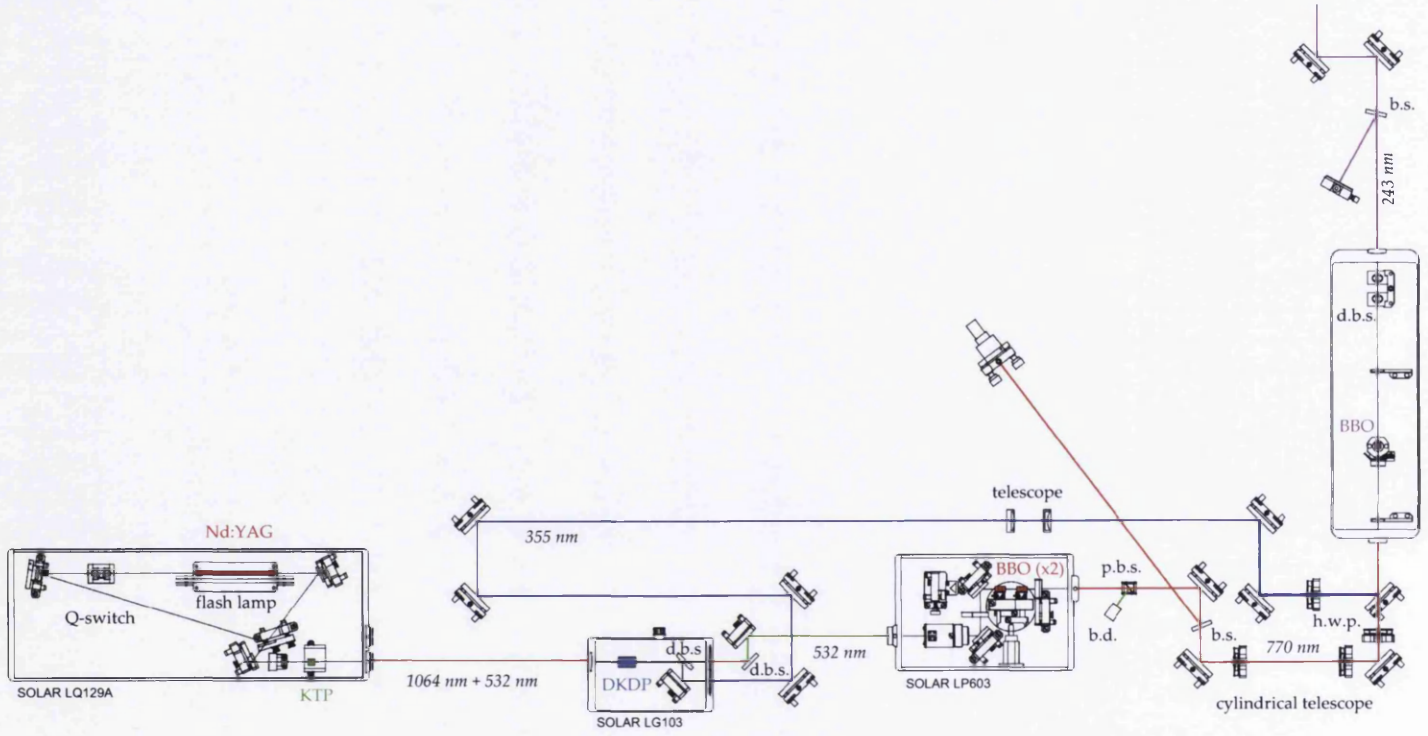

Figure 3.1: Schematic (approx. to scale) of the Swansea UV laser design. The main laser units have been labelled (see text), and the beam paths are colour coded and labelled by wavelength (italics). Additional labels refer to optical components, including: beam dumps (b.d.), beam samplers (b.s.), dichroic beam separators (d.b.s.), half-wave plates (h.w.p.), polarising beam splitters (p.b.s.), Nd:YAG rod and various NLO crystals (coloured in accord with output beam path) - see text.

Previous work at Swansea produced a pulsed 243 nm laser using the third harmonic of a solid state titanium sapphire (Ti:Al_2O_3) laser [Griffiths, 2005; Kerrigan, 2011; Watkeys, 2008]. The null result for Ps excitation events with this beam was attributed to insufficient bandwidth[1] and power to achieve sufficiently many excitation events to surpass their detection threshold.

An alternative scheme based on preliminary work by Kerrigan [2011] has been developed in these studies, which utilises a succession of nonlinear processes to generate a high power, broadband UV pulse. This is achieved by doubling and tripling the 1064 nm fundamental wave of a Nd:YAG laser, to 532 nm and 355 nm respectively. The second harmonic is used to pump an optical parametric oscillator (OPO), which generates a broadband signal-wave that is tuned to 770 nm. This is mixed with the third harmonic in a sum frequency generator (SFG), producing the required Ps Lyman-α wavelength of 243 nm. Both the tunability and broadband criteria outlined above, are fulfilled by use of the OPO. This laser design is depicted schematically in figure 3.1.

A great advantage of this wholly solid-state design is its robustness and consequently minimal need of maintenance, particularly in comparison to the dye lasers employed in the cited works.

3.2 Nd:YAG

The UV laser is derived from a Nd:YAG laser [Geusic *et al.*, 1964]. The active element of such is a solid-state crystal of yttrium aluminium garnate ($Y_3Al_5O_{12}$) doped with neodymium ($Nd^{3+} \sim 1$ %), which lases via a four level process at a wavelength of 1064 nm (figure 3.2). In pulsed operation these lasers are well suited to use with a Q-switch: a device which temporarily blocks the cavity to maximise population inversion in the active element, and thereby increase the peak power density of the output pulse.

[1] Although titanium sapphire has a very broad gain bandwidth ($\Delta\nu \approx 100$ THz), the output bandwidth of the laser was limited by various optical components to approximately 30 GHz.

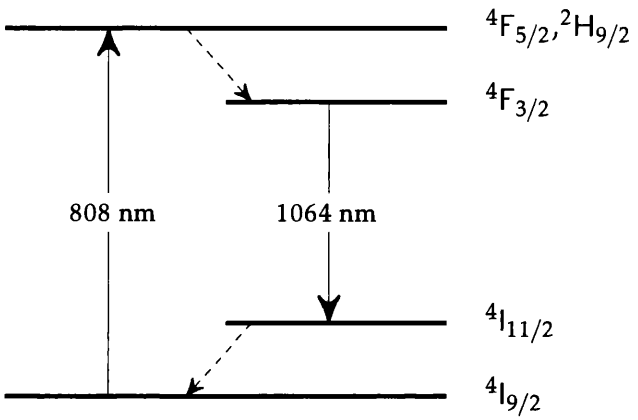

Figure 3.2: The dominant absorption (blue) and emission (red) transitions of the trivalent neodymium ion that are utilised by Nd:YAG lasers. The dashed arrows indicate the fast, radiationless decay between the laser and pump energy states. *N.B.* flash-lamp pumped lasers will excite a broad range of pump transitions.

Specifically, we employ a *SOLAR* LQ129A, which is powered, water cooled and controlled with a *SOLAR* LPS-1500 power supply. The former is a ring cavity Nd:YAG laser, which is optically pumped with a xenon flash lamp. Such lamps emit light well matched to the absorption spectrum of the active rod. The cavity further contains a Pockels-cell device, allowing for Q-switched operation. When running at 10 Hz this laser yields up to 500 mJ at 1064 nm in a 15 ns (FWHM) pulse, with a beam diameter of roughly 8 mm. The LPS-1500 can optionally be configured for remote triggering of the flash lamp and/ or Q-switch.

3.3 Nonlinear Frequency Conversion

The few wavelengths attainable with early laser technologies, fuelled interest in materials able to convert such frequencies into those of the otherwise inaccessible regions of the electromagnetic spectrum [Franken *et al.*, 1961]. The field of nonlinear optics (NLO) that arose maintains vigorous interest to this day, whilst the flexibility of nonlinear materials in deriving novel wavelengths at significant power

density, accounts for their extensive employment in a myriad of applications.

A brief outline of the nonlinear process of *three wave mixing* is given in the remainder of this section, and applications of such in the Swansea UV laser are discussed in the sections which follow. I refer the interested reader to Silfast [1996, chap. 16] and Telle *et al.* [2007, chap. 4], for further information regarding NLO.

NLO and Three Wave Mixing

When light propagates within a medium, the electric field component of the wave will interact with and distort the dipole moments formed by the electron clouds and their atomic nuclei, thereby inducing a macroscopic polarisation,

$$\vec{P} = \chi \epsilon_0 \vec{E} \,. \tag{3.1}$$

In certain materials the susceptibility, χ, to the electric field includes significant nonlinear components, such that the polarisation strength, P, may be expanded as a power series of the electric field strength, E, explicitly:

$$P = \epsilon_0 (\chi_1 E + \chi_2 E^2 + \chi_3 E^3 + \ldots) \,. \tag{3.2}$$

If we consider two superposed and coincident electromagnetic waves of frequencies ω_1 and ω_2, the total electric field strength may be represented as,

$$E(t) = E_1 e^{-i\omega_1 t} + E_1^* e^{i\omega_1 t} + E_2 e^{-i\omega_2 t} + E_2^* e^{i\omega_2 t} \,. \tag{3.3}$$

Therefore the second order term of the polarisation of a nonlinear medium subjected to such a field is given by,

$$\begin{aligned} P_2(t) &= \epsilon_0 \chi_2 E^2 \\ &= \epsilon_0 \chi_2 \Big[E_1^2 e^{-i(2\omega_1)t} + E_2^2 e^{-i(2\omega_2)t} + 2E_1 E_2 e^{-i(\omega_1+\omega_2)t} \\ &\qquad + 2E_1 E_2^* e^{-i(\omega_1-\omega_2)t} + E_1 E_1^* + E_2 E_2^* + \text{c.c.} \Big] \,. \end{aligned} \tag{3.4}$$

In physical terms, equation 3.4 implies that the intense electric field of two overlapping laser beams may cause charges in a medium with a non-zero second order susceptibility, to oscillate and thus radiate light, at the sum or difference of the frequencies of the input beams - the second harmonic being a special case of the former. From a quantum perspective the harmonic and sum cases may be interpreted as, two photons (ω_1, ω_2) being absorbed and a third (ω_3), equal to the sum of their energy, being emitted ($\omega_1 + \omega_2 \Rightarrow \omega_3$), thus satisfying energy conservation. Such second order NLO processes are classified as *three wave mixing*.

In truth, the above is an over-simplification as it disregards the vector properties of light. Taking these into consideration introduces the condition of *phase matching*, whereby the wave-vectors ($|\vec{k}| = 2\pi/\lambda$) of the input and output beams must balance, i.e. conserving momentum,

$$\vec{k}_1 + \vec{k}_2 = \vec{k}_3 \,. \tag{3.5}$$

Perhaps more intuitively, this restriction demands that: to generate an intense ω_3 field, the microscopic oscillations throughout the NLO medium must contribute to it in phase. In practice this is achieved by exploiting the birefringence of nonlinear materials, meaning the refractive index is anisotropic and thus dependent on the orientation of the light (i.e. the polarisation) with respect to the optical axis of the crystal. Angular tuning of the crystal relative to the propagation of the two pump beams (e.g. see figure 3.3) can therefore be tuned to satisfy equation 3.5. The nature of the birefringence determines whether this is achieved when the pump beams have either parallel or orthogonal polarisations, such crystals being categorized as type I or type II, respectively. Alternatively, the refractive index can be tuned to achieve phase matching by adjusting the temperature of a crystal.

A great variety of crystalline materials have been tailored for nonlinear production of light. Important properties include, non-linearity, transparency (for all relevant wavelengths), resilience to optical and chemical damage, homogeneity, size and cost. NLO materials employed in these studies include potassium titanyl phosphate (KTP, $KTiOPO_4$), deuterated potassium dihydrogen phosphate (DKDP, KD_2PO_4), and β-barium borate (BBO, β-BaB_2O_4).

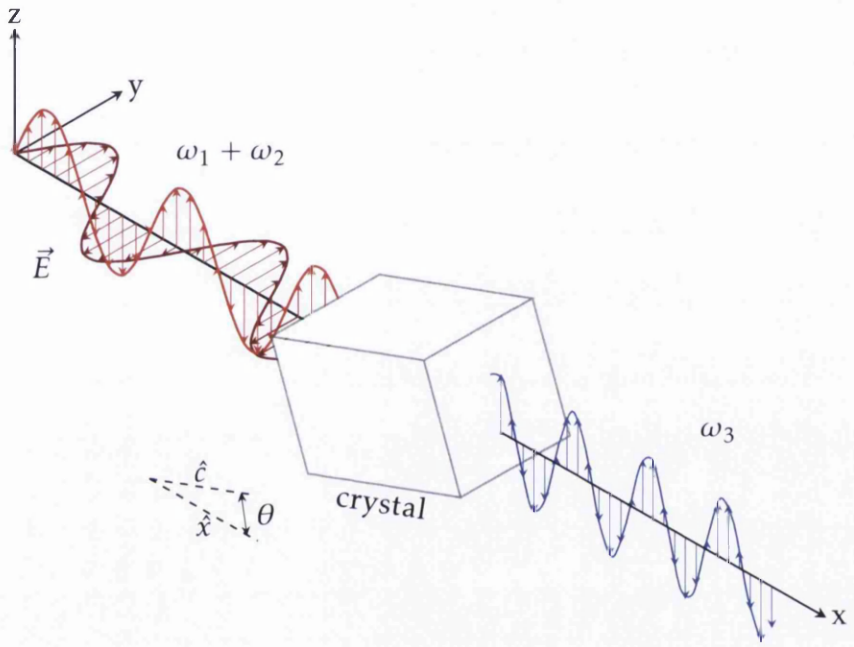

Figure 3.3: Schematic illustration of the electric field component for three wave mixing in a type II nonlinear crystal. Phase matching is achieved by tuning the angle (θ) of the optical axis of the crystal relative to the path of the input beams.

3.3.1 Harmonic Generation

A significant fraction of the intense pulse of IR radiation obtained with the LQ129A can be converted to its second harmonic (532 nm), by means of a temperature stabilised KTP nonlinear crystal, located within the the laser head unit - see figure 3.1. Optimal angular phase-matching of the crystal facilitates generation of up to 220 mJ of the 2ω wave (in Q-switched operation).

Ordinarily the 1ω and 2ω beams would be split within the LQ129A using a dichroic beam separator (d.b.s, i.e. a specially coated mirror designed to transmit/ reflect certain wavelengths of light), however this was removed in order that the beams exit the unit co-linearly. The laser light then enters a *SOLAR* LG103 (prototype) SFG, containing a temperature stabilised DKDP nonlinear crystal. Angular phase-matching to obtain the sum frequency of the two input beams yields up to 60 mJ of the third harmonic (355 nm). Within this unit a dichroic mirror separates the 3ω from the pump beams, and externally the residual 1ω and 2ω light is separated using a further dichroic mirror.

The 3ω beam is then steered to a Galilean telescope ($\times 2$ magnification) that compresses the diameter to $\sim$ 4 mm, following which it is directed to a second SFG device - section 3.3.3. The 2ω wave meanwhile is aligned to pump the OPO - section 3.3.2.

3.3.2 Optical Parametric Oscillation

As discussed in the introduction to this chapter, the key to the tunability and broadband features of the UV laser design is a free-running optical parametric oscillator (OPO) [Giordmaine and Miller, 1965].

An OPO is a second order nonlinear device which uses three wave mixing to obtain a tunable beam in a manner analogous to time reversed SFG, i.e $\omega_3 \Rightarrow \omega_1 + \omega_2$; conventionally each frequency (1-3) is referred to as the signal, idler and pump wave, respectively. In the case here, the pump wave (Nd:YAG 2ω, 532 nm), is focussed through a pair of BBO nonlinear crystals which are located in a 110 mm cav-

ity of the *SOLAR* LP603. The cavity is resonant with the desired signal wave, which - provided the pump exceeds threshold power density (in our case ~ 50 MW cm^{-2}) - is parametrically amplified within the crystals from background quantum fluctuations, concomitantly exciting an idler wave, both of which exit the unit via a partially transmitting cavity mirror. As two photons are generated for every one absorbed, there is an infinite continuum of coupled solutions to ω_{signal} and ω_{idler} that satisfy energy conservation. The wavelengths which are produced are thus selected by the phase matching condition (equation 3.5) which is adjusted for the desired frequency by rotation of the crystals.

Two BBO crystals (14 mm × 10 mm × 7 mm) are used in the OPO which have been cut such that phase selection is maintained by opposite rotation of each with respect to the other. This automatically corrects any beam walk (displacement of the beam path in passing through the medium) due to the altered crystal orientation, and thereby preserves alignment of the cavity and position of the output beams. The crystal rotation is controlled by a *Thorlabs* T-Cube DC servo motor controller, facilitating software control. The range of attainable signal wavelengths is illustrated in figure 3.4.

Exploiting the fact that the linearly polarised signal wave is orthogonal to both the pump and idler, the signal is isolated from the output using a polarising beam splitter. The elliptical beam profile and horizontal divergence of this beam is corrected for by use of a cylindrical telescope, afterwhich the signal wave is diverted into the SFG unit (section 3.3.3). When selected for 770 nm, the OPO output yields around 25 mJ per pulse, the length of which (10 ns, FWHM) is slightly less than the pump (15 ns) due to requirement to surpass threshold power density.

3.3.3 Sum Frequency Generation

To obtain the desired 243 nm beam the third harmonic (355 nm) and OPO signal-wave (770 nm) are combined in a sum frequency generator (SFG). A small extension was added to the path of the 3ω beam in order to slightly delay its arrival at

the SFG and thus account for the time required to build up beyond threshold in the OPO; i.e. the path was tuned such that the peak power of the two beams arrive at the SFG simultaneously. The timing of each was verified using a *Thorlabs* SV2-FC Si photodetector, indicating coincidence of better than 1 ns.

The energy in each pulse was selected to be roughly 43 mJ for the third harmonic and 24 mJ for the OPO signal-wave, in order to approximately equate the number of photons for the SFG. The beam energies were varied by (de)tuning the second harmonic phase-matching of the KTP crystal (see figure 3.5), reciprocally altering the efficiency of the third harmonic production and the intensity of the OPO pump.

Two telescopes (previously discussed) are used to approximately match the spatial profiles of the beams, which are overlapped and made to pass through a BBO crystal that is rotated for phase-matching at the sum of their frequencies. This generates a UV beam of $\lambda = 243$ nm in an 8 ns pulse, with between 0.75 mJ and 1.5 mJ of energy. As the wavelength of the OPO is tuned the phase-matching in the SFG must be adjusted to maintain optimum UV generation. A density plot of the UV pulse energy for various positions of the motors used to steer both the OPO and SFG is given in figure 3.6.

The UV pulse is separated from the residuals of its pump using dichroic mirrors, then passing through a quartz beam sampler the reflection is directed into a fibre cable coupled to an *Ocean Optics* HR-4000 spectrometer - see section 3.4.1. The transmitted beam (~ 90 %) is then steered to pass through an uncoated CaF_2 window mounted in a DN16 Conflat flange on cross IV, and passing through the centre of the cross, exits through a similar window on the opposite side - see figure 3.7. The beam was aligned to the centre of each window, following which the target assembly (figure 2.15) was positioned in such a way that the laser beam passed 10 mm in front of and parallel to the silica target.

A mirror is clamped onto the exit window flange in order that the UV beam is reflected back through the system, passing again in-front of the silica target. This double-pass approach increases the likelihood of exciting the atoms - see section 5.4.1 for further discussion.

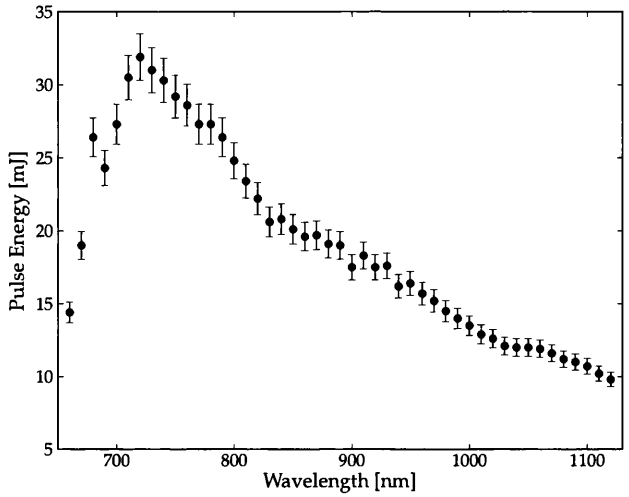

Figure 3.4: The OPO signal-wave wavelength range and output energy, as measured with a *High-Finesse* WS-6D wavemeter and *Coherent* LMP10 10 Hz energy sensor respectively.

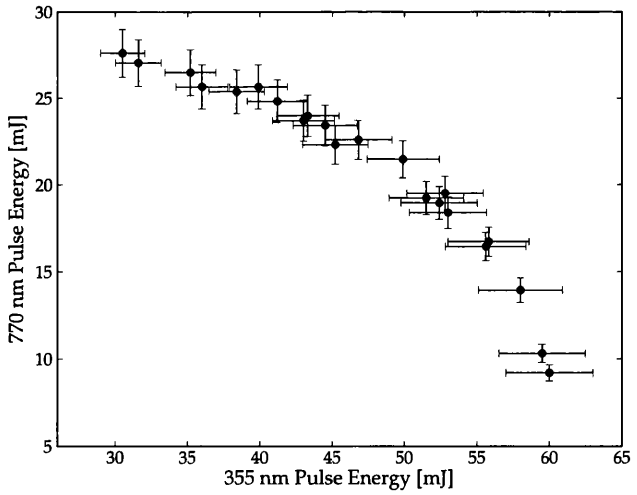

Figure 3.5: The Nd:YAG third harmonic (355 nm) and OPO signal-wave (770 nm) pulse energy for various tunings of the second harmoinc phase-matching.

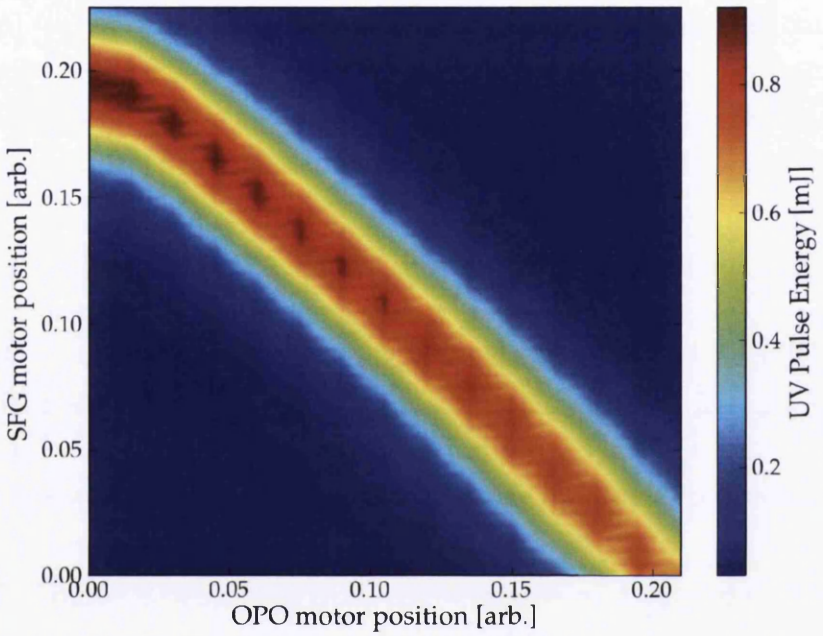

Figure 3.6: The UV pulse energy as measured with a *Sensor und Lasertechnik* PEM-34 for various positions (arbitrary units) of the motors used to control phase-matching for both the OPO and SFG. The range of UV wavelengths to which these parameters correspond is between 242.7 nm and 243.3 nm. The apparent undulating structure along the optimum band is an artefact of interpolation. *N.B.* these measurements were taken with a sub-optimal (aged) Nd:YAG flash-lamp; due to the non-linear nature of the UV beam generation, the $\sim$ 15 % lost at the pump culminated in a 50 % reduction in the UV beam energy from that previously observed.

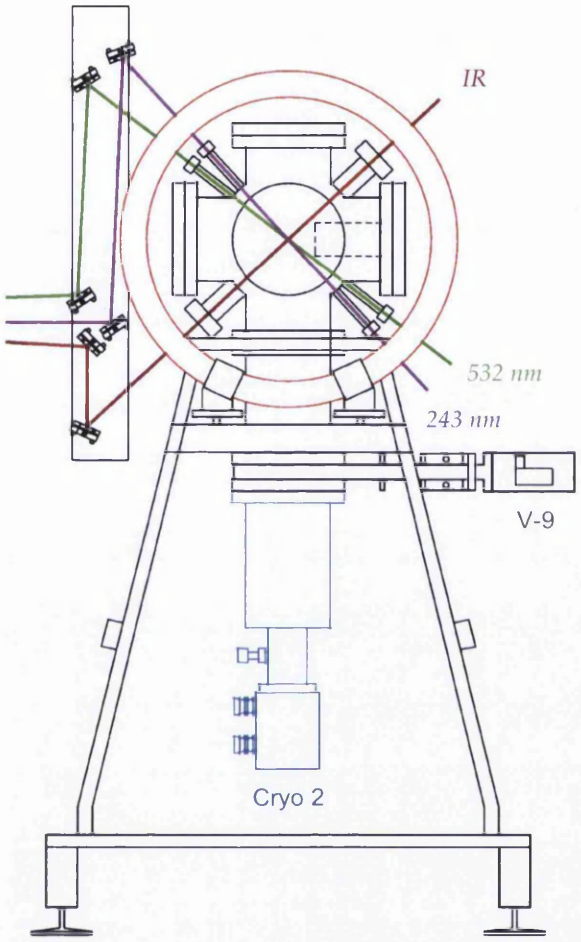

Figure 3.7: Schematic (approx. to scale) of the positron beamline in the region of cross IV as viewed from the direction of the source. The path of the UV 243 nm beam through the cross (left- to right) is shown. Also shown are the paths designated for additional visible (532 nm) and infra red (IR) beams (see chapter 6). The location of the inverted "top-hat" (see section 2.6.2) is illustrated by dashed lines.

3.4 Characterisation

3.4.1 Wavelength

During laser experiments the wavelength of the UV beam is monitored using an *Ocean Optics* HR-4000 high-resolution spectrometer, which collects light reflected from a quartz beam sampler. The HR-4000 employs a diffraction grating and a 3648 pixel (8 μm × 200 μm) linear CCD array to determine wavelengths of light with a resolution of up to 0.02 nm.

The HR-4000 was calibrated by referencing against the emission light of two hollow cathode lamps (HCL). The candent glow of a HCL is interspersed with well defined peaks that correspond to the emission of photons from excited state atoms/ ions, appertaining to the ion type and hence the cathode material (in this case, either palladium or cobalt) - see figure 3.8. Emission spectra were analysed to establish such peaks, by finding the roots of the first differential of an interpolation function of the background subtracted data, filtered to those roots where the data exceeded 4 standard deviations above the mean. These points were then compared to measured emission lines as given in the *National Institute of Standards and Technology* Atomic Spectra Database (ver. 5.0) [Kramida *et al.*, 2013] - see table 3.1. Using those lines in the region of 235 nm to 260 nm that could be confidently identified, a mean correction factor of -0.127 ± 0.005 nm was determined for the spectrometer. All following statements of measured UV wavelengths take this factor into account.

3.4.2 Linewidth

The lineshape of the UV beam is of great interest for Doppler broadened measurement of the $1^3S - 2^3P$ interval of the positronium atom; efficient excitation of such requiring higher than usual laser linewidths ($\gtrsim 80$ GHz). To estimate the widths achieved by the laser design discussed in section 3.1 we employed a *High Finesse* laser spectrum analyser (LSA). This is a highly sensitive grating spectrometer with a resolution of 1 GHz and a 3 THz spectral range from 350 nm to 1120 nm.

(a) Palladium

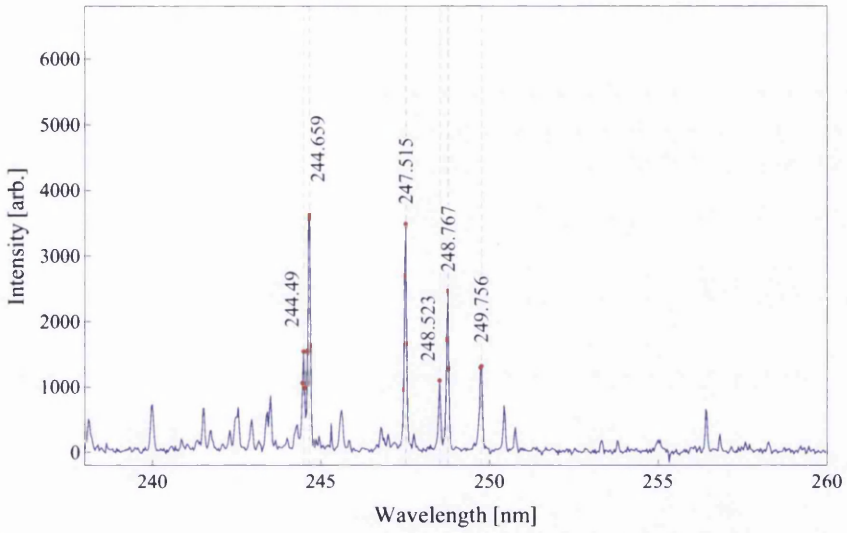

(b) Cobalt

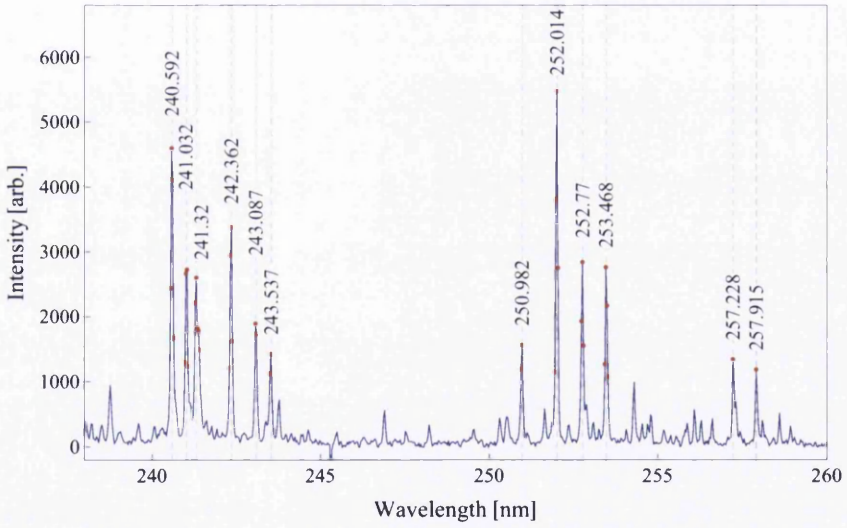

Figure 3.8: Data taken with an *Ocean Optics* HR-4000 spectrometer (15 s acquisition), for the emission of (a) Pa and (b) Co hollow cathode lamps operating at 12 mA. Background subtracted and interpolated data (blue); points exceeding 4 standard deviations above the mean (red); established peaks (see text), labelled and indicated by grey dashed lines.

Table 3.1: Peak wavelengths from HCL spectra as measured with an *Ocean Optics* HR-4000 spectrometer, and the corresponding literature values identified from Ref. Kramida *et al.* [2013]. The quoted wavelengths refer to light measured in air.

Intensity [arb.]	λ [nm]	Ref. λ [nm]	Ion	Lower Level		Upper Level		$\Delta\lambda$ [nm]
3834	244.659	244.790 58	Pd I	$4d^{10}$	$^1S_0$	$4d^9(^2D_{3/2})5p$	$^2\left[\frac{1}{2}\right]^\circ_1$	−0.132
3500	247.515	247.641 27	Pd I	$4d^{10}$	$^1S_0$	$4d^9(^2D_{3/2})5p$	$^2\left[\frac{3}{2}\right]^\circ_1$	−0.126
2464	248.767	248.891 46	Pd II	$4d^8(^3F)5s$	$^4F_{9/2}$	$4d^8(^3F)5p$	$^4D^\circ_{7/2}$	−0.124
1546	244.489	244.618 88	Pd II	$4d^8(^3F)5s$	$^4F_{7/2}$	$4d^8(^3F)5p$	$^4D^\circ_{5/2}$	−0.130
1385	249.756	249.877 69	Pd II	$4d^8(^3F)5s$	$^2F_{7/2}$	$4d^8(^3F)5p$	$^2G^\circ_{9/2}$	−0.122
5479	252.014	252.136	Co I	$3p^63d^74s^2$	a $^4F_{9/2}$	$3p^63d^7(^4F)4s4p(^1P^\circ)$	x $^4D^\circ_{7/2}$	−0.122
4699	240.592	240.725	Co I	$3p^63d^74s^2$	a $^4F_{9/2}$	$3p^63d^7(^4F)4s4p(^1P^\circ)$	x $^4G^\circ_{11/2}$	−0.133
3447	242.362	242.493	Co I	$3p^63d^74s^2$	a $^4F_{9/2}$	$3p^63d^7(^4F)4s4p(^1P^\circ)$	x $^4F^\circ_{9/2}$	−0.131
2864	241.032	241.162	Co I	Unknown		Unknown		−0.130
2838	252.770	252.897	Co I	$3p^63d^74s^2$	a $^4F_{7/2}$	$3p^63d^7(^4F)4s4p(^1P^\circ)$	x $^4D^\circ_{5/2}$	−0.127
2606	241.320	241.446	Co I	$3p^63d^74s^2$	a $^4F_{5/2}$	$3p^63d^7(^4F)4s4p(^1P^\circ)$	x $^4G^\circ_{7/2}$	−0.126
1953	243.087	243.221	Co I	$3p^63d^74s^2$	a $^4F_{7/2}$	$3p^63d^7(^4F)4s4p(^1P^\circ)$	x $^4F^\circ_{7/2}$	−0.134
1426	243.537	243.666	Co I	$3p^63d^74s^2$	a $^4F_{5/2}$	$3p^63d^7(^4F)4s4p(^1P^\circ)$	x $^4F^\circ_{5/2}$	−0.129

The UV wavelength (243 nm) lies beyond the range of the LSA, however the lineshape of the 355 nm and 770 nm lasers which pump the final SFG stage could be ascertained with this device (figure 3.9), and from these an upper bound for the UV beam can be inferred.

The LSA was calibrated against the known vacuum wavelength of a HeNe laser (632.991 nm), prior to measurement of the OPO signal-wave and various harmonics of the Nd:YAG. These data were then fitted assuming a Gaussian line-shape to find the FWHM linewidth - table 3.2.

Table 3.2: The vacuum wavelengths and linewidths (FWHM) obtained by measurement with a *High Finesse* LSA of the various beams employed in the UV laser design.

λ nm	$\Delta\lambda$ [nm]	$\Delta\nu$ [GHz]
1064.501	0.113	29.9
532.246	0.037	39.9
354.831	0.026	61.3
772.448	0.325	163.3

The observed fundamental line-shape is consistent with the Gaussian envelope profile anticipated for a multi-mode free running laser of this kind. Given the precision of the measurement device the internal mode structure was not expected - nor found - to be resolved. This lineshape persists through the harmonics, broadening at each stage due the convolution of the pump beams. In the case of the third harmonic (figure 3.9a) the lineshape is a little broader than expected ($\sim$ 20 %).

The OPO signal-wave lineshape does exhibit some strong features, although these are not easily explained. The mode spacing might be expected to relate to the OPO cavity of length (L), in accordance with,

$$\Delta\nu_{modes} = \frac{c}{2L} \approx 1.67 \text{ GHz} \quad (L = 110 \text{ mm}) . \tag{3.6}$$

Yet the spacing observed is roughly 31 GHz, which could instead be an artefact of interference caused by reflections between the two BBO crystals, or perhaps might result from phase-matching phenomena. Nonetheless, due to the breadth of the third harmonic, this structure should be suppressed in SFG, with the anticipated linewidth for the 243 nm beam being 174 GHz (0.034 nm).

(a) Nd:YAG third harmonic

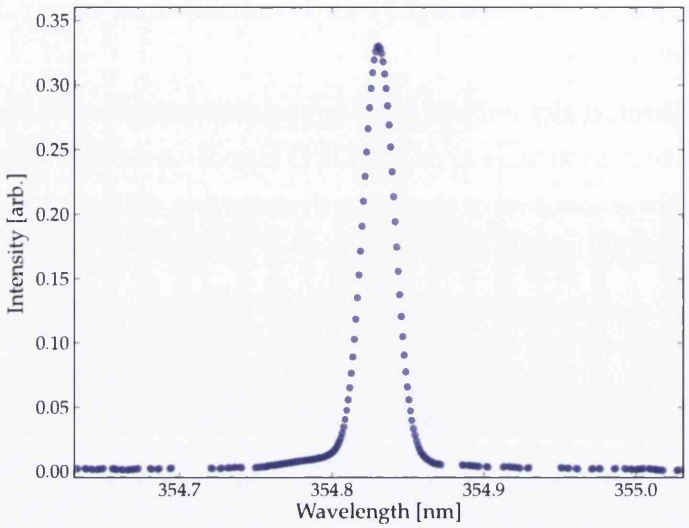

(b) OPO signal-wave

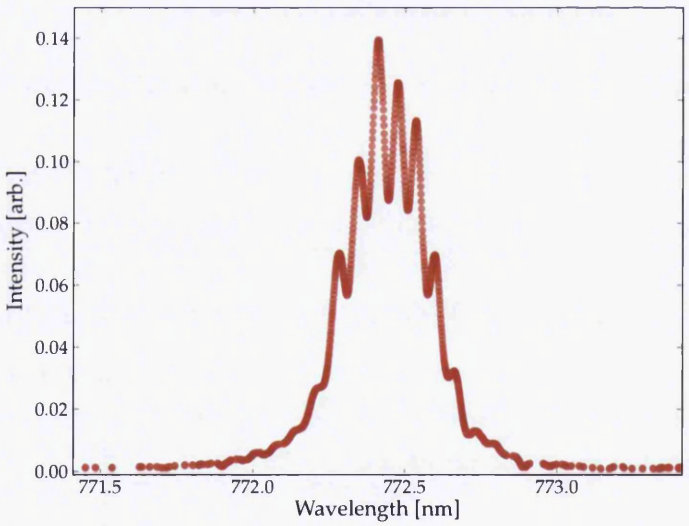

Figure 3.9: Line-shape data taken with a *High Finesse* LSA for (a) the Nd:YAG third harmonic and (b) the OPO signal wave.

Chapter 4

Positron Accumulation

Since the first successes with the two-stage positron accumulator [Clarke *et al.*, 2006], the fundamental hardware of the device has changed little. As one would expect for such a bespoke system, innumerable repairs and upgrades have indeed taken place, each typically unremarkable, yet contributing to a significant cumulative improvement in reliability, efficiency, detection and control.

One notable advancement has certainly been made with regard to the system for data capture and sequencer control (appendix A), primarily enhancing the reproducibility and experimental throughput, and effectively broadening the parameter spaces which can be explored. Contingent on this point - and likely of greater interest to the reader - have been the significant developments in manipulation, in terms of the radial extent and position, of the accumulated positron clouds. These two techniques employ a segmented electrode located in the second-stage of the accumulator, and both are outlined in the following section 4.1.

In particular, control of the radial extent of the clouds by use of the RW technique has been used to increase the density (directly in reduction of the cloud radius, but also indirectly by increasing the lifetime of the trap and with it the number accumulated), with applications in laser studies of positronium (chapter 5). Subtleties of RW operation with regard to both the anharmonicity of the trap and cloud density are explored in sections 4.2 and 4.3, respectively.

4.1 Positron Manipulations

4.1.1 Accumulation and the RW

Concerning the RW technique, many of the investigations performed at Swansea have been focussed on understanding the compression mechanism from a single-particle perspective [Isaac, 2010; Isaac *et al.*, 2011; Isaac, 2013]. This was achieved by accumulating positrons for some fixed period, then accessing the dimensions of the cloud after application of a RW with some frequency (f_{RW}) and amplitude (V_{RW}). By varying the duration for which the rotating field was applied, the compression rate could be found as a function of f_{RW} and V_{RW}. This proved to favourably compare with predictions of a simple model system, which was built on the approximation of ideal RW and trapping potentials (see figure 2.12).

The continuous employment of the RW technique throughout positron accumulation, is well known to reduce losses that are due to expansion to the electrode walls [Baker, 2010; Isaac, 2010; Watkeys, 2008]. Although long realised, understanding the relationship between the trap lifetime and RW parameters has proven a complex problem, which cannot be solved from an ideal trap perspective. This relationship, and further the interplay between accumulation and cooling gas pressure, is studied in the following.

Figure 4.1 indicates the number of positrons accumulated as a function of time, both with and without the RW technique applied for the duration (0.5 V; 9.45 MHz). This plot indicates that - for these parameters - the RW technique increases the lifetime of the trap, from 80 ms to 1.7 s. Notice that without the rotating field the lifetime is much reduced from earlier measurements (e.g. figure 2.10). This is due to the addition of SF_6 as a cooling gas (see section 2.4.2), estimated to be present in the second stage of the accumulator at a pressure of 2.6×10^{-5} mbar. The extra losses are dominated by expansion to the electrodes, caused by collisions with the added gas molecules, which is neutralised by inward transport when the RW is used.

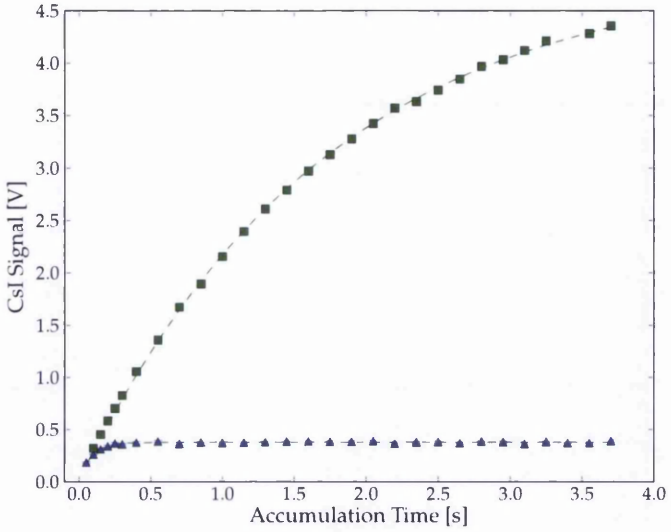

Figure 4.1: Positron accumulation curves, both with (■) and without (▲) the RW technique applied (0.5 V; 9.45 MHz). The green dashed lines represent fits of the form given by equation 2.11.

The complex relationship between cooling-gas pressure and RW parameters is illustrated in the density plots (a, b) of figure 4.2. These show the number of positrons accumulated in 1 s for a range of RW frequencies and cooling-gas pressures, and for RW amplitudes of 0.5 V and 2.0 V, respectively. A number of features of these plots can be relatively easily understood from our understanding of the single-particle dynamics (section 2.4.2).

For increasing cooling gas pressure the number of positrons is generally observed to reduce. As discussed previously, for the frequencies that the RW is inactive, this is most likely dominated by diffusion to the electrodes, hastened by collisions with the SF_6 molecules. Assuming that the vertical bands of enhanced accumulation - centred at approximately 9.5 MHz - indicate the frequencies at which the RW induces inward transport, we adduce that losses here at higher pressures are predominately due to annihilations with the gas molecules.

The centring of these bands is consistent with the single-particle model for axial-

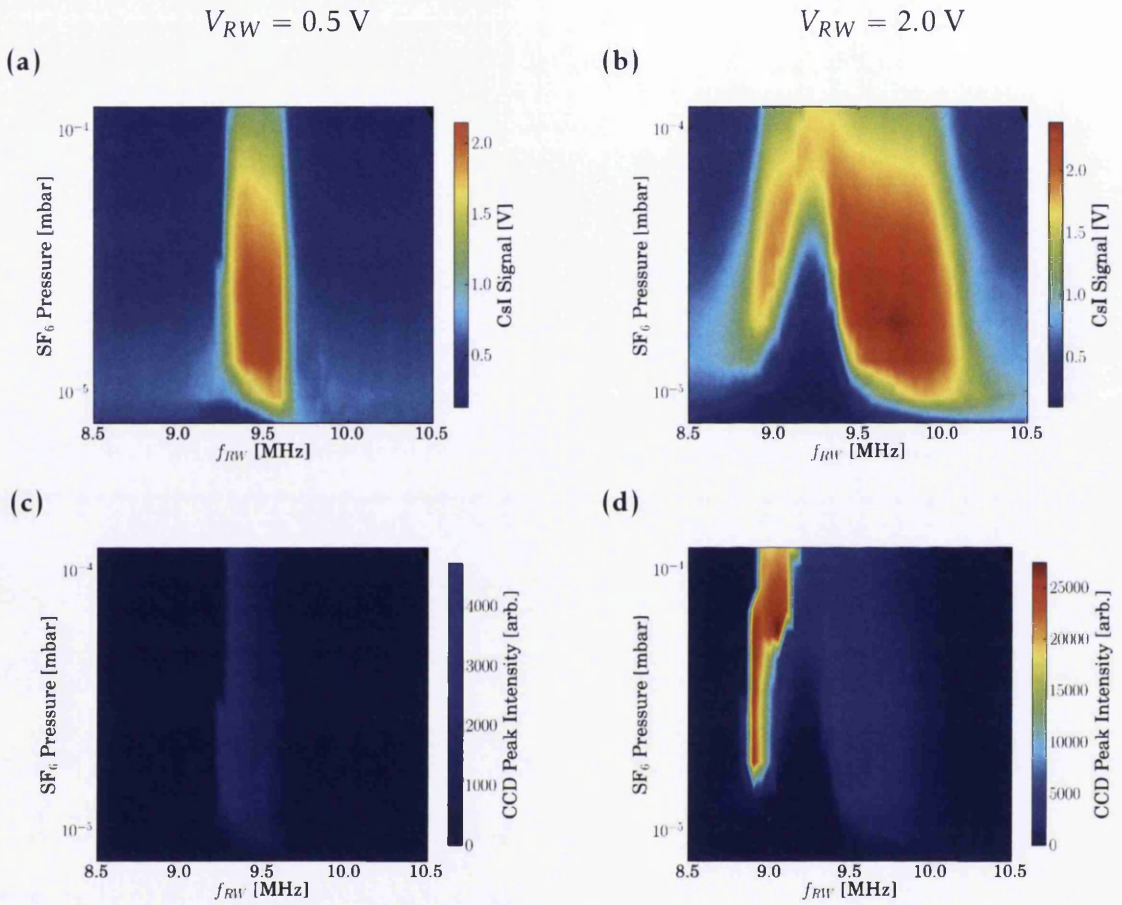

Figure 4.2: Density plots of the CsI signal, indicating the number of positrons accumulated in 1 s (a, b), and the peak intensity observed with the CDD camera (c, d), for a range of cooling gas pressures (log scale) and RW frequencies. The RW amplitude was fixed at 0.5 V (a, c) and 2.0 V (b, d).

isation in a rotating dipole field [Isaac, 2013], though appearing higher in frequency than the expected sum of the magnetron and bounce frequencies $\sim$ 9.4 MHz; as estimated from field calculations. In further agreement with the idealised model, the widths of the bands correlate with the amplitude of the RW - equation 2.21.

At the lowest cooling gas pressures, the RW technique is found to reduce the number of particles accumulated. This is expected, and is attributed to resonant heating of the particles by the rotating electric field. Such heating will excite positrons toward the threshold for positronium formation (8.5 eV for N_2 and 8.8 eV for SF_6), and significant losses will be consequently incurred. These losses persist to higher cooling gas pressure for the larger of the RW amplitudes, further supporting that such relates to heating. Interestingly, this effect is centred at a markedly lower frequency than the enhancement band. This shift cannot be understood from the ideal model, and is addressed in section 4.2.2, where the anharmonicities of the trapping potential are considered.

Figure 4.2 also includes plots of the peak intensity of the CCD image (c, d), recorded as the positrons impinged upon the MCP (section 2.6.1); this measurement corresponds to the areal density of the cloud. Notably, the larger of the RW amplitudes yields significantly ($\times 5$) brighter clouds. It is intriguing that within these plots the maximum intensity is evidenced at the lower frequencies within the enhancement band. This too cannot be understood from the ideal model and is addressed later (section 4.2.2).

4.1.2 Magnetron Orbit Excitation

Recently a need has arisen for precise control of the location to which accumulated particles are ejected - for instance in the loading of multi-cell trap arrays, [Surko and Greaves, 2003]. Autoresonant excitation of the diocotron-mode [Fajans *et al.*, 1999] has been identified as a suitable means to achieve such control over nonneutral plasmas, but these modes do not exist for densities below the plasma regime, and are hence inapplicable to the system described herein.

The diocotron mode arises from the $\vec{E} \times \vec{B}$ fields of the plasma and trap, and is analogous to magnetron motion in the non-interacting regime (section 2.3.1). Incoherent excitation of the magnetron motion is, essentially, expansion of the cloud; in general such is undesirable. However, we have recently developed a technique to excite this motion for the cloud as a collective, retaining the cloud dimensions, yet inducing it to orbit at a tunable radius and with a well defined phase [Mortensen *et al.*, 2013; Mortensen, 2013]. This technique has already found applications within these studies, as a means of mapping frequency variations within the trap (section 4.2) and for alignment purposes (section 5.2.1).

These orbits are obtained by biasing the segments of the RW electrode with a fixed (i.e. non-rotating) dipole field - similar to that described in section 2.4. In the cited works a simple theoretical model is presented, wherein a potential is added to that of the ideal Penning trap, and which is given by:

$$\phi_D = \frac{m_e \alpha x}{q}, \tag{4.1}$$

where α is in proportion to the magnitude of the applied bias. This is found to deform the symmetry of the Penning potential, such that the extremum is radially relocated from the origin by a translation,

$$\vec{k} = \frac{2\alpha}{\omega_z}\hat{x}. \tag{4.2}$$

Were such a field to be applied slowly (w.r.t. the magnetron motion), a particle very close to the centre of the trap, would be transported to the new maxima in the potential; whereas if applied quickly, an adiabatic invariant is broken [Notte *et al.*, 1993] and the particle will begin to orbit about the maxima at a radius $r_D = |\vec{k}|$. If the dipole field is removed as rapidly, the particle will afterward commence orbiting about the original centre, with an orbit radius determined by the its displacement at the moment the pulse ramped down.

Tuning the time for which the pulse is applied (t_1), in addition to the interval

prior to ejection of the particle from the trap (t_2), allows any position in the radial plane to be targeted (within $\sqrt{x^2+y^2} \leqslant 2r_D$). Clouds of positrons initially compressed to the centre of our trap have been found to obey these simple, single-particle dynamics. The concept is illustrated as a schematic in figure 4.3, alongside superposed MCP images of positron clouds ejected at different times during such orbits.

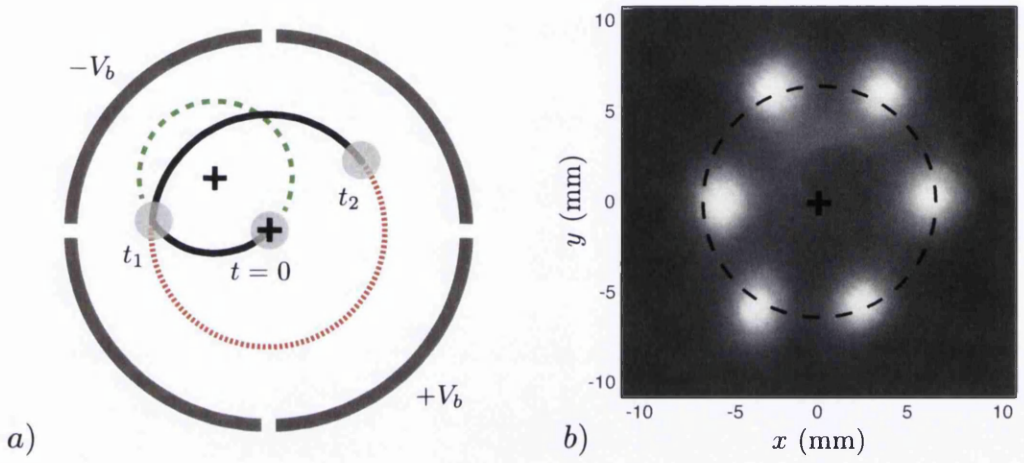

Figure 4.3: Schematic radial cross section of the RW electrode showing the bias voltages applied to opposing segments. The black solid line is the path of the positron cloud (grey disk) during the experiment (see text). The green broken line represents the cloud orbit during application of the bias voltages. The red dotted line follows the orbit after the bias voltages are removed. (b) Combined picture of positron clouds for a number of different positions within one magnetron orbit after a bias voltage of 0.36 V was switched on for 7 µs. The dashed line is a fit of a circle to the magnetron orbit with the cross denoting the centre of the trap. Asymmetries in the transport fields are the likely cause of the slight offsets of the clouds from the fitted orbit. [Mortensen *et al.*, 2013]

Exploration of the range and precision of this technique is well documented elsewhere [Mortensen *et al.*, 2013; Mortensen, 2013]; in addition to the full theory derived from the model outlined above, which is found in excellent agreement with experimental data.

4.2 Anharmonicity and the RW

Underpinning the theory of Isaac [2013], which describes operation of the RW technique in the single-particle regime, is the assumption that the electric field of the positron accumulator is consistent with the perfect quadrupole field of the ideal Penning trap (section 2.3.1). This is a reasonable approximation to the truth, however to explain certain phenomena observed with our system we must invoke the non-ideal, anharmonic components in the potential - such imperfections are typically non-negligible for Penning-Malmberg traps.

4.2.1 Frequency Mapping

In order to discuss the effect of field anharmonicities, we need first to quantify them. This is done with both calculations and observations, by determining the axial bounce frequency ($f_z = \omega_z/2\pi$) of positrons within the trap. In a harmonic trap f_z is a constant, however in the anharmonic case there will be variations depending on the total energy (E) and radial position (r) of a trapped particle.

The calculations were performed with *Wolfram* Mathematica,® which was used to map the solution to the Laplace equation within the accumulator electrodes (equation 2.9), and then to find the bounce frequency for a test charged particle of given E and r,

$$\frac{1}{f_z(E,r)} = \sqrt{\frac{2m}{q}} \int_{z_1}^{z_2} \frac{\mathrm{d}z}{\sqrt{E-\phi(z,r)}}, \tag{4.3}$$

where z_1 and z_2 are the particle's turning points, i.e. the solutions to $E = \phi$. The results are plotted for various kinetic energies as solid lines in figure 4.4. In summary, the bounce frequency on axis decreases for higher energies, and increases with radius to a maximum around 8 mm; the maximum is constant across these energies at ~ 9.5 MHz.

The bounce frequency was experimentally determined by exciting magnetron orbits. Using the technique described in section 4.1.2, the pulse amplitude (α)

and hold time (t_2) was varied, and the position of each cloud recorded at the MCP. From this data the frequency of the magnetron motion ($\omega_- \approx 270$ krad s^{-1}) could be mapped as a function of radius. Assuming a cyclotron frequency of 5.8 Grad s^{-1} ($B_z = 33$ mT), the data from the magnetron frequency map can then be applied to equation 2.6 to determine the equivalent map for the bounce frequency. The result is shown as the points in figure 4.4, and is found to roughly agree with the above calculation, assuming a mean kinetic energy of ~ 400 meV. This is more energetic than might otherwise be expected [see Mortensen *et al.*, 2013], suggesting the applied pulse causes significant heating. *N.B.* within the uncertainty of the magnetic field there is scope to shift the data points by a few hundred kHz, however the radial dependence would not be affected.

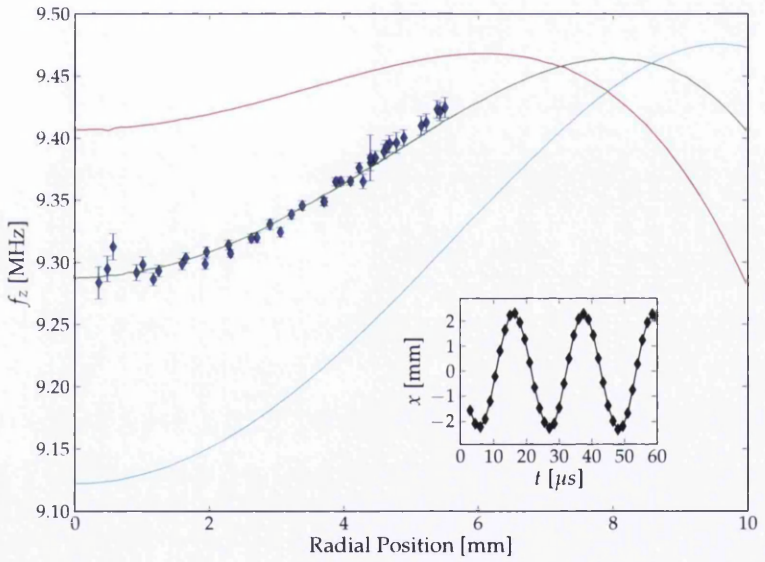

Figure 4.4: The axial bounce frequency ($f_z = \omega_z/2\pi$) as a function of radial position (points), derived from measurements of the magnetron frequency (ω_-) - see text. The error-bars indicate the uncertainty in fitting the magnetron orbits but do not account for the uncertainty in the magnetic field. Calculations (lines) of f_z for positrons displaced from the trap centre with kinetic energies of 100 meV (red), 400 meV (green) and 700 meV (cyan). Inset: an example of the time variance of the x coordinate of positron clouds, which is used to determine ω_-.

4.2.2 Applications

Accumulation and the RW

Having mapped the axial bounce frequency of positrons within the trap, we are now able to offer an explanation for some of the structure observed in the frequency scans of figure 4.2.

The change in bounce frequency with radial position (illustrated in figure 4.4) will alter the frequency detuning between the applied rotating field (ω_r) and upper sideband of the particle motion (ω_0) - see section 2.4.2. Assuming that this perturbation to the ideal RW model will not invalidate its conclusions, we may surmise that both compression and heating from the rotating field, will likewise vary as a function of r.

This simple idea immediately resolves the noted quandary that the optimum drive frequency, with regard to the number of positrons accumulated, lies several hundred kHz above where losses due to heating are most prevalent. The interpretation is as follows: when the drive frequency is closer to resonance at higher radii than on-axis, it provides a restoring force to those particles which drift outward, i.e. preventing losses to the electrode walls, yet the heating effect to those particles at lower radii is enervated and thus losses to positronium formation curtailed. Conversely, when resonant on-axis, the particles cannot escape the heating from the rotating field and more cooling gas is required to accrue an appreciable number. This phase-space selective, i.e. pseudo-potential depiction, is in many ways analogous to other confinement techniques, such as magneto-optical trapping.

The anharmonicities of the trap may also explain why the densest clouds are found with lower drive frequencies and higher field amplitudes. As a point of contrast we consider a low amplitude field that is resonant on-axis (with sufficient cooling), for which the compressive force will be felt strongly at $r = 0$, but much less so nearer the electrodes. This is a consequence of the sharply peaked cusp function of the compression curve (equation 2.21; figure 2.12) and hence allows sufficiently off-axis particles to diffuse outward and be lost. For a larger field similarly tuned,

at moderate cooling-gas pressures the heating is demonstrated to cause losses, however, if detuned below axial resonance the adverse heating is lessened, and compression at $r = 0$ will be akin to that for the weaker field. Unlike the former case however, significant compressive forces will still be felt at larger radii, as a result of the broad wings of the cusp function, and thus the particles there are transported inward and the densest clouds achieved.

It's also worth considering the role of kinetic energy with regard to particle interactions with the rotating field. In the anharmonic well, the axial bounce frequency - and thus the strength of RW interaction - will vary with a particle's energy quite strongly; especially close to $r = 0$, as shown in figure 4.4. Furthermore, resonant fields will impart energy that will shift these frequencies, therefore detuning the resonance, whilst collisions with neutrals will cause both cooling and radial displacement, which further complicates matters. The intricacy of the situation makes it very difficult to separate the mechanisms experimentally - seemingly this is a problem best tackled by simulations [Marjanović *et al.*, 2013]. What may be noted without such is that in the region of $r = 6$ mm to 9 mm the bounce frequency calculated at each energy reaches ~ 9.45 MHz. Perhaps this pan-energy resonance further explains why the optimum frequency for accumulation is found here - in particular with low amplitudes, for which the resonance is narrow.

Frequency Chirping

Having established a plausible explanation for the observations made when the RW technique is employed during accumulation, the natural reaction is to try and exploit our understanding, for improved accumulation and compression.

A reasonable suggestion would be to accumulate positrons in a rotating field which is resonant off-axis (enhancing the trap lifetime but causing minimal heating and therefore requiring less cooling-gas), followed by chirping the frequency down, effectively sweeping the compressive force inward through the trap radii, in the hope of achieving a small dense cloud prior to extraction.

(a)

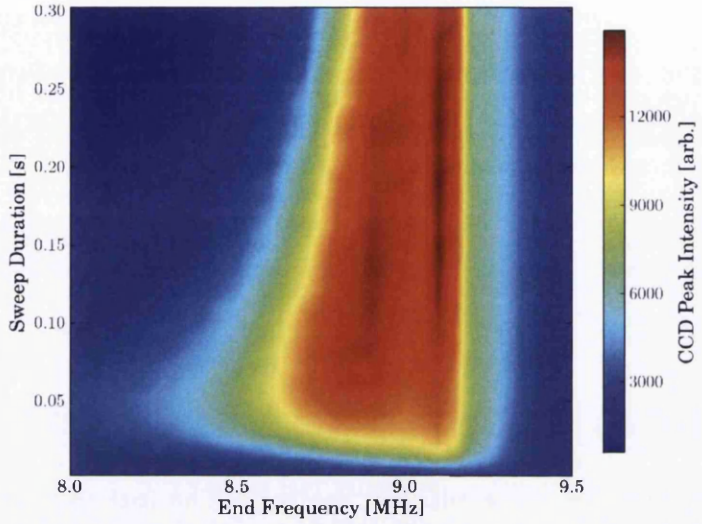

(b)

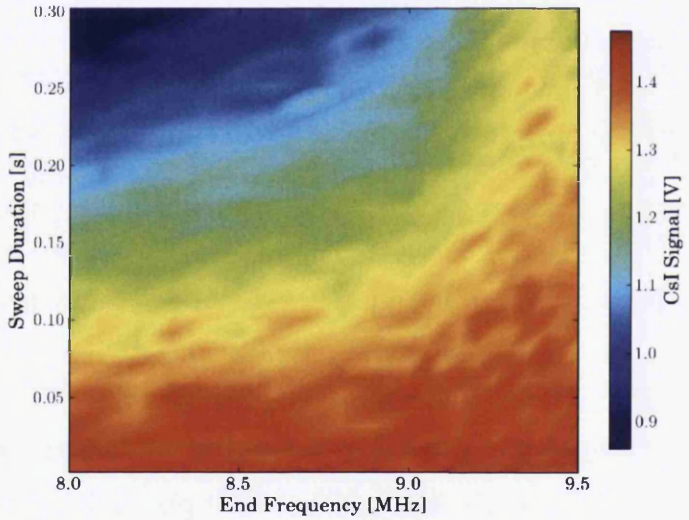

Figure 4.5: The CCD peak intensity (a) and CsI signal (b), indicating the central density and number of positrons accumulated in 1 s with the RW applied at 0.5 V and 9.45 MHz. The SF_6 pressure is estimated at 1.8×10^{-5} mbar. Prior to measurement the rotating field is swept to a variety of end-frequencies for a given sweep duration.

Figure 4.5a shows the peak intensity of the CCD image of clouds accumulated for 1 s with a RW of 0.5 V and 9.45 MHz, and with cooling-gas present at an estimated 1.8×10^{-5} mbar. Following accumulation a chirp is applied to the RW, which is swept to some end frequency in some variable period of time. The plot shows how the density is enhanced by more than a factor of six, when swept to approximately 9.1 MHz in at least 100 ms. If this is assumed to be the on-axis bounce frequency, we may estimate the kinetic energy of the particles (parallel to the magnetic field) to be 700 meV, implying substantial heating. The number of positrons is relatively unaffected by the sweep, naturally depleting for longer sweep times due to the usual losses, which are somewhat mitigated when compression is achieved - figure 4.5b. A cross-section through the peak of two images, before and after successful chirping, is given in figure 4.6. *N.B.* although in this case significant improvement in density is achieved versus the static 0.5 V RW, denser clouds are yet produced with the 2 V rotating field.

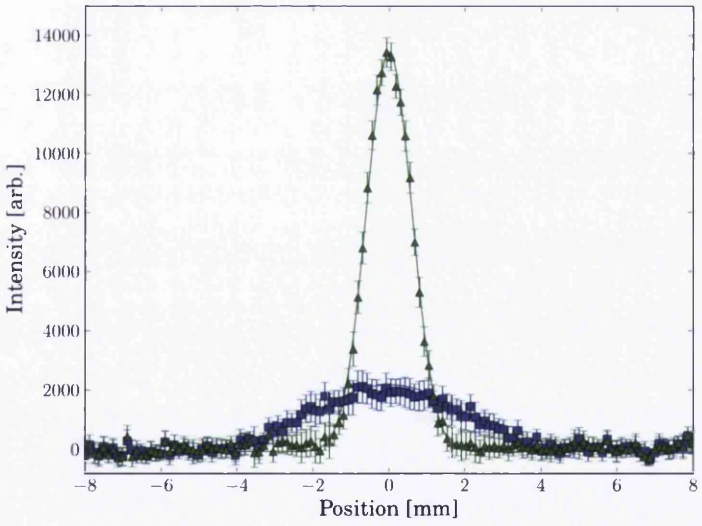

Figure 4.6: Cross-section through the maximum of a 2D Gaussian fit (lines) to data (points) of clouds accumulated for 1 s and imaged by the CCD. RW compression of 0.5 V at 9.45 MHz (■), followed by an 150 ms linear chirp down to 9.1 MHz (▲), as described in the text.

4.3 Density Considerations

The developments made with improving positron accumulation and compression, forces a rethink on the density regime of the "clouds" we amass; hitherto assumed to be a collection of non-interacting, single particles.

Unfortunately, a lack of calibration for our detectors makes it difficult to accurately assess the number of positrons. However, we can make a conservative estimate based on the source strength and expected capture efficiency, that we are routinely achieving in the region of at least 10^5. For the size of the clouds as measured from MCP images, this finds the Debye length (equation 2.16, ~ 1 mm) to be comparable to the cloud dimensions. Although not strictly dense enough to be considered a plasma, we might classify such clouds as "rarified plasmas" [Sarid *et al.*, 2002] and some collective phenomena (e.g. shielding, waves, and global thermal equilibria) accordingly presumed. Indeed, self-rotation of the "plasma" likely inhibits shearing (caused by variance in the magnetron frequency across its diameter), following excitation of magnetron orbits (section 4.1.2).

It has been the goal of this work to absolutely maximise the density of positron clouds, in order to subsequently obtain the most dense plumes of positronium for laser spectroscopy (chapter 5). In the following section (4.3.1) we consider how the space-charge of such dense clouds can influence accumulation, in particular with regard to the RW. In the final section of this chapter (4.3.2) we consider the pulse length (in time) of the accumulated clouds, and how this might be minimised to achieve the maximum temporal overlap between the positronium plume and pulsed laser (chapter 3).

4.3.1 Space-Charge and the RW

One of the best known phenomena pertaining to collections of charges is that of space-charge i.e. the charge density that exists in free space. This will alter the electric fields within the trap, and will therefore exert an influence on the dynamics

of the charges which make up the collection. Gauss's law must be solved to find the electric potential for the combined system of electrodes and charges, which in its differential form is given by,

$$\nabla^2\phi = -\frac{\rho}{\epsilon_0}, \tag{4.4}$$

(i.e. Poisson's equation) where ρ is the charge density. Note that this simplifies to the Laplace equation (2.8) in the absence of charges. As the electric field and particle distribution mutually affect one another, self-consistent solvers are required to determine the equilibrium solution.

During accumulation the number of charges increases and accordingly the electric potential of the well is expected to be perverted from its vacuum state. The space-charge will consequently cause a shift in the motional frequencies of the trapped particles, which in turn may alter the influence of the RW technique and thus the lifetime of the trap. Such an effect is suggested to lie behind the strange shape of the accumulation curve in figure 4.7, showing that eventually sufficient charges are accumulated to improve the effectiveness of the RW and thus increase the trap lifetime.

A longer, flatter well (identical to the traditional case (table 2.4) except with E5 lowered to 28 V) was implemented to reduce the influence of space-charge on accumulation. We estimate the space-charge contribution to the electric potential using a self-consistent Poisson solver, which was kindly given by Prof. Francis Robicheaux (ALPHA Collaboration). The solver was configured with the electrode geometries and applied biases of both the traditional and longer well, for a plasma of 10^5 positrons at 1000 K - the results are shown for the electric potential on-axis in figure 4.8, in addition to the vacuum potential calculation for the same region.

These plots show that, in the case of the shorter (traditional) well, the space-charge contribution has a significant flattening effect on the well shape, whereas for the longer well the space-charge is much less and its distortion to the well profile reduced. These electric potentials were applied to calculations of the axial bounce

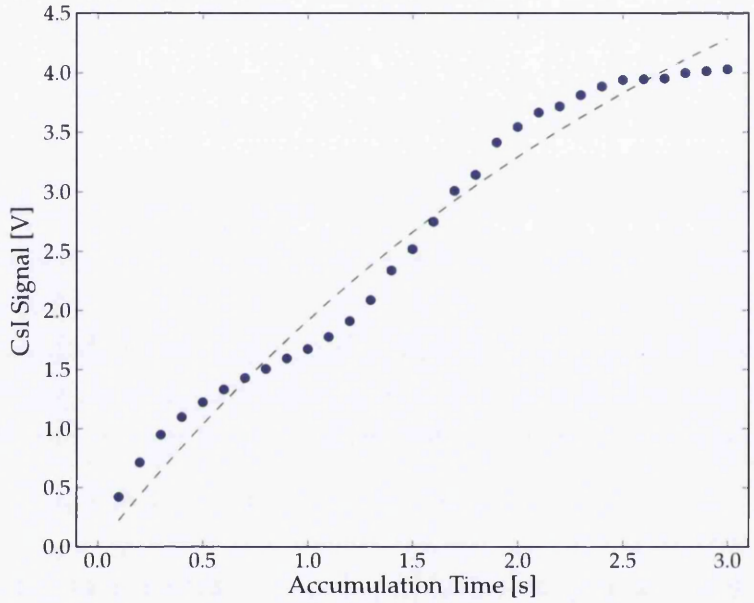

Figure 4.7: Example accumulation curve for the simple trapping scheme described in table 2.4 with an applied RW (2 V; 8.7 MHz). The green dashed line represents a fit of the form given in equation 2.11 ($\tau = 3 \pm 0.2$ s). The disconformity between data and fit is thought to result from shifts to the bounce-frequency caused by a build-up of space-charge, which dynamically alters the effectiveness of the RW technique and consequently the trap lifetime.

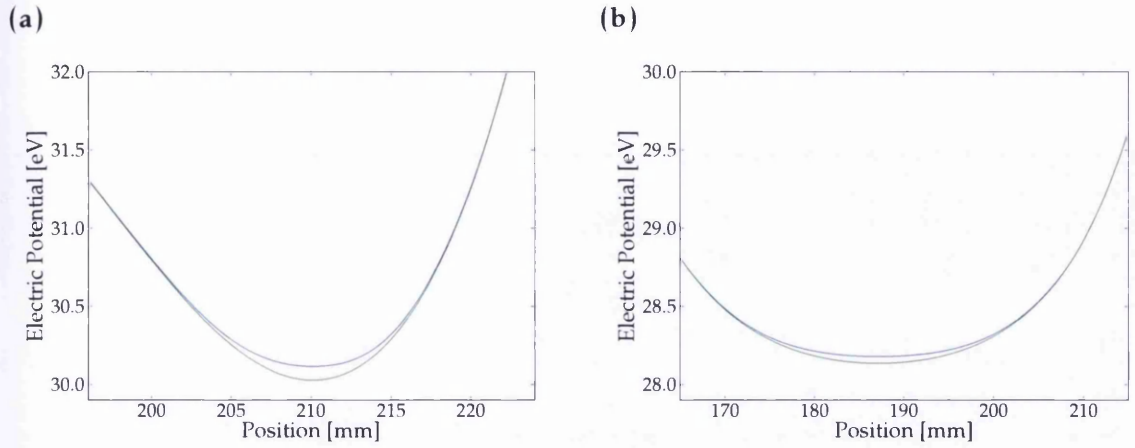

Figure 4.8: The electric potential on-axis (i.e. $r = 0$) in vacuum (green) and including the space-charge contribution of 10^5 positrons at 1000 K (blue), for the traditional accumulation scheme (a) and an alternative, longer well (b) - see text.

frequency (equation 4.3), the result of which (figure 4.9) ratifies this observation, indicating much closer agreement between the vacuum and space-charge instances for the longer well in comparison to the traditional version. The calculations depicted in figure 4.9a also support the explanation given above for the unusual accumulation curve of figure 4.7. These show that positrons with a few hundred meV will come onto resonance with the 8.7 MHz rotating field once sufficient space-charge is accrued.

The bounce frequency is substantially reduced in the longer well - approximately 2.7 MHz for low energies. Accumulation is accordingly found to be optimised with the RW technique applied at 2.65 MHz (1.4 V). Despite the highly non-harmonic characteristics of this well-shape the compression operates similarly to the harmonic case, although with apparently less heating; likely due to the longer cloud being slightly removed from the RW electrode. The assuaged requirement for cooling-gas accordingly results in longer lifetimes than can be achieved with the traditional well ($\sim$ 3.7 s), and hence the longer design was adopted for the accumulation scheme (see table 4.1) employed for the positronium spectroscopy studies (chapter 5).

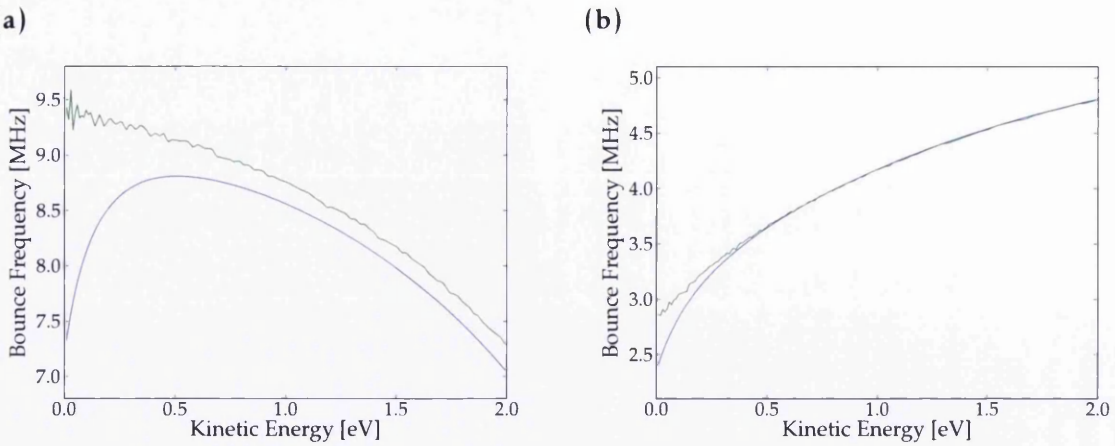

Figure 4.9: The bounce frequency (f_z) on-axis (i.e. $r = 0$) in vacuum (green) and including the space-charge contribution of 10^5 positrons at 1000 K (blue), for the traditional accumulation scheme (a) and an alternative, longer well (b) - see text. The ripples in the result are thought to be an artefact of the resolution of the calculations.

4.3.2 Bunching

To obtain the strongest signal for laser spectroscopy (particularly desired at this proof-of-concept stage), the entire positronium plume would ideally be probed within the 8 ns laser pulse. In order to achieve the maximum interaction time, it is therefore advantageous to minimise the length of the Ps pulse, e.g. by means of time-focussing the positron pulse employed in forming the Ps atoms.

Early attempts at achieving short e^+ bunches involved ejecting the particles from the trap as quickly as possible, by ramping the exit electrode voltage (E7) to ground in roughly 35 ns with a "fast pulser". However, rather than shortening the antiparticle bunch length this proved to extend it. This failing is thought due to uneven distortions to the electric potential across the cloud's length as the electrode is ramped down, which acts to increase the energy-spread of the positrons and thus the range of arrival times at the conversion target.

Manipulating the base of the well could - in principle - significantly reduce the

pulse length of the cloud by the opposite effect. By lowering the exit electrode to around 60 V, then raising the well until particles escape over its potential, the slower tail of the cloud could be provided a carefully tuned kick, such that these particles "catch up" to the earlier escapees, for synchronous arrival at the target. Unfortunately, the electronic configuration for the RW electrodes prevented control of the well at the bandwidth required.

Ultimately, the shortest pulses achieved in this work were measured to be 32 ns FWHM at the target (section 5.1.1). These clouds were accumulated for 3 s in the longer well (see above), then axially compressed and allowed to cool into a single electrode, before lowering E7 to eject the particles. The gate electrode need only be selected to drop to 50 V for all of the particles to escape, due to significant overshoot in the amplifier output when ramped down (here dropping to $\sim$ 30 V). This found only a marginal improvement over previous attempts, and with more attention to the ejection scheme it's expected significant progress might be made - see chapter 6 for further discussion. This scheme was employed in the laser spectroscopy studies of chapter 5, and is depicted in table 4.1.

Table 4.1: The accumulation scheme designed to maximise the number and density of positrons accumulated in the two-stage buffer gas accumulator. The RW parameters are 1.4 V and 2.65 MHz.

Description	Step Time	RW	Voltages [V]							
			E0	E1	E2	E3	E4	E5	E6	E7
Accumulate	3 s	ON	45	44	38	35	34	28	28	140
Squeeze well	3 µs	OFF	140	60	60	60	60	60	28	140
Wait	1 ms	OFF	140	60	60	60	60	60	28	140
Empty trap	3 µs	OFF	140	60	60	60	60	60	28	50

Chapter 5

Laser Excitation of Positronium

As alluded to by the title of this thesis, laser excitation of the positronium atom is the primary goal of these studies. It is hoped that such will be a proof-of-concept precursor to forming Rydberg states of positronium (section 1.3.2), with potential applications in antihydrogen synthesis.

In the following chapter we discuss how the techniques outlined in chapter 4 - pertaining to accumulation and manipulations of positrons - have been applied to the formation of positronium (section 5.1). The application of a UV laser (chapter 3) in exciting the Lyman-α transition of Ps is later reviewed (section 5.2), and laser measurements of the Doppler profile of the interval are also presented (section 5.3).

5.1 Positronium Formation

Positronium atoms are formed by embedding a short bunch of positrons (section 4.3.2) into a porous silica sample held in an electrode assembly (section 2.5.1). The formation of Ps is inferred from the slow decay component of the annihilation signal measured with a PWO scintillating crystal and PMT detector (section 2.6.2). This technique is termed *single shot positron annihilation lifetime spectroscopy* (SSPALS) and was developed by Cassidy *et al.* [2006b].

Although SSPALS promises information regarding the formation of Ps from a "single shot," in practice many repeat measurements are made and the signals averaged, to improve the statistics. This is necessary due to the low light output of PWO and the relatively few positrons which can be amassed with the positron accumulator, in comparison to the cited work.

The disadvantage of SSPALS over traditional beam based PALS, is that a number of time dependent features (primarily the time distribution of positrons and measurement artefacts) are convolved with the positronium signal. Consequently, a simple model has been developed in an attempt to deconvolve and extract useful elements of the SSPALS signal - this is elucidated in the following section.

5.1.1 SSPALS Curve Fitting

To construct a model of the anticipated SSPALS function, we first assume that the arrival time of positrons at the sample follows a Gaussian distribution,

$$N_{e^+}(t) = \frac{Ae^{-\frac{t^2}{2\sigma^2}}}{\sqrt{2\pi}\sigma}. \tag{5.1}$$

Following implantation, the two most prevalent positron fates are expected to be either *i)* instantaneous annihilation (< 1 ns) to two gammas, or *ii)* production of free ortho-positronium (fraction 'S') preceding exponential decay into three gammas with a characteristic time of 'τ_S'. In accordance with this presumption the number of gammas as a function of time may be described as

$$N_\gamma(t) = \int_{-\infty}^{\infty} \frac{Ae^{\frac{-t'^2}{2\sigma^2}}}{\sqrt{2\pi}\sigma} \left(2(1-S)\delta(t-t') + \frac{3S}{\tau_S} \mathrm{H}(t-t') e^{-(t-t')/\tau_S} \right) dt', \tag{5.2}$$

where $\delta(x)$ is the Dirac delta function and $\mathrm{H}(x)$ the Heaviside step function.

To determine the signal function we assume linearity in the crystal, such that the probability of detecting a decay (i.e. the number of photons) multiplied by

the mean detection signal per decay is a constant. Essentially we drop the factors of 2 and 3 from equation 5.2, and an added constant is absorbed into A. This is then convolved with the detector function, approximated as a step function with an exponential decay and a characteristic time of 'τ_D,' which gives the anticipated signal function of the form:

$$V(t) = \frac{-Ae^{-t\left(\frac{2}{\tau_D}+\frac{1}{\tau_S}\right)}}{2(\tau_D-\tau_S)}\left(S\tau_D e^{\frac{2t}{\tau_D}+\frac{\sigma^2}{2\tau_S^2}}\left(1+\mathrm{Erf}\left[\frac{-\sigma^2+t\tau_S}{\sqrt{2}\sigma\tau_S}\right]\right)-\right.$$
$$\left.(\tau_D+\tau_S(S-1))e^{\frac{\sigma^2}{2\tau_D^2}+t\left(\frac{1}{\tau_D}+\frac{1}{\tau_S}\right)}\left(1+\mathrm{Erf}\left[\frac{-\sigma^2+t\tau_D}{\sqrt{2}\sigma\tau_D}\right]\right)\right), \tag{5.3}$$

where Erf(x) is the error function.

The above is only expected to approximate the signal shape, ignoring as it does known artefacts of measurement, such as the PMT/ oscilloscope bandwidth, as well as non-linearity, rise time and afterglow in the PWO. Furthermore, sure physical effects are overlooked, including positronium diffusion time within the sample [Cassidy *et al.*, 2010a] and annihilation of o-Ps confined to pores ($\tau_{\mathrm{pore}} \approx$ 74 ns, Crivelli *et al.* [2010]). Nonetheless, the dominant features having been taken into account, equation 5.3 is found to fit well to experimental data, as shown in figure 5.1.

The o-Ps fraction parameter, $S = 33$ %, is in reasonable agreement with the expected value of ~ 30 %, yet the characteristic time of the slow decay component, $\tau_s = 120$ ns, is significantly shorter than the field free o-Ps vacuum lifetime, 142 ns. This may be explained by the magnetic field in the region of the target, which is expected to cause quenching of the triplet state $m_s = 0$ (see section 5.2 and Cassidy *et al.* [2010b]), reducing the average o-Ps lifetime. Furthermore, the trace may be distorted by a medium-fast decay component in the PWO crystal ($\tau_{\mathrm{med}} \approx 30$ ns, Qu *et al.* [2002]), which has not been taken into account by equation 5.3.

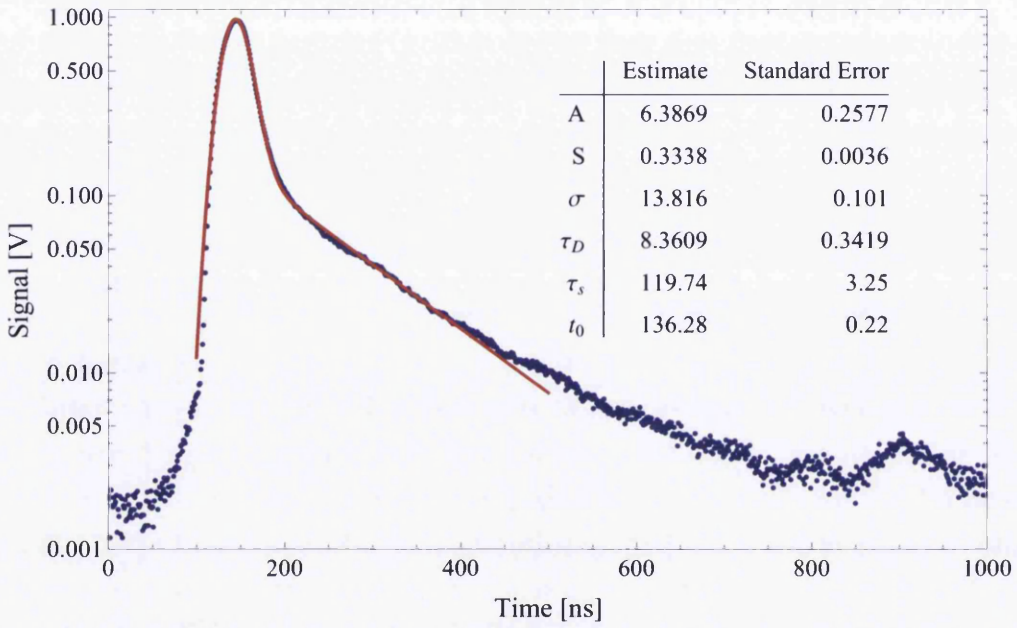

Figure 5.1: Example SSPALS trace for positrons implanted at 2 keV into porous silica. The data (points) from 100 ns to 500 ns has been fitted with equation 5.3 using *Wolfram* Mathematica,® (solid line, parameters inset). The fit parameters are as described in the text, and - where applicable - given in units of ns. The value t_0 represents the arrival time of positrons. The slow decay component suggests in-vacuum annihilation of ortho-positronium.

5.1.2 Implantation Depth

The depth to which positrons are implanted into a porous silica sample is naturally expected to correlate with the time that it takes any positronium atoms subsequently formed to diffuse back to the surface [Cassidy *et al.*, 2010a]. Consequent to increasing the time spent in the sample will be a concomitant increase in the number of collisions that a Ps atom will undergo, and with each collision there is a chance to lose energy or annihilate.

For a large excitation signal, many and cool positronium atoms are desirable; the latter criterion being due to the noted susceptibility of positronium to significant Doppler broadening (section 1.3.2). In accordance with the arguments above, there is then an optimum depth to which positrons should be implanted, to compromise between the fraction of Ps that survive into vacuum and their temperature.

The implantation depth is adjustable by biasing of the sample mount in the target assembly (figure 2.15), with some negative (i.e. attractive) electric potential. Figure 5.2a shows how the fraction of free o-Ps annihilations (S, determined by fitting equation 5.3 to SSPALS traces) decreases with the e^+ implantation energy, across a 3 keV range. Although the temperature of the emitted positronium cannot be ascertained in the same manner, the increase in τ_s shown in figure 5.2b could be interpreted as a reduction in the emitted o-Ps energy at higher implantation depths. The argument follows that, as the detector is so close to the sample, the fastest Ps atoms will transport to regions away from the crystal, thereby reducing their cross-section with it, and suppressing the detection of gammas at later times.

5.2 Laser Excitation and Magnetic Quenching

The UV laser described in chapter 3 was designed for efficient excitation of the Lyman-α ($1^3S - 2^3P$) transition in positronium, having an especially broad linewidth in order to maximise the frequency overlap between the laser and the Doppler broadened interval (see section 1.3.2).

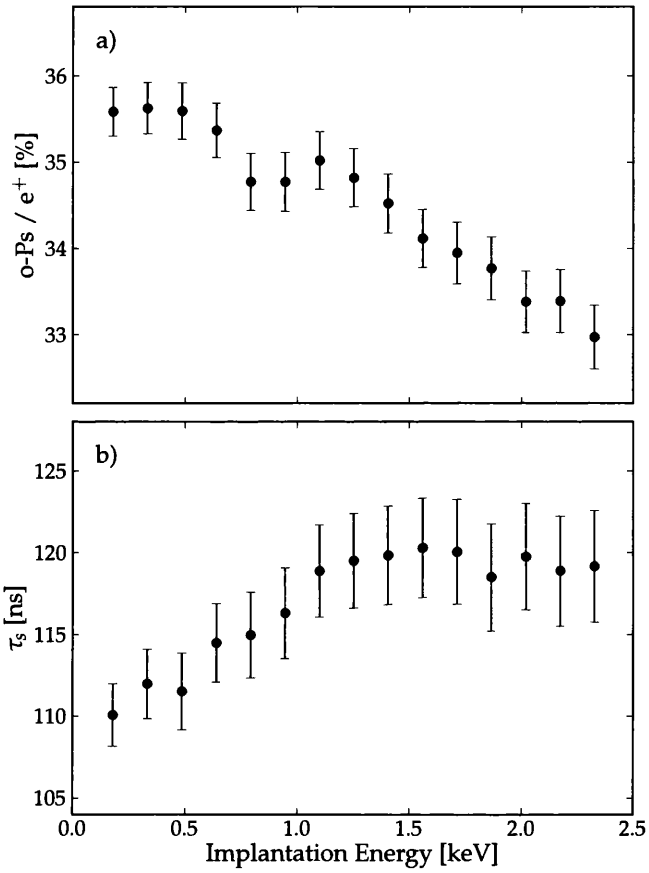

Figure 5.2: (a) The fraction (S) of free, ortho-positronium formed by implanting positrons at various energies into a porous silica sample, and (b) the slow decay component (τ_s) of the SSPALS trace. The values for S and τ_s were determined by fitting equation 5.3 to SSPALS traces recorded from the PWO/ PMT detector. The error-bars indicate the uncertainty in the fit.

In the following sections we discuss the - arguably more critical - overlap between the laser and positronium cloud with regards to space (section 5.2.1) and time (section 5.2.2). Assuming that these challenges are met and excitation of Ps is achieved, raises the question of how the experimentalist is to know of his success, i.e. how to detect such excitation events?

There have been a number of detection schemes previously explored at Swansea - most vehemently that of two-photon ionisation and recapture of the positrons in a Penning trap [Kerrigan, 2011; Watkeys, 2008] - however, a simple and effective technique is in use of SSPALS.

Assuming no external electromagnetic fields, in the $n = 2$ state the lifetime of Ps is longer than its ground-state equivalent and, in principle, this can be observed in the long lived component of the SSPALS decay. However, as the radiative decay to the ground-state is very fast (3.2 ns) the annihilation signal will only be marginally depleted during the laser pulse. A far stronger indication of optical pumping is found if excitation occurs in a magnetic field ($\gtrsim$ 10 mT), which causes Zeeman mixing of the singlet and triplet states with the same magnetic quantum number (recall figure 1.5) [Dermer and Weisheit, 1989]. The admixture is greater for higher n, such that laser excitation results in an increased annihilation signal due to a marked reduction in the triplet lifetime. This is known as magnetic quenching [Cassidy *et al.*, 2010b; Ziock *et al.*, 1990b] and is readily detectable with SSPALS. This technique is exploited repeatedly in the remainder of this chapter - for an example of quenching in an SSPALS trace, see figure 5.4. The field necessary for quenching is greater than that provided by the coils ($\sim$ 7 mT), which is accordingly augmented by that of a permanent magnet ($\sim$ 100 mT) - depicted in figure 2.15.

5.2.1 Alignment

The progress made in positron compression described in chapter 4, was largely motivated by the desire for small, dense plumes of positronium with which to perform laser spectroscopy. Whilst this improves the likelihood of observing an

excitation signal, it introduces an added practical difficulty in ensuring that the relatively small laser/ positron beams overlap physically.

This is tackled by aligning the UV laser to the mechanical references of the windows of cross IV, and subsequently using this beam to guide the positioning of the target assembly (figure 2.15) to the centre of the cross. To ensure that accumulated positrons impinge on the silica target along the centre axis of the cross (through which the laser passes) the assembly ring electrode is biased to +80 V, blocking all but those particles impinging on its centre; *N.B.* positrons are ejected from the accumulator at $\sim$ 30 eV. Fine adjustments are then made to the steering coils in order to maximise the annihilation signal on a CsI detector placed behind the assembly.

The alignment was confirmed by use of the magnetron kicking technique (section 4.1.2), configured to trace a cross-hair in the horizontal and vertical directions, and recording the annihilation signal of positrons transmitted through the ring electrode (biased as before). The results are shown in figure 5.3 and indicate alignment of the accumulated positrons to the centre of the electrode of better than 0.5 mm.

5.2.2 Timing

As crucial to achieving excitation as the alignment described above, is in ensuring that the laser pulse and positronium plume pass through the interaction region concurrently. This is non-trivial considering the FWHM length of the positron cloud is estimated at 32 ns (determined from fits of equation 5.3 to SSPALS traces) and the laser pulse is even shorter at just 8 ns long.

The Nd:YAG flash lamp and Q-switch (section 3.2) are triggered remotely by a *Berkeley Nucleonics Corporation* 555 pulse generator; for optimal operation, the Q-switch trigger is delayed by 180 µs relative to the flash lamp. This device is controlled by an external trigger administered by the FPGA, in order to synchronise the positron accumulation sequence with the UV beam. The pulse generator has a

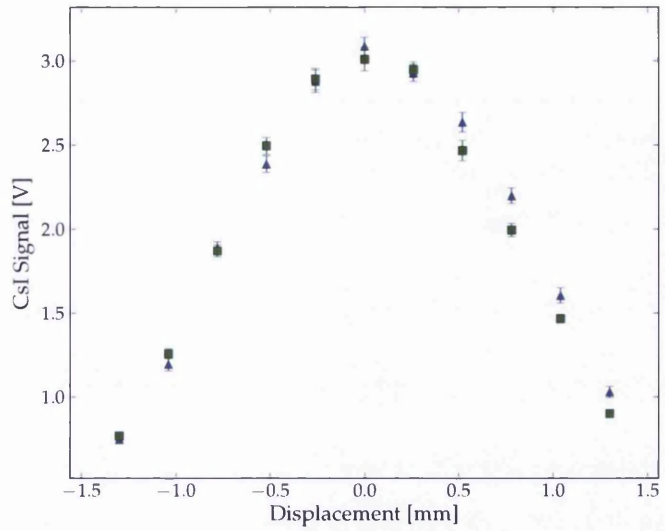

Figure 5.3: The annihilation signal for positrons transmitted through the alignment electrode (+80 V) of the target assembly (figure 2.15), for various vertical (▲) and horizontal (■) displacements of the accumulated cloud.

1 ns timing resolution on its output channels, however its absolute timing accuracy is limited to 15 ns by its external trigger input, imparting an unfortunate jitter onto the synchronisation. Throughout the 3 s accumulation sequence the laser is continuously triggered at a rate of 10 Hz, to keep the temperature of the active rod, and hence also the laser intensity, stable.

To select the approximate time at which to trigger the UV laser during a sequence, an additional laser beam was utilised as a reference. This beam was obtained from the residual 1064 nm pulse left over from the first SFG of the UV laser design (section 3.3.1). Passing this beam through a KDP nonlinear crystal yielded a $\sim$ 4 mJ pulse of the second harmonic, 532 nm. This beam (green) was steered into cross IV (figure 3.7), via a path arranged to match in length that for the UV laser. A *Thorlabs* SV2-FC 2GHz Si Photodetector (S.N. 2262) clamped to the cross IV exit port and aligned to receive the 532 nm beam, thus provided a signal for

the laser timing which, by adjustment of the sequencer timings, could be matched to the arrival of the positrons, as measured with the PWO/ PMT gamma detector (section 2.6.2).

It was not exactly clear what (if any) laser timing would provide the strongest excitation signal. Therefore - utilising a zetetic approach - the system was configured for SSPALS measurements, the UV laser tuned to the Lyman-α wavelength, and a variety of trigger times attempted across a 400 ns range. A selection of traces are shown in figure 5.4, with those where the laser arrives approximately 80 ns after the positrons displaying a discernible excess in annihilations shortly after the reference laser pulse is detected.

5.3 Doppler Profile of the Lyman-α Transition

By tuning the frequency of the UV laser that pumps the $1^3S - 2^3P$ transition, and quantifying any excess in the SSPALS traces due to magnetic quenching from the excited state, the Doppler broadened linewidth of the interval can be observed. The linewidth as measured will be correlated with the temperature of the positronium distribution parallel to the silica surface wherein the atoms form, and is expected to reduce with increasing formation depth [Cassidy *et al.*, 2010b], i.e. positron implantation energy (section 5.1.2).

The process of quantifying the excitation signal (f) is performed by summing the points within a 10 ns window, which was determined by inspection to include any quenching excess. *N.B.* this time is relative to a trigger for data acquisition, which itself is fixed (arbitrarily) with respect to the time of the laser trigger. Because of shot-to-shot variations in the number of positrons, this sum is then normalised against the entire SSPALS trace, and then averaged across 300 repeats. Due to acceleration of positrons between the grid and target, it was necessary to assess the arrival time (t_0 - see figure 5.1) individually for each different bias, from which the

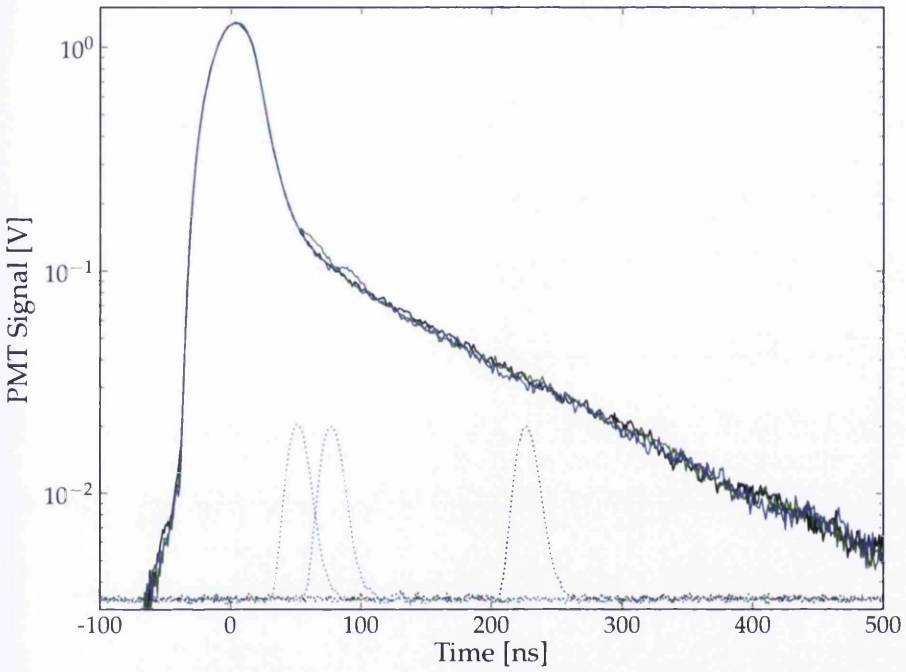

Figure 5.4: A selection of SSPALS traces (log scale) for different UV laser trigger times. Overlaid are the corresponding Si diode detector pulses (dots, arbitrary rescaling). Positrons implanted at 2 keV and the data averaged from 100 repeats. A small excess in the annihilation signal is observed for the laser pulses around 80 ns, indicating Ps excitation and subsequent magnetic quenching. *N.B.* the time-scale has been adjusted such the the positrons' arrival is found at $t_0 = 0$. The length of the averaged laser pulses is much broader than the 8 ns measured of a single pulse; this is a result of jitter in the trigger timing.

SSPALS total was defined as an integral relative to this trigger, i.e.

$$f = \int_{214\,\mathrm{ns}}^{224\,\mathrm{ns}} V(t)\,\mathrm{d}t \Big/ \int_{-20\,\mathrm{ns}}^{350\,\mathrm{ns}} V(t+t_0)\,\mathrm{d}t\,. \tag{5.4}$$

The excess signal (g) is subsequently defined as the difference relative to the background (f_b, laser off-resonant) of the excitation signal f,

$$g = \frac{f - f_b}{f_b}\,. \tag{5.5}$$

This excess has been plotted as a percentage in figure 5.5, which shows a clear resonance in the region of 243 nm that narrows with increasing target bias. The FWHM of the linewidth, as determined by fitting each plot with a Gaussian function, is shown against the implantation energy of the positrons in figure 5.6.

The fit parameters for the highest implantation energy of 2.9 keV finds the Lyman-α transition wavelength to be 243.020 ± 0.007 nm (corrected for the refractive index of air, $n = 1.00027$). This is in agreement with the 243.021 nm measurement of the $1^3\mathrm{S} - 2^3\mathrm{S}$ transition by Chu *et al.* [1984].

The Gaussian width from the same fit ($\sigma = 0.056$ nm) gives an estimate of the mean kinetic energy associated with motion in the direction of the laser,

$$E_x = \frac{1}{2} m_{Ps} \langle v^2 \rangle = \frac{m_e c^2 \sigma^2}{\lambda^2} = 27 \pm 2\,\mathrm{meV}\,. \tag{5.6}$$

At 2.9 keV implantation, the Ps emission energy should likely approach the ground state energy given by the size of the pores (section 2.5.1), though would not be expected to fall below the thermal energy of the sample, i.e. 25 meV (ambient).

In comparison to other studies, this measurement of the mean energy of the positronium distribution, is significantly lower than suchlike measured in the direction perpendicular to an F-127 SiO_2 sample (sim. to this work), by means of TOF (48 ± 5 meV, Crivelli *et al.* [2010]). It is also found to be somewhat lower than similar measurements of the Doppler width (42 ± 3 meV, Cassidy *et al.* [2010b])

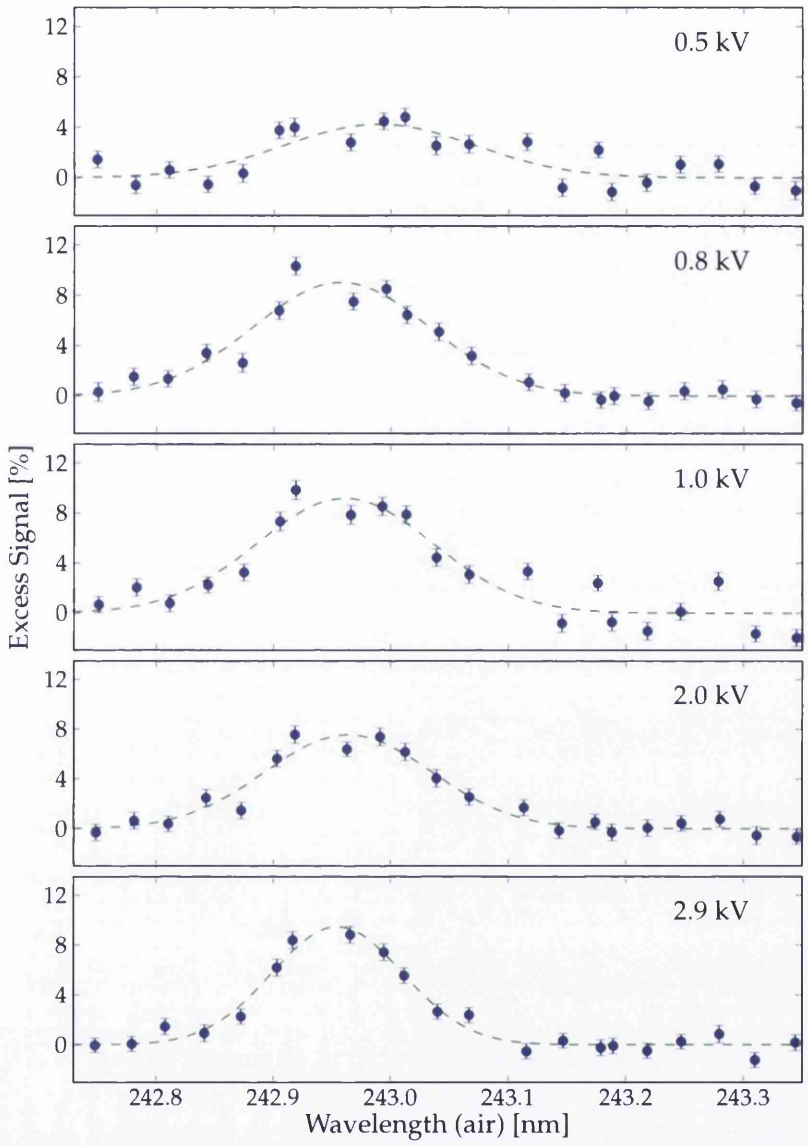

Figure 5.5: The excess SSPALS signal during the excitation window (see text) for various tunings of the UV laser wavelength and target bias. At each point the data has been normalised against the total SSPALS signal and scaled to represent a percentage increase over the background (laser off-resonant). The error-bars indicate the standard error from 300 repeats. The dashed line represents a Gaussian fit to the points.

for positronium created with a CTAC1-TEOS SiO_2 sample. However, we should expect cooler positrons than the latter group, due to the smaller pore size of their sample. Indeed, noting that Crivelli *et al.* [2010] found positronium atoms from CTAC1-TEOS samples to be a factor of 1.52 more energetic than those from F-127, and assuming the same factor applies for measurements parallel to such samples, brings this measurement in-line with Cassidy *et al.* [2010b]. This relationship is interesting to note, but it's not obvious that the assumption has any physical basis. Moreover, there are many unknowns with regard to the angular and energy distributions of the emitted Ps, and accordingly care should be taken in drawing conclusions from this result. It would be worthwhile to extend these methods to a spatially well-defined beam (i.e. focussed and with an accurately known, adjustable position) to try and elucidate the situation, or additionally to perform time-of-flight measurements.

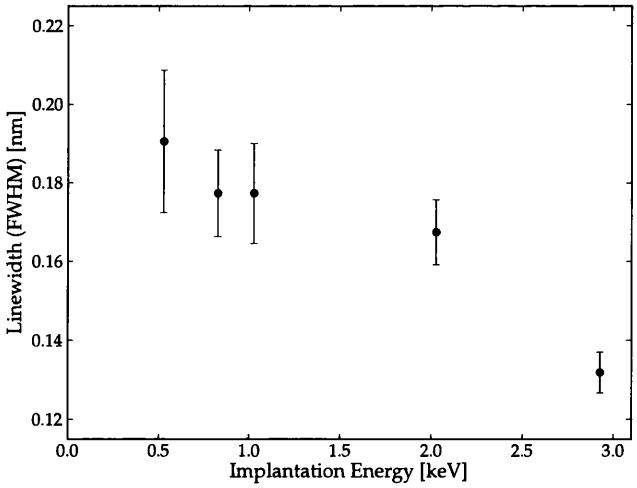

Figure 5.6: The Doppler broadened linewidth (FWHM) of the Lyman-α interval of free ortho-positronium. The values were determined by fitting a Gaussian function to SSPALS measurements of the magnetic quenching excess, across a range of UV laser wavelengths, for a selection of target biases (e.g. figure 5.5).

5.4 Further Studies

5.4.1 Single-Pass Magnetic Quenching

The intensity of light needed to saturate the Lyman-α interval is related to the wavelength (λ_0) required to pump the transition, and the radiative lifetime of the excited state (τ_{2P}). A simple steady state model describes the relationship as,

$$I_{sat} = \frac{\pi hc}{3\lambda_0^3 \tau_{2P}} \sim 0.5\,[\mathrm{W/cm^2}]\,. \tag{5.7}$$

Or equivalently, for a beam diameter of 6 mm to saturate one natural linewidth (50 MHz) of the transition, requires approximately 1 nJ in an 8 ns pulse. Taking into account that the energy is distributed across the broad laser linewidth (174 GHz), suggests our beam would require just 3.5 µJ to saturate the transition, as compared to its estimated pulse energy of 1 mJ. Monte-Carlo simulations and experimental results [Cassidy *et al.*, 2010b; Ziock *et al.*, 1990b] find that an intensity in excess of 200 $\mu\mathrm{J\,cm^{-2}}$ is actually needed to achieve saturation, nonetheless implying that the laser described in chapter 3 is more than sufficient.

Despite such, in designing the initial experiments we chose to utilise a double-pass of the UV beam, in the hope of strengthening any quenching signal. Even when in saturation, the small delay (2 ns) in the reflected path would potentially increase the likelihood of excitation, by lengthening the laser pulse and thus interaction time. Furthermore, if slightly detuned from the Lyman-α frequency, the reflected beam would be resonant with the atoms Doppler shifted in the opposite direction to those resonant with the first pass, increasing the fraction which are addressed and improving the likelihood of detecting magnetic quenching.

A comparison of single and double pass magnetic quenching experiments is shown in figure 5.7. The results are consistent with the expectation of exceeding saturation intensity, with only a marginal enhancement for the double pass case, which is not significant in view of the statistical uncertainties.

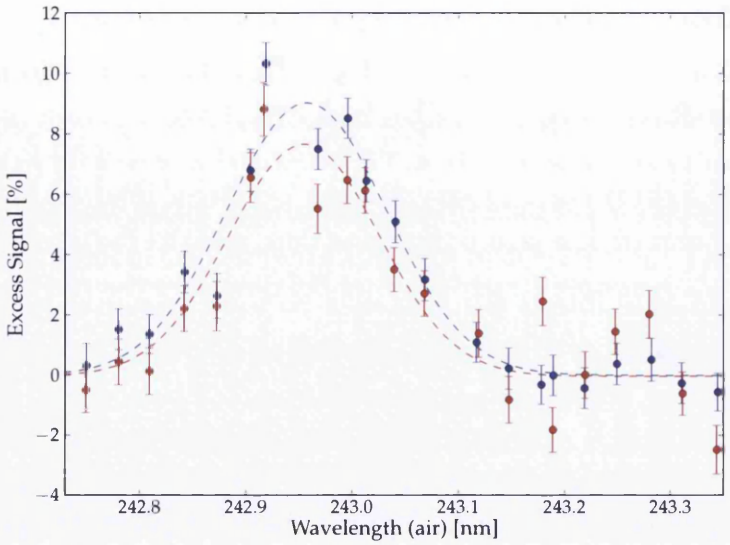

Figure 5.7: The excess SSPALS signal for various tunings of a single (red) and double (blue) pass of a UV laser through a cloud of positronium atoms. The error-bars indicate the standard error from 300 repeats. The dashed lines represent Gaussian fits to the points. The Ps conversion target was biased at −0.8 keV.

5.4.2 Resonant Ionisation Spectroscopy

The objective of these works is to progress towards laser excitation of positronium into Rydberg states. A technically similar - albeit simpler - experiment is that of two-photon resonant ionisation spectroscopy (RIS); accordingly RIS has been attempted as a precursor to pursuing Rydberg states. The study involves exciting the Ps Lyman-α transition with the resonantly tuned UV laser (as above), followed by excitation from the 2P state into the ionisation continuum with a green laser (section 5.2.2).

To suppress the magnetic quenching signal exploited in the previous experiments, the permanent magnet was removed from behind the target. If successful ionisation events are achieved, the expected signal would be an increase in annihilations when the lasers fire, due to dissociated positrons being accelerated into the target (measurable with SSPALS). In absence of the green laser, the UV beam alone

should result in a very slight depletion in signal, as a consequence of the increase in lifetime against self-annihilation of the excited state (in the lower magnetic field).

Table 5.1 shows the "excess" signal of a preliminary attempt at such an experiment, for the permutations of the green and UV (242.96 nm, air) lasers applied or otherwise. The data has been analysed in a manner similar to the Doppler measurements (section 5.3), however the background in this case was taken to be when neither laser was fired.

Table 5.1: The excess annihilation signal (g) [%] for different combinations of lasers applied in a RIS study of positronium. The uncertainty represents the standard error from 300 repeats.

		Ultraviolet	
		Off	On
Green	Off		-2.01 ± 1.46
	On	1.19 ± 1.47	3.13 ± 1.50

The results are qualitatively consistent with ionisation, but are unfortunately statistically indistinguishable from the null-hypothesis. The photons in the green (532 nm) beam exceed the energy required to achieve single-photon ionisation from the 2P state (resonant at 729 nm), yet do not have a very large cross-section for doing so. Increasing the power of this laser and/ or enhancing the detection efficiency would greatly improve the chances of observing ionisation events - see chapter 6.

Chapter 6

Concluding Remarks

6.1 Summary

We have developed and advanced techniques for the manipulation of positrons accumulated in a two-stage buffer gas accumulator. A simple and versatile method for reproducible, radial displacement of trapped positrons is outlined, with a number of potential applications - most notably that of multi-cell trapping.

This method of control has been employed as a diagnostic of the anharmonic (non-ideal) characteristics of the trap, and such findings are used to extend an ideal model for compression with a rotating dipole electric field, to explain a number of phenomena pertaining to accumulation and compression in a non-ideal trap. Furthermore, a new scheme for compressing particles with a rotating field swept downward in frequency was devised which exploits the trap anharmonicity. For certain conditions this "chirp" was shown to increase the cloud density by a factor of six, although - in these preliminary tests - no improvement was made to the absolute density attainable.

In pursuit of the most dense positron clouds a longer well-shape (Penning-Malmberg electric potential) was employed for accumulation with compression, mitigating a loss of resonance with the rotating field due to the build up of space-

charge and subsequent distortions to the well. These positron clouds have been implanted into a porous silica sample to form positronium, which is emitted to vacuum with an efficiency estimated at $\sim$ 30 %. Such formation is evidenced by lifetime measurements (SSPALS) using a fast gamma-ray detector assembled specifically for this purpose.

In parallel to the work with positrons, a pulsed UV laser has been developed with an especially broad linewidth, which has been designed for optical pumping of the $1S - 2P$ interval of positronium. Excitation events are achieved by probing positronium clouds with the laser and detecting deviations to the Ps decay as measured with SSPALS; the deviations are attributed to magnetic quenching to short lived states which is enhanced by excitation.

Using the above technique the expected Doppler broadened width of the interval was measured. Cooling in the silica target of the positronium atoms was subsequently inferred, from linewidth measurements at different depths of positron implantation. A comparison between single and double pass laser measurements indicates the laser is saturating the positronium population, in agreement with expectation. Additionally, a preliminary attempt at resonant ionisation of positronium was made using a second laser (visible, 532 nm). The results of this experiment are encouraging although not yet statistically significant - further work being required.

6.2 Outlook

6.2.1 Accumulation

The main difficulty with optimising the accumulator is the enormity of the parameter space for the various settings (electrode biases, gas-pressures, RW settings, magnetic fields, etc.). This is even further enlarged when dynamic schemes are considered, e.g. RW chirping. It is easy to imagine then that the the present configuration may be significantly improved upon, in terms of the positron densities that

can be achieved, perhaps through a radically different trapping scheme. Indeed, recent Monte-Carlo simulations by Petrović and co-workers (Institute of Physics, Belgrade, Serbia) [unpublished] have suggested that capture efficiencies approaching 100 % are attainable, with tetrafluoromethane (CF_4) as a buffer gas in place of molecular nitrogen.

If significant further gains are made, the difficulty of dealing with space-charge is likely to become more critical, with regard to keeping the RW optimally tuned. As discussed in section 4.3.1, longer flatter wells are more resistant to this phenomenon, however an active approach might be taken in tuning the RW frequency throughout the accumulation, in order to track changes in the motional frequencies that are caused by the build-up of space-charge. This might be achieved with trial and error, or better yet the results of simulations. An inherent difficulty for such would be in adapting to variations in the moderator strength/ trapping efficiency. It would be significantly more robust to instead feedback electric signals induced by the oscillating charges (e.g. using nearby pickup electrodes), to track any shifts.

Another avenue for investigation of the RW technique would be to try and reduce the anharmonic components of the trapping potential, to better replicate the ideal model proposed by Isaac *et al.* [2011]. A system of two, six-segment electrodes that are separated and buttressed with compensation electrodes, has already been designed and assembled for this purpose - although it is yet to be tested. Having demonstrated in these works some applications of the non-ideal potential, it is not clear that there will be any practical benefit to "improving" the fields, besides providing a more faithful test of the theory.

Increasing the density and number of positrons embedded into the silica will help to improve the signal-to-noise of the spectroscopy studies (see below). The most dramatic increase might be made by an additional third stage trap, with high quality fields and good vacuum conditions, which could be dynamically loaded from the two-stage to achieve a plasma with roughly 10^8 positrons, that would be compressible by the strong-drive RW technique [Danielson and Surko, 2005].

Other improvements might be made more simply by pursuing particle bunch-

ing, to time compress the positron clouds and thereby better match the Ps plume to the laser pulse (8 ns). There are a number of possible ways to achieve this, e.g. by means of an assembly of cylindrical electrodes, through which the positrons pass, and to which are applied some suitable voltage ramps [Cassidy *et al.*, 2006a].

6.2.2 Spectroscopy

A worthwhile upgrade to the magnetic quenching experiment would be to find some means of triggering the laser that improves upon the 15 ns jitter observed across repeat measurements with the present configuration. Reducing this to better than 1 ns is well within the scope of available technologies.

It should be noted that the data sets for Doppler width scans were taken on separate days and that the temperature of the lab is not regulated, therefore each approximately 6 h acquisition period may have been subject to different environmental drifts. The light-output of the PWO crystal is known to change with temperature (approx. 2 % per °C at room temperature [Qu *et al.*, 2002]), therefore we should expect some variation in detection efficiency. Naïvely, this should be taken into account by the normalisation of the data, but might be avoided altogether by thermally stabilising the crystal.

The moderator efficiency and cryo-pump speeds (thus trapping rate and lifetime) are also known to drift over the course of days, ultimately changing the amount of Ps formed with each shot. This should, in principle, be accounted for with normalisation, but is nonetheless undesirable. Avoiding such drifts is non-trivial, but could perhaps be corrected for by adjusting the accumulation time against some reference of the moderator strength, to achieve consistent results. The moderator stability might be enhanced by improving the vacuum conditions in the source chamber, to prevent the build-up of detrimental containments. Additionally, to better track changes in pumping speed, the cooling-gas pressure could be regulated to PG-6 in cross II rather than to PG-11 in the cooling-gas line. Alternatively, cryopump 1 could be swapped for a turbo pump for better consistency,

at the expense of pumping speed.

It is also worth considering beam walk of the UV laser, caused by the path change through the nonlinear crystals as these are rotated in accordance with the desired wavelength. This is corrected for in the OPO but not in the second SFG; though such could be implemented with relative ease. Observations show that beam walk can move the laser by up to 2 mm at cross IV, altering the physical overlap with the positronium plume and potentially affecting the excitation signal. However, experiments were repeated after deliberate movement of the beam by a similar degree, and no significant difference was observed. Nonetheless, small changes in the e^+/ laser alignment could increase sensitivity to beam walk.

A simple measurement yet to be attempted with this apparatus, would be to accurately determine the pulse energy required to saturate the Ps Lyman-α transition. As we presently suspect we are well past saturation, this could be performed by simply repeating the quenching measurements with a variably attenuated UV beam, e.g. by means of a half-wave plate (to rotate the beam polarisation) and polarising beam splitter.

It would also be eminently interesting to use the quenching technique to investigate the Doppler width of positronium emitted from different samples, and furthermore from samples which are held at different temperatures. The latter in particular would require substantial hardware changes, but is merited by the significant interest in the Ps formation properties of porous films at low temperatures, by those pursuing ultra-cold positronium - e.g. for efficient antihydrogen production or gravitational measurements with Ps.

Success might be had with resonant ionisation studies of Ps (section 5.4.2) by use of a second Nd:YAG - conveniently, one is operational and already installed in the positron lab! This laser would need to be synchronised with the UV laser, and could provide up to 200 mJ pulses of its second harmonic (532 nm), i.e. much more than should be required to achieve a strong RIS signal. Furthermore, this would be excellent preparation for developing an infra-red beam (most likely pumped by this YAG), for exciting 2P positronium atoms to Rydberg states.

6.2.3 Detection

A significant improvement to the statistics of the spectroscopy experiments might be made by use of additional detectors for SSPALS, thereby increasing the solid angle coverage. The poor light yield of the PWO is beneficial in the sense that it does not saturate the PMT, however a fast plastic scintillator would have better timing characteristics (faster decay and less afterglow), and although weak gamma absorbers (low density) such plastics can be made in large pieces which are relatively inexpensive. Regardless of the materials used, a thorough characterisation study of the detectors would be useful for improving on the SSPALS model described in section 5.1.1.

The experiment would also significantly benefit from a faster, higher resolution oscilloscope for recording the PMT signal(s). The 300 MHz bandwidth of the *National Instruments* PCI-5152 used in this work (section A.2.3), is one of the biggest limiting factors to the timing resolution. Furthermore, as the entire range of the signal must be captured for normalisation, the 8-bit voltage resolution of this card causes significant digitisation to the traces in the region of interest; this is one of the reasons that so many repeats are required.

To perform precision spectroscopy with this set-up, it will actually be beneficial to use much lower intensity lasers, to avoid power broadening. It is unlikely that the consequently weak signals will be detectable by SSPALS, and therefore a more sensitive scheme should be developed.

A preliminary detector concept for precision Ps spectroscopy studies is illustrated in figure 6.1. Positrons are accumulated and embedded into a silica sample that is orientated to emit Ps atoms across the magnetic field lines (along which the positrons propagate). Laser excitation and photo-ionisation/ field ionisation of the Ps will then produce positrons that will be guided along a path offset from the original positron cloud trajectory, to impinge upon a Channeltron® electron multiplier (CEM). Such a device would have near unity quantum detection efficiency for positrons, enabling detection of very few ionisation events.

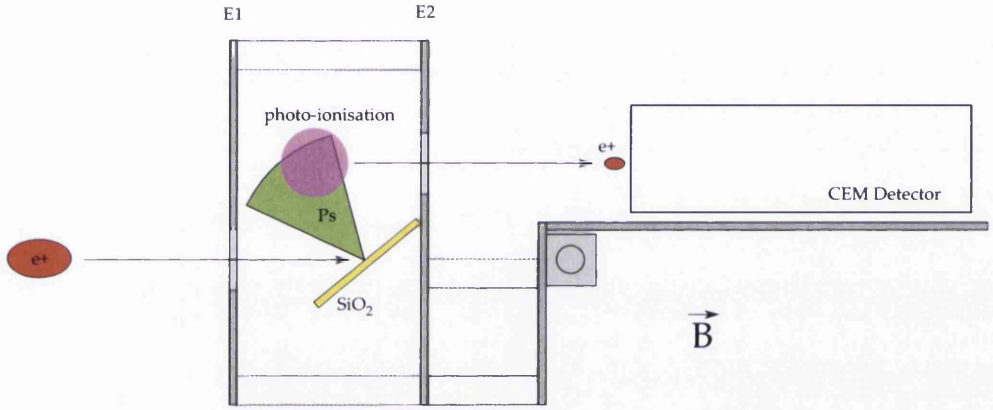

Figure 6.1: Schematic illustration of a proposed detection scheme for photo-ionisation/ field ionisation of positronium atoms - see text.

Computers are useless. They can only give you answers.

Pablo Picasso [attributed]

Appendix A

Experiment Control

Virtually all modern experiments are controlled using a combination of hardware and software, ideally configured to circumvent some of the multifarious disadvantages of the human experimentalist. The much increased capacity and reduced cost of digital memory facilitates continuous monitoring of experimental conditions and the recording of vast sets of high resolution experimental data. This begets the difficulty - albeit enviable - of extracting useful statistics from potentially colossal data sets. An extreme example of such is the petabyte of data generated every second by the LHC, which is filtered and distributed around the world by the CERN computing grid.

The following outlines some of the steps taken to efficiently monitor and control the Swansea positron beamline (see chapter 2), and to establish a scalable system for effectively managing the relatively modest volume of data that it produces.

A.1 System Monitoring

With every experimental system it is advisable to monitor and record any variable conditions which may influence the results. Timestamps associated with experimental measurements can then be cross referenced against such records, in order

to better identify correlation between measurements, experiment parameters and system variables.

In the case of the positron beamline, it is essential to monitor the vacuum conditions (see section 2.1.1), as these influence the annihilation rate, trapping efficiency and particle cooling; these are recorded from the twin MaxiGauge™s using a Labview™ virtual instrument (vi). The temperature measured at the source mount by the *Lakeshore* Model 331 (section 2.2) is similarly recorded, in addition to readings from various sensors that monitor the cooling water temperature, lab temperature and lab humidity. The voltage and current output by the power supply for solenoid-2 (table 2.3) is also monitored and recorded.

The above measurements are written to file, and furthermore a backup is transferred to a MySQL database running on a separate server; usefully, this also facilitates remote live monitoring with a simple web based graphical interface.

A.2 Control and Data Logging

A.2.1 Sequencer

The control of the voltages that supply the accumulator electrodes is provided by an FPGA and two Analogue Output devices - see section 2.3.2. Additionally the FPGA produces digital triggers for extra system hardware (e.g. pulser, laser) and measurement devices (e.g. camera, digitiser - see section A.2.3). Furthermore, a number of steerable experimental parameters - termed VARs - may be configured programmatically prior to running the FPGA. Systems which can be controlled in this manner include: RW frequency and amplitude; buffer and cooling gas PID set points; solenoid-2 current supply; source mount temperature PID set point; laser system motor controls for the OPO and SFG (section 3.3).

The desired timing steps, AO levels, digital triggers etc. are encoded in human readable form and appended with a simple text based VARs system: VAR=VALUE. These are stored as an ASCII text file, .sq5, the format of which is as given in

figure A.1. Each line represents a time step for the FPGA, and consists of six tab separated elements: the first gives the duration of the step; the second is a Boolean (0,1) option for whether this is an AO step, i.e. 'trigger AO device?'; the third, fourth and fifth are comma delimited arrays of the digital inputs (0,1) (not used in these studies), digital outputs (0,1) and analogue outputs ($\pm$140.0) respectively; the final element allows for a description of the step process. The timing resolution of each step is 12.5 ns with a minimum step time of 37.5 ns, which increases to 3 µs for AO steps.

```
START:
<step 1 duration> <AO?><DI ×10><DO ×30><AO ×16><description>
<step 2 ...
 ⋮
<step n ...
#VAR_1=VALUE_1,VAR_2=VALUE_2, ..., VAR_n=VALUE_n
:STOP
```

Figure A.1: The format of .sq5 sequence files.

The process of executing an .sq5 file was originally developed by C. A. Isaac, and the system used in these studies is modelled upon the integrated sequencer described in his postgraduate thesis [Isaac, 2010]. A Labview™ virtual instrument, 'sequencer.vi,' co-ordinates the sequence execution, and begins by reading the .sq5 file and extracting the VARs. The VARs are served to global variables with status: *pending*. Specialised vi's are written to listen for specific VAR keys, to act upon pending values (write hardware settings) and to update the VAR status to: *set*. The 'VARs Network Server.vi' listens for user selected VARs and translates them into 'Datasockets' which are accessible by the local network; this enables VARs to be relayed to a PC with control of specific hardware, e.g. the accumulator solenoid power supply. This modular approach allows for great flexibility, as introducing new VARs requires no update to the core 'sequencer.vi'.

The sequencer waits for each requested VAR to be answered (set), then distils a table of AO steps from the sequence lines and loads it into each AO device. Finally the sequence lines are translated into ML (medium-level) code, looped using the requested number of repeats, and loaded into the FPGA (the driver for which was written by W. Bertsche - ALPHA collaboration), initiating the sequence to run. The overriding concept of running a sequence is illustrated as a flow diagram in figure A.2.

The sequencer and VAR virtual instruments are collected together in a Labview project file, along with additional vi's, including: hardware drivers; those for data capture (section A.2.3); a graphical user interface for sequence writing; another for production of sequence batches (section A.2.2).

Whenever a single sequence or list is run, the sequencer generates a unique run_ID number (based on a timestamp) and records the sequence name(s) and time ran in an .olg, text based log file and further to a MySQL database - facilitating live remote monitoring, much as with the environment data (section A.1). Additional information recorded includes: an iterating sequence_ID; the number of repeats; any error codes encountered; (if applicable) the variable values used by 'Modder.vi' (see below) for each specific sequence. This information is utilised later for data processing (section A.3).

A.2.2 Batch Sequences

Batch sequence production is achieved with 'Modder.vi,' the purpose of which is to take a template sequence file and to replace a number of features (e.g. step duration, AO, VARs) with all possible permutations of the values given in a list of arrays. The result is a batch of sequences and an .lst5 file - essentially instructions to the sequencer to execute each sequence in turn. This has powerful applications in measuring large parameter spaces, for e.g. many combinations of the RW frequency and amplitude.

Furthermore, 'Modder.vi' has been programmed with the facility to randomise

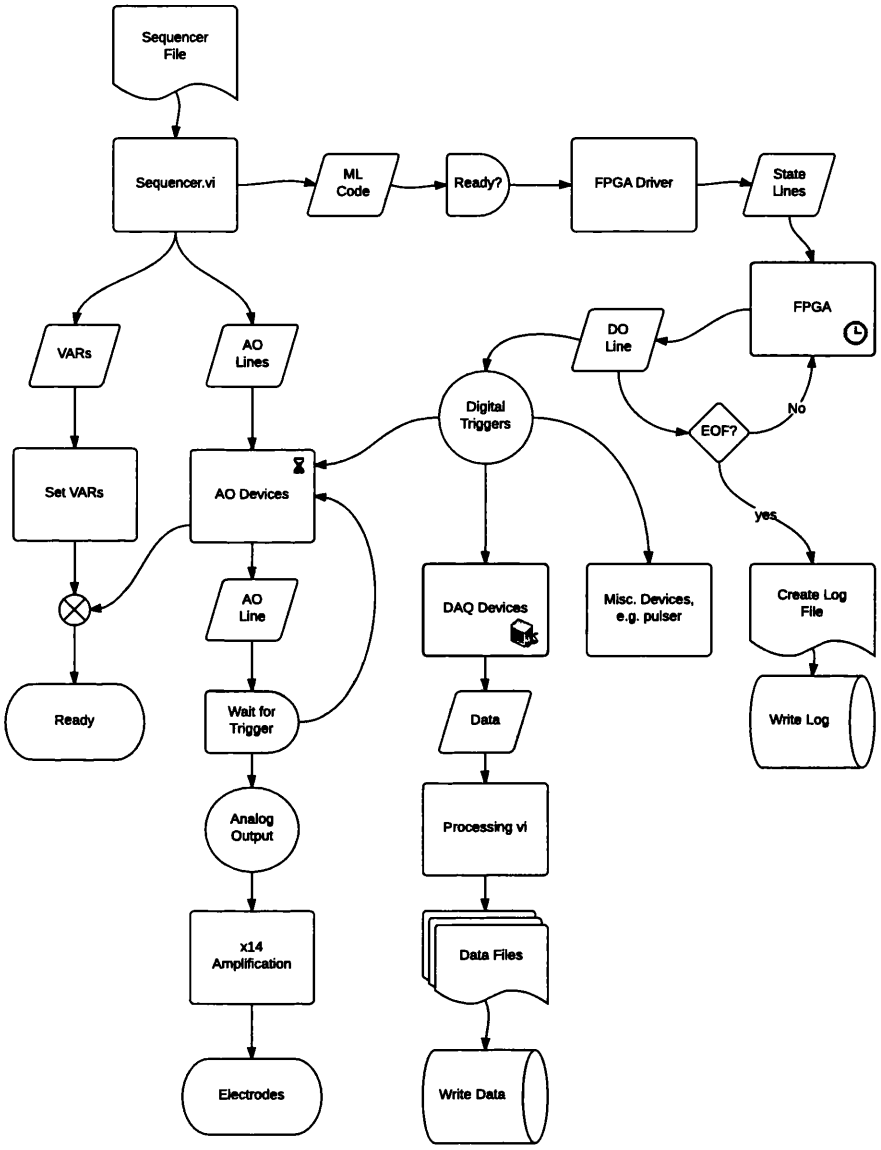

Figure A.2: Flow diagram depicting the execution of a sequencer file that initialises VARs, generates analogue and digital outputs, and triggers data acquisition.

the order of the list file. This is used to suppress the influence of drifting experimental conditions e.g. moderator degradation, which could impart a misleading systematic aberration onto sequentially run data - unlikely in the randomised case.

A.2.3 Data Capture

The flexibility of the sequencer and control system has allowed for integration of experimental runs with numerous data acquisition devices. Those which have been predominately employed in these studies are outlined in the following.

Digitiser

The digitiser used for the majority of data capture is a *National Instruments* PCI-5152. This card has a 300 MHz bandwidth and can record voltage readings at a maximum sample rate of 2 GS /s across two separate channels, with 8-bit resolution in a 100 mV to 10 V range. Hardware triggering is used to synchronise data capture with the experimental sequences by means of the FPGA.

The digitiser card is configured using Labview,™ which also extracts and saves the data into a file structure based upon the timestamp run_ID and iterating sequence_ID (see above), with data from subsequent repeats appended to the same file. A simple script written in Python can then be used to extract and display traces using these numbers as unique identifiers, with the added facility to plot averaged data from multiple repeats and/or to fit the data with various functions. An example trace from a CsI/ diode detector of a positron cloud annihilation signal is given in figure A.3.

Camera

The luminescence from the MCP/ phosphor screen assembly (section 2.6.1) is imaged using a *Hamamatsu* Orca-R2, 1.3 megapixel CCD camera with a 16 bit dual A/D converter. The camera is configured using Labview,™ which also extracts and

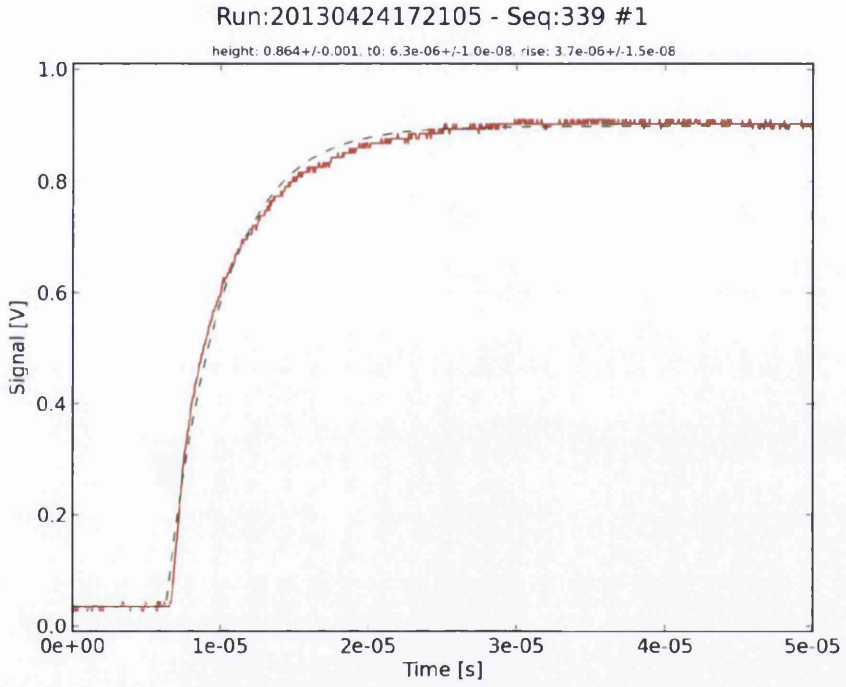

Figure A.3: Example digitiser trace data (red) extracted and plotted using a Python/ matplotlib script (repeat #1). The data has been fitted with a capacitive charging curve (green, dashed), to ascertain the height of the CsI/ diode signal.

saves the data into a file structure consistent with the digitiser data acquisition (see above). Synchronisation between the camera acquisition and sequencer is achieved by means of a hardware trigger connected to a DO of the FPGA.

The systematic structure of the data storage allows images to be reliably retrieved with a Python script using the run_ID and sequence_ID as unique identifiers. The same script has added features for subtracting an empty image (removing the background caused by a temperature gradient across the CCD), and for fitting a 2D Gaussian function. See figure A.4 for an example.

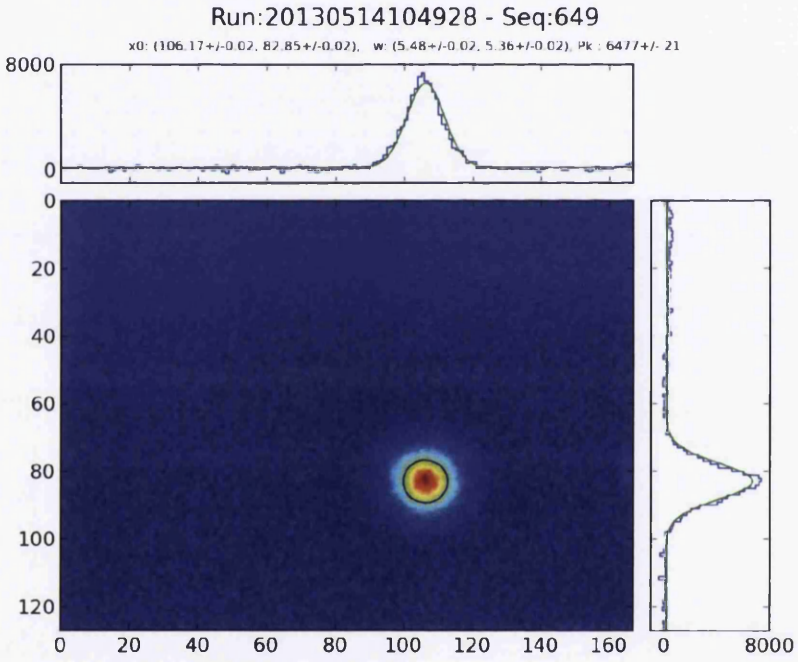

Figure A.4: Example camera image extracted and plotted with background subtraction using a Python/ matplotlib script (*N.B.* data averaged from 20 repeats). Slices through the data at the point of maximum intensity (arb. units) are shown for x and y as sub-plots alongside and above, respectively. To characterise the image the data has been fitted with a 2D Gaussian, (green, sub-plots). The dimensions are given in units of binned data points (8 × 8 pixels), where the width of each bin represents 0.28 mm at the phosphor screen.

A.3 Data Processing

As described in section A.2, the sequencer and data acquisition yield a comprehensive quagmire of logs and data files - extra manipulation is needed to refine these into something more intelligible. Not-to-mention that large data sets may be amassed often and in a relatively short space of time (hours), due to the rapid cycle operation and stability of the positron accumulator. These data are distributed across the local area network, such that several users may have simultaneous access. Accordingly, a number of Python scripts have been written for rapid batch analysis of the data across the network, intrinsically designed to be easily configured for operation on a variety of systems, and managed from a central server running the version control software, SVN.

The Python scripts perform basic data manipulation tasks, such as the averaging of repeat measurements and determination of the basic statistical 'features,' such as range and standard deviation. Furthermore, the fitting modules used to analyse individual traces and images may be called upon to perform batch fitting operations, returning yet more data 'features' in the form of fit parameters. Additionally, the timestamps from the log file may be used to map data against the system monitoring records, e.g. vacuum pressures.

The wealth of information which can be accrued in executing these scripts is stored as tables in *_info.csv files. This forms a crude database - compatible with commercial spreadsheet software - which can be searched based on any aspect of the analysis features (or Modder.vi variables) by means of yet another Python script, or likewise filtered and exported using an unlimited number of rules applied to any number of such features. Finally, data can be selected for display in a variety of informative plot formats, with added functionality for fitting a number of commonly used functions to such data, e.g. accumulation curves (figure 2.10) and energy spectrum curves (figure 2.18).

The upshot of the above is that shortly after running a number of sequences it's quick and easy to analyse and scrutinize the results, for even very large data sets.

Author Publications

2013

Amole, C., Ashkezari, M.D., Baquero-Ruiz, M., Bertsche, W., Butler, E., Capra, A., Cesar, C.L., Charlton, M., Deller, A., Eriksson, S., Fajans, J., Friesen, T., Fujiwara, M.C., Gill, D.R., Gutierrez, A., Hangst, J.S., Hardy, W.N., Hayden, M.E., Isaac, C.A., Jonsell, S., Kurchaninov, L., Little, A., Madsen, N., McKenna, J.T.K., Menary, S., Napoli, S.C., Olchanski, K., Olin, A., Pusa, P., Rasmussen, C.O.., Robicheaux, F., Sarid, E., Shields, C.R., Silveira, D.M., So, C., Stracka, S., Thompson, R.I., van der Werf, D.P., Wurtele, J.S., Zhmoginov, A. and Friedland, L. (2013). Experimental and computational study of the injection of antiprotons into a positron plasma for antihydrogen production. *Physics of Plasmas*, 20(4):043510. doi:10.1063/1.4801067

Mortensen, T., Deller, A., Isaac, C.A., van der Werf, D.P., Charlton, M. and Machacek, J.R. (2013). Manipulation of the magnetron orbit of a positron cloud in a penning trap. *Physics of Plasmas*, 20(1):012124. doi:10.1063/1.4789880

2012

Andresen, G., Ashkezari, M., Bertsche, W., Bowe, P., Butler, E., Cesar, C., Chapman, S., Charlton, M., Deller, A., Eriksson, S., Fajans, J., Friesen, T., Fujiwara, M., Gill, D., Gutierrez, A., Hangst, J., Hardy, W., Hayden, M., Hayano, R., Humphries, A., Hydomako, R., Jonsell, S., Jørgensen, L., Kurchaninov, L., Madsen, N., Menary, S., Nolan, P., Olchanski, K., Olin, A., Povilus, A., Pusa, P., Sarid, E., el Nasr, S.S., Silveira, D., So, C., Storey, J., Thompson, R., van der Werf, D. and Yamazaki, Y. (2012). Antihydrogen annihilation reconstruction with the ALPHA silicon detector. *Nuclear Instruments and Methods in Physics Research Section A*, 684:73 – 81. doi:http://dx.doi.org/10.1016/j.nima.2012.04.082

Amole, C., Ashkezari, M.D., Baquero-Ruiz, M., Bertsche, W., Bowe, P.D., Butler, E., Capra, A., Cesar, C.L., Charlton, M., Deller, A., Donnan, P.H., Eriksson, S., Fajans, J., Friesen, T., Fujiwara, M.C., Gill, D.R., Gutierrez, A., Hangst, J.S., Hardy, W.N., Hayden, M.E., Humphries, A.J., Isaac, C.A., Jonsell, S., Kurchaninov, L., Little, A., Madsen, N., McKenna, J.T.K., Menary, S., Napoli, S.C., Nolan, P., Olchanski, K., Olin, A., Pusa, P., Rasmussen, C.Ø., Robicheaux, F., Sarid, E., Shields, C.R., Silveira, D.M., Stracka, S., So, C., Thompson, R.I., van der Werf, D.P. and Wurtele, J.S. (2012). Resonant quantum transitions in trapped antihydrogen atoms. *Nature*, 483(7390):439–443. doi:10.1038/nature10942

Amole, C., Andresen, G.B., Ashkezari, M.D., Baquero-Ruiz, M., Bertsche, W., Butler, E., Cesar, C.L., Chapman, S., Charlton, M., Deller, A., Eriksson, S., Fajans, J., Friesen, T., Fujiwara, M.C., Gill, D.R., Gutierrez, A., Hangst, J.S., Hardy, W.N., Hayden, M.E., Humphries, A.J., Hydomako, R., Kurchaninov, L., Jonsell, S., Madsen, N., Menary, S., Nolan, P., Olchanski, K., Olin, A., Povilus, A., Pusa, P., Robicheaux, F., Sarid, E., Silveira, D.M., So, C., Storey, J.W., Thompson, R.I., van der Werf, D.P. and Wurtele, J.S. (2012). Discriminating between antihydrogen and mirror-trapped antiprotons in a minimum-B trap. *New Journal of Physics*, 14(1):015010

2011

Andresen, G.B., Ashkezari, M.D., Baquero-Ruiz, M., Bertsche, W., Bowe, P.D., Butler, E., Cesar, C., Chapman, S., Charlton, M., Deller, A., Eriksson, S., Fajans, J., Friesen, T., Fujiwara, M., Gill, D., Gutierrez, A., Hangst, J., Hardy, W., Hayden, M., Humphries, A., Hydomako, R., Jonsell, S., Madsen, N., Menary, S., Nolan, P., Olin, A., Povilus, A., Pusa, P., Robicheaux, F., Sarid, E., Silveira, D., So, C., Storey, J., Thompson, R., van der Werf, D.P., Wurtele, J. and Yamazaki, Y. (2011). Centrifugal separation and equilibration dynamics in an electron-antiproton plasma. *Physical Review Letters*, 106(14):1–5. doi:10.1103/PhysRevLett.106.145001

Andresen, G.B., Ashkezari, M.D., Baquero-Ruiz, M., Bertsche, W., Bowe, P.D., Butler, E., Cesar, C.L., Charlton, M., Deller, A., Eriksson, S., Fajans, J., Friesen, T., Fujiwara, M.C., Gill, D.R., Gutierrez, A., Hangst, J.S., Hardy, W.N., Hayano, R.S., Hayden, M.E., Humphries, A.J., Hydomako, R., Jonsell, S., Kemp, S.L., Kurchaninov, L., Madsen, N., Menary, S., Nolan, P., Olchanski, K., Olin, A., Pusa, P., Rasmussen, C.O., Robicheaux, F., Sarid, E., Silveira, D.M., So, C., Storey, J.W., Thompson, R.I., van der Werf, D.P., Wurtele, J.S. and Yamazaki, Y. (2011). Confinement of antihydrogen for 1,000 seconds. *Nature Physics*, 7(7):558–564. doi:10.1038/nphys2025

2010

Andresen, G.B., Ashkezari, M.D., Baquero-Ruiz, M., Bertsche, W., Bowe, P.D., Butler, E., Cesar, C.L., Chapman, S., Charlton, M., Deller, A., Eriksson, S., Fajans, J., Friesen, T., Fujiwara, M.C., Gill, D.R., Gutierrez, A., Hangst, J.S., Hardy, W.N., Hayden, M.E., Humphries, A.J., Hydomako, R., Jenkins, M.J., Jonsell, S., Jørgensen, L.V., Kurchaninov, L., Madsen, N., Menary, S., Nolan, P., Olchanski, K., Olin, A., Povilus, A., Pusa, P., Robicheaux, F., Sarid, E., Seif el Nasr, S., Silveira, D.M., So, C., Storey, J.W., Thompson, R.I., van der Werf, D.P., Wurtele, J.S. and Yamazaki, Y. (2010). Trapped antihydrogen. *Nature*, 468(7324):673–676. doi:10.1038/nature09610

Bibliography

Amole, C., Ashkezari, M.D., Baquero-Ruiz, M., Bertsche, W., Bowe, P.D., Butler, E., Capra, A., Cesar, C.L., Charlton, M., Deller, A., Donnan, P.H., Eriksson, S., Fajans, J., Friesen, T., Fujiwara, M.C., Gill, D.R., Gutierrez, A., Hangst, J.S., Hardy, W.N., Hayden, M.E., Humphries, A.J., Isaac, C.A., Jonsell, S., Kurchaninov, L., Little, A., Madsen, N., McKenna, J.T.K., Menary, S., Napoli, S.C., Nolan, P., Olchanski, K., Olin, A., Pusa, P., Rasmussen, C.Ø., Robicheaux, F., Sarid, E., Shields, C.R., Silveira, D.M., Stracka, S., So, C., Thompson, R.I., van der Werf, D.P. and Wurtele, J.S. (2012). Resonant quantum transitions in trapped antihydrogen atoms. *Nature*, 483(7390):439–443. doi:10.1038/nature10942

Amoretti, M., Amsler, C., Bonomi, G., Bouchta, A., Bowe, P., Carraro, C., Cesar, C.L., Charlton, M., Collier, M.J.T., Doser, M., Filippini, V., Fine, K.S., Fontana, A., Fujiwara, M.C., Funakoshi, R., Genova, P., Hangst, J.S., Hayano, R.S., Holzscheiter, M.H., Jørgensen, L.V., Lagomarsino, V., Landua, R., Lindelöf, D., Rizzini, E.L., Macrì, M., Madsen, N., Manuzio, G., Marchesotti, M., Montagna, P., Pruys, H., Regenfus, C., Riedler, P., Rochet, J., Rotondi, A., Rouleau, G., Testera, G., Variola, A., Watson, T.L. and van der Werf, D.P. (2002). Production and detection of cold antihydrogen atoms. *Nature*, 419(6909):456–459. doi:10.1038/nature01096

Anderegg, F., Hollmann, E.M. and Driscoll, C.F. (1998). Rotating field confinement of pure electron plasmas using trivelpiece-gould modes. *Physical Review Letters*, 81:4875–4878. doi:10.1103/PhysRevLett.81.4875

Anderson, C.D. (1933). The positive electron. *Physical Review*, 43:491–494. doi:10.1103/PhysRev.43.491

Andresen, G.B., Ashkezari, M.D., Baquero-Ruiz, M., Bertsche, W., Bowe, P.D., Butler, E., Cesar, C.L., Chapman, S., Charlton, M., Deller, A., Eriksson, S., Fajans, J., Friesen, T., Fujiwara, M.C., Gill, D.R., Gutierrez, A., Hangst, J.S., Hardy, W.N., Hayden, M.E., Humphries, A.J., Hydomako, R., Jenkins, M.J., Jonsell, S., Jørgensen, L.V., Kurchaninov, L., Madsen, N., Menary, S., Nolan, P., Olchanski, K., Olin, A., Povilus, A., Pusa, P., Robicheaux, F., Sarid, E., Seif el Nasr, S., Silveira, D.M., So, C., Storey, J.W., Thompson, R.I., van der Werf, D.P., Wurtele, J.S. and Yamazaki, Y. (2010). Trapped antihydrogen. *Nature*, 468(7324):673–676. doi:10.1038/nature09610

Andresen, G.B., Ashkezari, M.D., Baquero-Ruiz, M., Bertsche, W., Bowe, P.D., Butler, E., Cesar, C.L., Charlton, M., Deller, A., Eriksson, S., Fajans, J., Friesen, T., Fujiwara, M.C., Gill, D.R., Gutierrez, A., Hangst, J.S., Hardy, W.N., Hayano, R.S., Hayden, M.E., Humphries, A.J., Hydomako, R., Jonsell, S., Kemp, S.L., Kurchaninov, L., Madsen, N., Menary, S., Nolan, P., Olchanski, K., Olin, A., Pusa, P., Rasmussen, C.O., Robicheaux, F., Sarid, E., Silveira, D.M., So, C., Storey, J.W., Thompson, R.I., van der Werf, D.P., Wurtele, J.S. and Yamazaki, Y. (2011). Confinement of antihydrogen for 1,000 seconds. *Nature Physics*, 7(7):558–564. doi:10.1038/nphys2025

Baker, C. (2010). *Studies of magnetized positronium and of positron dynamics in a rotating dipolar electric field.* Ph.D. thesis, Swansea University

Baker, C., Jennings, J., Verma, A., Xu, J., Weber, M. and Lynn, K. (2012). Progress toward the long time confinement of large positron numbers. *The European Physical Journal D*, 66:1–7. ISSN 1434-6060. doi:10.1140/epjd/e2012-20631-6

Baur, G., Boero, G., Brauksiepe, A., Buzzo, A., Eyrich, W., Geyer, R., Grzonka, D., Hauffe, J., Kilian, K., LoVetere, M., Macri, M., Moosburger, M., Nellen, R., Oelert, W., Passaggio, S., Pozzo, A., Röhrich, K., Sachs, K., Schepers, G., Sefzick, T., Simon, R.S., Stratmann, R., Stinzing, F. and Wolke, M. (1996). Production of antihydrogen. *Physics Letters B*, 368(3):251 – 258. ISSN 0370-2693. doi:10.1016/0370-2693(96)00005-6

Bertsche, W. and Fajans, J. (2003). Collisional cooling of pure electron plasmas using CO_2. *Non-Neutral Plasma Physics V*, 692:235–238. doi:10.1063/1.1635180. AIP Conference Proceedings

Blanford, G., Christian, D.C., Gollwitzer, K., Mandelkern, M., Munger, C.T., Schultz, J. and Zioulas, G. (1998). Observation of atomic antihydrogen. *Physical Review Letters*, 80:3037–3040. doi:10.1103/PhysRevLett.80.3037

Brillouin, L. (1945). A theorem of larmor and its importance for electrons in magnetic fields. *Physical Review*, 67:260–266. doi:10.1103/PhysRev.67.260

Brown, L.S. and Gabrielse, G. (1986). Geonium theory: Physics of a single electron or ion in a Penning trap. *Review of Modern Physics*, 58:233–311. doi:10.1103/RevModPhys.58.233

Canter, K.F., Mills, Jr., A.P. and Berko, S. (1974). Efficient positronium formation by slow positrons incident on solid targets. *Physical Review Letters*, 33:7–10. doi:10.1103/PhysRevLett.33.7

Canter, K.F., Mills, Jr., A.P. and Berko, S. (1975). Observations of positronium Lyman-α radiation. *Physical Review Letters*, 34:177–180. doi:10.1103/PhysRevLett.34.177

Cassidy, D.B., Deng, S.H.M., Greaves, R.G. and Mills, Jr., A.P. (2006a). Accumulator for the production of intense positron pulses. *Review of Scientific Instruments*, 77(7):073106. doi:10.1063/1.2221509

Cassidy, D.B., Deng, S.H.M., Tanaka, H.K.M. and Mills, Jr., A.P. (2006b). Single shot positron annihilation lifetime spectroscopy. *Applied Physics Letters*, 88(19):194105. doi:10.1063/1.2203336

Cassidy, D.B. and Mills, Jr., A.P. (2007). The production of molecular positronium. *Nature*, 449:195–197. doi:10.1038/nature06094

Cassidy, D.B., Hisakado, T.H., Meligne, V.E., Tom, H.W.K. and Mills, Jr., A.P. (2010a). Delayed emission of cold positronium from mesoporous materials. *Physical Review A*, 82:052511. doi:10.1103/PhysRevA.82.052511

Cassidy, D.B., Crivelli, P., Hisakado, T.H., Liszkay, L., Meligne, V.E., Perez, P., Tom, H.W.K. and Mills, Jr., A.P. (2010b). Positronium cooling in porous silica measured via doppler spectroscopy. *Physical Review A*, 81:012715. doi:10.1103/PhysRevA.81.012715

Cassidy, D.B., Hisakado, T.H., Tom, H.W.K. and Mills, Jr., A.P. (2012). Efficient production of Rydberg positronium. *Physical Review Letters*, 108:043401. doi:10.1103/PhysRevLett.108.043401

Chamberlain, O., Segrè, E., Wiegand, C. and Ypsilantis, T. (1955). Observation of antiprotons. *Physical Review*, 100:947–950. doi:10.1103/PhysRev.100.947

Charlton, M. (1990). Antihydrogen production in collisions of antiprotons with excited states of positronium. *Physics Letters A*, 143(3):143 – 146. doi:10.1016/0375-9601(90)90665-B

Charlton, M. and Humberston, J.W. (2001). *Positron Physics*. Cambridge Monographs on Atomic, Molecular and Chemical Physics - Volume II. Cambridge University Press, Cambridge, first edition. ISBN 0-521-41550-0

Cheng, X., Babikov, D. and Schrader, D.M. (2011). Binding-energy predictions of positrons and atoms. *Physical Review A*, 83:032504. doi:10.1103/PhysRevA.83.032504

Cherry, W.H. (1958). *Secondary Electron Emission Produced from Surfaces by Positron Bombardment*. Ph.D. thesis, Princeton University. Dissertation Abstracts International, Volume: 19-08, page: 2113

Chu, S., Mills, Jr., A.P. and Hall, J.L. (1984). Measurement of the Positronium $1^3S_1 - 2^3S_1$ interval by Doppler-free two-photon spectroscopy. *Physical Review Letters*, 52:1689–1692. doi:10.1103/PhysRevLett.52.1689

Clarke, J., van der Werf, D.P., Griffiths, B., Beddows, D.C.S., Charlton, M. and Telle, H.H. (2003). Developments in the trapping and accumulation of slow positrons using the buffer gas technique. In M. Schauer, T. Mitchell and R. Nebel, editors, *Non-Neutral Plasma Physics V*, volume AIP CP692, pp. 178–183. ISBN 0-7354-0165-9. ISSN 0094-243X. Workshop on Non-Neutral Plasmas, Santa Fe, New Mexico

Clarke, J., van der Werf, D.P., Griffiths, B., Beddows, D.C.S., Charlton, M., Telle, H.H. and Watkeys, P.R. (2006). Design and operation of a two-stage positron accumulator. *Review of Scientific Instruments*, 77(6):063302. doi:10.1063/1.2206561

Cluggish, B.P. and Driscoll, C.F. (1995). Transport and damping from rotational pumping in magnetized electron plasmas. *Physical Review Letters*, 74:4213–4216. doi:10.1103/PhysRevLett.74.4213

Coleman, P. (2000). *Positron beams and their applications*. World Scientific Publishing Co. Pte. Ltd, first edition. ISBN 981-02-3394-9

Cork, B., Lambertson, G.R., Piccioni, O. and Wenzel, W.A. (1956). Antineutrons produced from antiprotons in charge-exchange collisions. *Physical Review*, 104:1193–1197. doi:10.1103/PhysRev.104.1193

Crivelli, P., Gendotti, U., Rubbia, A., Liszkay, L., Perez, P. and Corbel, C. (2010). Measurement of the orthopositronium confinement energy in mesoporous thin films. *Physical Review A*, 81:052703. doi:10.1103/PhysRevA.81.052703

Dale, J.M., Hulett, L.D. and Pendyala, S. (1980). Low energy positrons from metal surfaces. *Surface and Interface Analysis*, 2(6):199–203. doi:10.1002/sia.740020602

Danielson, J.R. and Surko, C.M. (2005). Torque-balanced high-density steady states of single-component plasmas. *Physical Review Letters*, 94:035001. doi:10.1103/PhysRevLett.94.035001

Debenedetti, S. and Corben, H.C. (1954). Positronium. *Annual Review of Nuclear Science*, 4(1):191–218. doi:10.1146/annurev.ns.04.120154.001203

Dehmelt, H.G. (1968). Radiofrequency spectroscopy of stored ions I: Storage. volume 3 of *Advances in Atomic and Molecular Physics*, pp. 53 – 72. Academic Press. doi:10.1016/S0065-2199(08)60170-0

Derenzo, S., Boswell, M., Weber, M. and Brennan, K. (2013). Scintillation properties. Online. `http://scintillator.lbl.gov/`

Dermer, C.D. and Weisheit, J.C. (1989). Perturbative analysis of simultaneous Stark and Zeeman effects on $n = 1 \leftrightarrows n = 2$ radiative transitions in positronium. *Physical Review A*, 40:5526–5532. doi:10.1103/PhysRevA.40.5526

Deutsch, M. (1951). Evidence for the formation of positronium in gases. *Physical Review*, 82(3):455. doi:10.1103/PhysRev.82.455

Dirac, P.A.M. (1928a). The quantum theory of the electron. *Proceedings of the Royal Society London A*, 117:610–624. doi:10.1098/rspa.1928.0023

Dirac, P.A.M. (1928b). The quantum theory of the electron. Part II. *Proceedings of the Royal Society London A*, 118:351–361. doi:10.1098/rspa.1928.0056

Dirac, P.A.M. (1930). A theory of electrons and protons. *Proceedings of the Royal Society London A*, 126(801):360–365. doi:10.1098/rspa.1930.0013

Dirac, P.A.M. (1931). Quantised singularities in the electromagnetic field. *Proceedings of the Royal Society London A*, 133(821):60–72. doi:10.1098/rspa.1931.0130

Dorfan, D.E., Eades, J., Lederman, L.M., Lee, W. and Ting, C.C. (1965). Observation of antideuterons. *Physical Review Letters*, 14:1003–1006. doi:10.1103/PhysRevLett.14.1003

Driscoll, C.F. and Malmberg, J.H. (1983). Length-dependent containment of a pure electron-plasma column. *Physical Review Letters*, 50:167–170. doi:10.1103/PhysRevLett.50.167

Dull, T.L., Frieze, W.E., Gidley, D.W., Sun, J.N. and Yee, A.F. (2001). Determination of pore size in mesoporous thin films from the annihilation lifetime of positronium. *The Journal of Physical Chemistry B*, 105(20):4657–4662. doi:10.1021/jp004182v

Edwardson, C.J., Grogan, M.D.W., Birks, T.A. and Coleman, P.G. (2011). Positron and positronium studies of silica aerogel. *Journal of Physics: Conference Series*, 262:012018. doi:10.1088/1742-6596/262/1/012018

Eggleston, D.L., Driscoll, C.F., Beck, B.R., Hyatt, A.W. and Malmberg, J.H. (1992). Parallel energy analyzer for pure electron plasma devices. *Physics of Fluids B: Plasma Physics*, 4(10):3432–3439. doi:10.1063/1.860399

Eldrup, M., Lightbody, D. and Sherwood, J. (1981). The temperature dependence of positron lifetimes in solid pivalic acid. *Chemical Physics*, 63(1–2):51 – 58. doi:10.1016/0301-0104(81)80307-2

Estrada, J. (2002). *Cold Trapped Positrons and Progress to Cold Antihydrogen.* Ph.D. thesis, Massachusetts Institute of Technology

Fajans, J., Gilson, E. and Friedland, L. (1999). Autoresonant (nonstationary) excitation of the diocotron mode in non-neutral plasmas. *Physical Review Letters*, 82:4444–4447. doi:10.1103/PhysRevLett.82.4444

Franken, P.A., Hill, A.E., Peters, C.W. and Weinreich, G. (1961). Generation of optical harmonics. *Physical Review Letters*, 7:118–119. doi:10.1103/PhysRevLett.7.118

Gabrielse, G., Bowden, N.S., Oxley, P., Speck, A., Storry, C.H., Tan, J.N., Wessels, M., Grzonka, D., Oelert, W., Schepers, G., Sefzick, T., Walz, J., Pittner, H., Hänsch, T.W. and Hessels, E.A. (2002). Background-free observation of cold antihydrogen with field-ionization analysis of its states. *Physical Review Letters*, 89:213401. doi:10.1103/PhysRevLett.89.213401

Gerchikov, L.G. and Gribakin, G.F. (2008). Electron attachment to SF_6 and lifetimes of SF_6^- negative ions. *Physical Review A*, 77:042724. doi:10.1103/PhysRevA.77.042724

Geusic, J.E., Marcos, H.M. and van Uitert, L.G. (1964). Laser oscillations in Nd-doped yttrium aluminum, yttrium gallium and gadolinium garnets. *Applied Physics Letters*, 4(10):182–184. doi:10.1063/1.1753928

Gidley, D.W., Frieze, W.E., Dull, T.L., Yee, A.F., Ryan, E.T. and Ho, H.M. (1999). Positronium annihilation in mesoporous thin films. *Physical Review B*, 60:R5157–R5160. doi:10.1103/PhysRevB.60.R5157

Giordmaine, J.A. and Miller, R.C. (1965). Tunable coherent parametric oscillation in $LiNbO_3$ at optical frequencies. *Physical Review Letters*, 14:973–976. doi:10.1103/PhysRevLett.14.973

Greaves, R.G. and Surko, C.M. (2001). Radial compression and inward transport of positron plasmas using a rotating electric field. *Physics of Plasmas*, 8(5):1879–1885. doi:10.1063/1.1350570

Greaves, R.G. and Moxom, J.M. (2008). Compression of trapped positrons in a single particle regime by a rotating electric field. *Physics of Plasmas*, 15(7):072304. doi:10.1063/1.2956335

Gribakin, G.F., Young, J.A. and Surko, C.M. (2010). Positron-molecule interactions: Resonant attachment, annihilation, and bound states. *Review of Modern Physics*, 82:2557–2607. doi:10.1103/RevModPhys.82.2557

Griffiths, B.C. (2005). *Development of a High powered tunable laser system for spectroscopic studies of trace elements and positronium.* Ph.D. thesis, Swansea University

Gullikson, E.M. and Mills, Jr., A.P. (1986). Positron dynamics in rare-gas solids. *Physical Review Letters*, 57:376–379. doi:10.1103/PhysRevLett.57.376

Hanneke, D., Fogwell, S. and Gabrielse, G. (2008). New measurement of the electron magnetic moment and the fine structure constant. *Physical Review Letters*, 100:120801. doi:10.1103/PhysRevLett.100.120801

Hanson, N.R. (1961). Discovering the positron (I). *British Journal for the Philosophy of Science*, XII(47):194–214. doi:10.1093/bjps/XII.47.194

Heisenberg, W. (1973). Development of concepts in the history of quantum theory. In J. Mehra, editor, *The Physicist's Concept of Nature*, p. 271. D. Reidel Publishing Company. ISBN 978-90-277-0345-3

Howell, R.H., Rosenberg, I.J. and Fluss, M.J. (1987). Production and use of low-energy, monoenergetic positron beams from electron LINACS. *Applied Physics A*, 43:247–255. ISSN 0947-8396. doi:10.1007/BF00635179

Huang, X.P., Anderegg, F., Hollmann, E.M., Driscoll, C.F. and O'Neil, T.M. (1997). Steady-state confinement of non-neutral plasmas by rotating electric fields. *Phys. Rev. Lett.*, 78:875–878. doi:10.1103/PhysRevLett.78.875

Hugenschmidt, C. (2009). Positron sources and positron beams. In A. Dupasquier and A.P. Mills Jr., editors, *Proceedings of the International School of Physics "Enrico Fermi": Physics with Many Positrons*, volume 174, pp. 399–417. IOS Press. ISBN 978-1-60750-647-8. doi:10.3254/978-1-60750-647-8-399

Hughes, V.W., McColm, D.W., Ziock, K. and Prepost, R. (1960). Formation of muonium and observation of its Larmor precession. *Physical Review Letters*, 5:63–65. doi:10.1103/PhysRevLett.5.63

Isaac, C.A. (2010). *Axialisation of Particles in a Penning-type Trap by the Application of a Rotating Dipole Electric Field and its Application to Positron Accumulation.* Ph.D. thesis, Swansea University

Isaac, C.A., Baker, C.J., Mortensen, T., van der Werf, D.P. and Charlton, M. (2011). Compression of positron clouds in the independent particle regime. *Physical Review Letters*, 107:033201. doi:10.1103/PhysRevLett.107.033201

Isaac, C.A. (2013). Motional sideband excitation using rotating electric fields. *Physical Review A*, 87:043415. doi:10.1103/PhysRevA.87.043415

Iwata, K., Greaves, R.G., Murphy, T.J., Tinkle, M.D. and Surko, C.M. (1995). Measurements of positron-annihilation rates on molecules. *Physical Review A*, 51:473–487. doi:10.1103/PhysRevA.51.473

Kerrigan, S.J. (2011). *An Experimental Study of Positron Moderation and Accumulation and the Laser Ionisation of Positronium.* Ph.D. thesis, Swansea University

Khatri, R., Charlton, M., Sferlazzo, P., Lynn, K.G., Mills, Jr., A.P. and Roellig, L.O. (1990). Improvement of rare-gas solid moderators by using conical geometry. *Applied Physics Letters*, 57(22):2374–2376. doi:10.1063/1.103856

Knoll, G.F. (2000). *Radiation Detection and Measurement.* John Wiley & Sons Inc., New York, third edition. ISBN 9780471073383

Kobayashi, Y., Zheng, W., Meyer, E., McGervey, J., Jamieson, A. and Simha, R. (1989). Free volume and physical aging of poly(vinyl acetate) studied by positron annihilation. *Macromolecules*, 22(5):2302–2306. doi:10.1021/ma00195a052

Kobayashi, Y., Ito, K., Oka, T. and Hirata, K. (2007). Positronium chemistry in porous materials. *Radiation Physics and Chemistry*, 76(2):224–230. ISSN 0969-806X. doi:10.1016/j.radphyschem.2006.03.042. Proceedings of the 8th International Workshop on Positron and Positronium Chemistry

Kramida, A., Ralchenko, Y., Reader, J. and NIST ASD Team (2013). NIST atomic spectra database (v. 5.0). Online. `http://physics.nist.gov/asd`

Leventhal, M., MacCallum, C.J. and Stang, P.D. (1978). Detection of 511 keV positron annihilation radiation from the galactic center direction. *Astrophysical Journal, Part 2 - Letters to the Editor*, 225. doi:10.1086/182782

Ley, R. (2002). Atomic physics of positronium with intense slow positron beams. *Applied Surface Science*, 194(1-4):301–306. ISSN 0169-4332. doi:10.1016/S0169-4332(02)00139-3. 9th International Workshop on Slow Positron Beam Techniques for Solids and Surfaces

Liang, E.P. and Dermer, C.D. (1988). Laser cooling of positronium. *Optics Communications*, 65(6):419 – 424. ISSN 0030-4018. doi:10.1016/0030-4018(88)90116-2

Liszkay, L., Barthe, M.F., Corbel, C., Crivelli, P., Desgardin, P., Etienne, M., Ohdaira, T., Perez, P., Suzuki, R., Valtchev, V. and Walcarius, A. (2008a). Orthopositronium annihilation and emission in mesostructured thin silica and silicalite-1 films. *Applied Surface Science*, 255(1):187 – 190. ISSN 0169-4332. doi:10.1016/j.apsusc.2008.05.210. Proceedings of the Eleventh International Workshop on Slow Positron Beam Techniques for Solids and Surfaces

Liszkay, L., Corbel, C., Perez, P., Desgardin, P., Barthe, M.F., Ohdaira, T., Suzuki, R., Crivelli, P., Gendotti, U., Rubbia, A., Etienne, M. and Walcarius, A. (2008b). Positronium reemission yield from mesostructured silica films. *Applied Physics Letters*, 92(6):063114. doi:10.1063/1.2844888

Major, F., Gheorghe, V.N. and Werth, G. (2005). *Charged particle traps: physics and techniques of charged particle field confinement.* Springer, first edition. ISBN 9783540220435

Malmberg, J.H. and Driscoll, C.F. (1980). Long-time containment of a pure electron plasma. *Physical Review Letters*, 44:654–657. doi:10.1103/PhysRevLett.44.654

Marjanović, S., Banković, A., Šuvakov, M. and Petrović, Z.L. (2013). Rotating wall technique for positron cloud compression: a Monte-Carlo simulation. A poster (P-11) presented at the XVII International Workshop on Low-Energy Positron and Positronium physics (POSMOL 2013, *Kanazawa*)

Marler, J.P. and Surko, C.M. (2005). Positron-impact ionization, positronium formation, and electronic excitation cross sections for diatomic molecules. *Physical Review A*, 72:062713. doi:10.1103/PhysRevA.72.062713

Massam, T., Muller, T., Righini, B., Schneegans, M. and Zichichi, A. (1965). Experimental observation of antideuteron production. *Nuovo Cimento Serie*, 39:10–14. doi:10.1007/BF02814251

Massey, H.S.W. and Mohr, C.B.O. (1954). Gaseous reactions involving positronium. *Proceedings of the Physical Society. Section A*, 67(8):695. doi:10.1088/0370-1298/67/8/306

Merrison, J.P., Charlton, M., Deutch, B.I. and Jørgensen, L.V. (1992). Field assisted positron moderation by surface charging of rare gas solids. *Journal of Physics: Condensed Matter*, 4(12):L207. doi:10.1088/0953-8984/4/12/003

Mills, Jr., A.P. (1981). Observation of the positronium negative ion. *Physical Review Letters*, 46:717–720. doi:10.1103/PhysRevLett.46.717

Mills, Jr., A.P. and Leventhal, M. (2002). Can we measure the gravitational free fall of cold Rydberg state positronium? *Nuclear Instruments and Methods in Physics Research Section B: Beam Interactions with Materials and Atoms*, 192(1–2):102 – 106. doi:10.1016/S0168-583X(02)00789-9

Mills, Jr., A.P. (2002). Positronium molecule formation, Bose-Einstein condensation and stimulated annihilation. *Nuclear Instruments and Methods in Physics Research Section B: Beam Interactions with Materials and Atoms*, 192(1–2):107–116. ISSN 0168-583X. doi:10.1016/S0168-583X(02)00790-5

Mohorovičić, S. (1934). Möglichkeit neuer elemente und ihre bedeutung für die astrophysik. *Astronomische Nachrichten*, 253(4):93

Mortensen, T., Deller, A., Isaac, C.A., van der Werf, D.P., Charlton, M. and Machacek, J.R. (2013). Manipulation of the magnetron orbit of a positron cloud in a penning trap. *Physics of Plasmas*, 20(1):012124. doi:10.1063/1.4789880

Mortensen, T. (2013). *Manipulation of the magnetron orbits of particles and clouds in a two-stage buffer gas accumulator.* Ph.D. thesis, Swansea University

Nagashima, Y., Morinaka, Y., Kurihara, T., Nagai, Y., Hyodo, T., Shidara, T. and Nakahara, K. (1998). Origins of positronium emitted from SiO_2. *Physical Review B*, 58:12676–12679. doi:10.1103/PhysRevB.58.12676

Notte, J., Fajans, J., Chu, R. and Wurtele, J.S. (1993). Experimental breaking of an adiabatic invariant. *Physical Review Letters*, 70:3900–3903. doi:10.1103/PhysRevLett.70.3900

Özen, A., Garner, A. and Laricchia, G. (2000). Rare gas solid moderator for Ps beam at UCL. *Nuclear Instruments and Methods in Physics Research Section B: Beam Interactions with Materials and Atoms*, 171(1-2):172–177. doi:10.1016/S0168-583X(00)00045-8

Paulin, R. and Ambrosino, G. (1968). Annhilation libre de l'ortho-positronium forme dans certaines poudres de grande surface specifique. *Journal of Physics*, 29(4):263–270. doi:10.1051/jphys:01968002904026300

Penning, F.M. (1936). Die glimmentladung bei niedrigem druck zwischen koaxialen zylindern in einem axialen magnetfeld. *Physica*, 3(9):873 – 894. ISSN 0031-8914. doi:10.1016/S0031-8914(36)80313-9

Petkov, M.P., Lynn, K.G. and Roellig, L.O. (1996). Water-induced effects on the positron moderation efficiency of rare gas solids. *Journal of Physics: Condensed Matter*, 8(41):L611. doi:10.1088/0953-8984/8/41/003

Qu, X., Zhang, L., Zhu, R.Y., Liao, J., Shen, D. and Yin, Z. (2002). A study on yttrium doping in lead tungstate crystals. *Nuclear Instruments and Methods in Physics Research Section A: Accelerators, Spectrometers, Detectors and Associated Equipment*, 480:470 – 487. doi:10.1016/S0168-9002(01)01217-7

Quint, W., Kaiser, R., Hall, D. and Gabrielse, G. (1993). (anti)hydrogen recombination studies in a nested Penning trap. *Hyperfine Interactions*, 76(1):181–188. doi:10.1007/BF02316717

Rich, A. (1981). Recent experimental advances in positronium research. *Review of Modern Physics*, 53(1):127. doi:10.1103/RevModPhys.53.127

Ruark, A.E. (1945). Positronium. *Physical Review*, 68(11-12):278. doi:10.1103/PhysRev.68.278

Sarid, E., Gilson, E. and Fajans, J. (2002). Decay of the diocotron rotation and transport in a new low-density asymmetry-dominated regime. *AIP Conference Proceedings*, 606(1):422–432. doi:10.1063/1.1454313

Schultz, P.J. and Lynn, K.G. (1988). Interaction of positron beams with surfaces, thin films, and interfaces. *Review of Modern Physics*, 60:701–779. doi:10.1103/RevModPhys.60.701

Silfast, W.T. (1996). *Laser Fundamentals*. Cambridge University Press, second edition. ISBN 0-521-83345-0

Soga, Y., Kiwamoto, Y. and Hashizume, N. (2006). Transport processes of a non-neutral plasma coupled to an external rotating wave. *Physics of Plasmas*, 13(5):052105. doi:10.1063/1.2193911

Sperber, W., Becker, D., Lynn, K.G., Raith, W., Schwab, A., Sinapius, G., Spicher, G. and Weber, M. (1992). Measurement of positronium formation in positron collisions with hydrogen atoms. *Physical Review Letters*, 68:3690–3693. doi:10.1103/PhysRevLett.68.3690

Storry, C.H., Speck, A., Sage, D.L., Guise, N., Gabrielse, G., Grzonka, D., Oelert, W., Schepers, G., Sefzick, T., Pittner, H., Herrmann, M., Walz, J., Hänsch, T.W., Comeau, D. and Hessels, E.A. (2004). First laser-controlled antihydrogen production. *Physical Review Letters*, 93:263401. doi:10.1103/PhysRevLett.93.263401

Sullivan, J.P., Marler, J.P., Gilbert, S.J., Buckman, S.J. and Surko, C.M. (2001). Excitation of electronic states of Ar, H_2, and N_2 by positron impact. *Physical Review Letters*, 87:073201. doi:10.1103/PhysRevLett.87.073201

Sunn Pedersen, T., Danielson, J.R., Hugenschmidt, C., Marx, G., Sarasola, X., Schauer, F., Schweikhard, L., Surko, C.M. and Winkler, E. (2012). Plans for the creation and studies of electron-positron plasmas in a stellarator. *New Journal of Physics*, 14(3):035010. doi:10.1088/1367-2630/14/3/035010

Surko, C.M., Wysocki, F.J., Leventhal, M. and Passner, A. (1988). Accumulation and storage of low energy positrons. *Hyperfine Interactions*, 44:185–200. ISSN 0304-3843. doi:10.1007/BF02398669

Surko, C.M. and Murphy, T.J. (1992). Positron trapping in an electrostatic well by inelastic collisions with nitrogen molecules. *Physical Review A*, 46:5696–5705. doi:10.1103/PhysRevA.46.5696

Surko, C.M. and Greaves, R.G. (2003). A multicell trap to confine large numbers of positrons. *Radiation Physics and Chemistry*, 68(3–4):419 – 425. ISSN 0969-806X. doi:10.1016/S0969-806X(03)00194-4. Proceedings of the 7th International Conference on Positron and Positronium Chemistry

Surko, C.M. and Greaves, R.G. (2004). Emerging science and technology of antimatter plasmas and trap-based beams. *Physics of Plasmas*, 11(5):2333–2348. doi:10.1063/1.1651487

Tao, S.J. (1972). Positronium annihilation in molecular substances. *The Journal of Chemical Physics*, 56(11):5499–5510. doi:10.1063/1.1677067

Telle, H.H., González Ureña, A. and Donovan, R.J. (2007). *Laser Chemistry*. John Wiley & Sons Ltd., first edition. ISBN 978-0-471-48571-1

Watkeys, P.R. (2008). *Advances in positron accumulation techniques*. Ph.D. thesis, Swansea University

Wineland, D., Ekstrom, P. and Dehmelt, H. (1973). Monoelectron oscillator. *Physical Review Letters*, 31:1279–1282. doi:10.1103/PhysRevLett.31.1279

Wiza, J.L. (1979). Microchannel plate detectors. *Nuclear Instruments and Methods*, 162(1–3):587 – 601. ISSN 0029-554X. doi:10.1016/0029-554X(79)90734-1

Yamazaki, T., Morita, N., Hayano, R.S., Widmann, E. and Eades, J. (2002). Antiprotonic helium. *Physics Reports*, 366:183 – 329. ISSN 0370-1573. doi:10.1016/S0370-1573(01)00082-5

Yu, R.S., Ohdaira, T., Suzuki, R., Ito, K., Hirata, K., Sato, K., Kobayashi, Y. and Xu, J. (2003). Positronium time-of-flight measurements of porous low-k films. *Applied Physics Letters*, 83(24):4966–4968. doi:10.1063/1.1634380

Ziock, K.P., Howell, R.H., Magnotta, F., Failor, R.A. and Jones, K.M. (1990a). First observation of resonant excitation of high-n states in positronium. *Physical Review Letters*, 64:2366–2369. doi:10.1103/PhysRevLett.64.2366

Ziock, K.P., Dermer, C.D., Howell, R.H., Magnotta, F. and Jones, K.M. (1990b). Optical saturation of the $1^3S - 2^3P$ transition in positronium. *Journal of Physics B: Atomic, Molecular and Optical Physics*, 23(2):329. doi:10.1088/0953-4075/23/2/015